Azimuthal Correlations of High-p_T Photons and Hadrons in Au+Au Collisions at STAR

Dissertation
zur Erlangung des Doktorgrades
der Naturwissenschaften

vorgelegt beim Fachbereich Physik
der Johann-Wolfgang-Goethe-Universität
in Frankfurt am Main

von
Thomas Dietel
aus Ansbach

Frankfurt am Main, 2005 (D F 1)

Zusammenfassung

Diese Arbeit untersucht azimuthale Korrelationen von Photonen und geladenen Hadronen mit hohem Transversalimpuls in Kollisionen von zwei Goldkernen bei einer Schwerpunktsenergie von $\sqrt{s_{NN}} = 200\,\mathrm{GeV}$. Die Daten wurden mit dem STAR-Experiment am Relativistic Heavy Ion Collider (RHIC) aufgezeichnet.

Kernmaterie, die unter normalen Umständen in Form von Protonen und Neutronen vorkommt, durchläuft bei hohen Temperaturen und Dichten einen Phasenübergang, bei dem die hadronischen Freiheitsgrade des Systems durch partonische ersetzt werden: die Nukleonen „schmelzen" und setzen die in ihnen enthaltenen Quarks und Gluonen frei. Dieses Medium aus freien Partonen wird Quark-Gluonen-Plasma (QGP) genannt, und kommt in der Natur nur unter extremen Bedingungen wie bei der Entstehung des Universums und im Inneren von Neutronensternen vor. Mit den Beschleunigern der neuesten Generation ist es möglich, diese extreme Form von Materie auch im Labor zu erzeugen, indem Atomkerne bei relativistischen Energien zur Kollision gebracht werden. Um die für ein thermodynamisches System notwendige Teilchenzahl zu erhalten, sind Kerne mit hoher Nukleonenzahl wie Blei oder Gold notwendig. Die Kernmaterie wird durch eine Vielzahl von Kollisionen der Partonen der Projektile so stark erhitzt, dass kurzzeitig ein QGP entsteht. Aufgrund des hohen Druckes und der Temperatur des QGP expandiert das Medium, und kühlt so ab. Fällt die Temperatur des QGP unter die kritische Temperatur des Phasenüberganges, so werden die Quarks und Gluonen wieder zu Hadronen kombiniert, die dann zuerst als heißes Hadronengas expandieren und dann als freie, nicht mehr wechselwirkende Teilchen den Kollisionsbereich verlassen. Ein Überblick über Schweionenphysik ist in Kapitel **??** zu finden.

Kapitel 2 vertieft dann einen Teilbereich der Schwerionenphysik, die Produktion harter Proben und insbesondere Korrelationen zwischen Teilchen mit hohem Transversalimpuls. Diese Teilchen können nur in den ersten, sehr harten Kollisionen von Partonen der Projektilkerne entstehen, da in darauffolgenden Wechselwirkungen die Energie nicht mehr ausreicht, um solch hochenergetische Teilchen zu erzeugen. Der Produktionsmechanismus von Teilchen mit hohem Transversalimpuls kann mit der Quantenchromodynamik (QCD) beschrieben werden und stimmt gut mit Messungen in Proton-Proton-Kollisionen üeberein. Die QCD beschreibt diese Kollisionen als Kollision einzelner Partonen, die sich, obwohl sie in den Nukleonen gefangen sind, bei hohen Impulsüberträgen verhalten, als wären sie frei, ein Phänomen, das als asymptotische Freiheit bekannt ist. Diese Parton-Parton-Kollisionen können mit Hilfe von Feynman-Diagrammen im Rahmen quantenchromodynamischer Störungsrechnungen beschrieben werden. Typischerweise werden in diesen Kollisionen Paare von Quarks oder Gluonen mit hohem Transversalimpuls erzeugt, die allerdings nicht direkt beobachtbar sind, sondern in eine Gruppe von Hadronen, einen sogenannten Jet, fragmentieren. Durch die Messung aller Teilchen eines Jets können die kinetischen Eigenschaften des ursprünglischen Partons rekonstruiert werden. In einigen Fällen werden allerdings anstatt zweier Partonen ein Photon und ein Quark und ein Gluon erzeugt. Da dies keine reinen QCD-Prozesse sind, sondern auch eine elektromagnetische Wechselwirkung enthalten, sind sie gegenüber Dijet-Erieignissen allerdings stark unterdrückt.

Da die Produktion von Teilchen mit hohem Transversalimpuls sehr gut verstanden ist, eignen sich diese gut zur Untersuchung der heißen und dichten Materie, die in Schwerionenkollisionen erzeugt wird. Wechselwirkungen zwischen Jets und dem Medium spiegeln die Eigenschaften des heißen Mediums wider und führen zu einer Modifikation der Production von Teilchen mit hohem Transversalimpuls. Die Messungen der ersten Jahre des RHIC Programms zeigen eine Unterdrückung dieser Teilchen in Schwerionenkollisionen. Die Transversalimpulsspektren einzelner Teilchen lassen sich am einfachsten anhand des nuklearen Modifikationsfaktors R_{AA} vergleichen, der definiert ist als das Verhältnis des beobachteteten Teilchenproduktion und der erwarteten Produktion unter der Annahme, dass eine Kollision zweier Kerne als Superposition unabhängiger Nukleon-Nukleon-Kollisionen beschrieben werden kann. In den zentralsten Au+Au-Kollisionen wurde $R_{AA} \approx 0.2$ gemessen, also eine Unterdrückung von Teilchen mit hohem Transversalimpuls $p_T > 5\,\mathrm{GeV}/c$ um einen Faktor 5. Diese starke Reduktion deutet darauf hin, dass Partonen Energie verlieren, wenn sie das heiße Medium durchqueren, und die daraus entstehenden Hadronen deshalb bei geringerer Energie gemessen werden. Alternative Theorien, die die Unterdrückung mit einer Modifikation der PDFs in schweren Kernen erklären, konnten aufgrund einer Vergleichsmessung mit d+Au-Kollisionen ausgeschlossen werden.

Eine weitere Möglichkeit zur Messung des Energieverlustes eines Quarks nutzt die azimuthalen Korrelation zwischen Teilchen des selbem und des entgegengesetzten Jets. Teilchen aus einem Jet sind sehr stark gebündelt, Polar- und Azimuthwinkel des Impulsvektors sind daher stark korreliert, während der Betrag des Impulses gemäß der Fragmentationsfunktion verteilt ist, und deshalb keine Korrelation zwischen den Teilchen zeigt. Wie bereits erwähnt werden Jets oft paarweise erzeugt, wobei sich die beiden Jets im Schwerpunktssystem der Parton-Parton-Kollision in entgegengesetzte Richtungen bewegen. Aufgrund des geringen Transversalimpulses der Partonen im Kern bewegt sich auch das Schwerpunktssytem kaum in transversaler Richtung, so dass die transversalen Komponenten der Impulse der beiden Jets ebenfalls in entgegengesetzte Richtungen zeigen. Der azimuthale Winkel zwischen den beiden Jets ist damit zirka 180°. Der azimuthale Winkel zwischen Teilchen aus entgegengesetzten Jets wird deshalb ebenfalls etwa 180° betragen. Wenn man die Korrelation im Ganzen betrachtet, wird man eine schmalen Anhäufung von Paaren mit einer Differenz der Azimuthalwinkel $\Delta\phi$ bei $\Delta\phi \approx 0$ aufgrund von Teilchen aus dem selben Jet und eine etwas breitere Anhäufung bei $\Delta\phi \approx \pi$ aufgrund von Teilchen aus entgegengesetzten Jets erwarten. Zufällige Kombinationen sind über den gesamten Bereich von 0 bis 2π verteilt und bilden einen nahezu flachen Untergrund unter den jetartigen Korrelationen. Im Jahr 2001 konnte STAR zeigen, dass die Korrelationen von geladenen Triggerteilchen in einem Transversalimpulsbereich von $4\,\mathrm{GeV} < p_T^{trigger} < 6\,\mathrm{GeV}$ und geladenen assozierten Teilchen $2\,\mathrm{GeV} < p_T^{assoc} < 4\,\mathrm{GeV}$ mit in p+p-Kollisionen wie erwartet sowohl einen diesseitigen als auch einen entgegengesetzten Jet widerspiegeln. Die Analyse von zentralen Au+Au-Kollisionen hat nach Abzug des kombinatorischen Untergrundes dagegen nur die für einen diesseitigen Jet charakterische Anhäufung bei $\Delta\phi \approx 0$ gezeigt, während keine Hinweise auf die Existenz von entgegengesetzten Dijets gefunden wurden. Dies kann damit erklärt werden, dass nur Jets, die nahe der Oberfläche des heißen Mediums entstehen, das Medium verlassen können, währen Jets die einen langen Weg zurücklegen müssen zu viel Energie verlieren, um noch beobachtet werden zu können. Da im Fall von entgegengesetzten Dijets ein Jet immer einen relativ lange Wegstrecke zuruückzulegen hat, verschwinden die charakteristischen Korrelationen entgegengesetzter Jets bei $\Delta\phi \approx \pi$ nahezu vollständig. Auch hier konnte eine Vergleichsmessung in d+Au-Kollisionen die beobachtete Unterdückung von Teilchen aus entgegengesetzten Jets nicht rekonstuieren, so dass Effekte aufgrund kalter Kernmatierie als Erklärung ausgeschlossen werden können. Die in dieser Dissertation präsentierte Analyse dehnt die Untersuchung von Korrelationen bei hohem Transversalimpuls auf ungeladene, mit dem elektromagnetischen Kalorimeter gemessene Triggerteilchen aus, und ist so nicht nur Hadronen, hier neutrale Pionen, sondern auch auf einzelne Photonen aus

In Kapitel **??** wird als Grundlage für die Datenanalyse das experimentelle Umfeld dieser Dissertation beschrieben. Die Arbeit wurde am derzeit größten Beschleuniger für schwere Kerne durchgeführt, dem Relativistic Heavy Ion Collider (RHIC) am Brookhaven National Laboratory in den USA. RHIC kann verschiedene Ionensorten von Protonen bis zu Goldkernen auf Energien bis zu $\sqrt{s_{NN}} = 200\,\mathrm{GeV}$ beschleunigen. Seit seiner Inbetriebnahme im Jahr 2000 wurden p+p, Au+Au, Cu+Cu und d+Au Kollisionen bei Energien zwischen 20 und 200 GeV erzeugt. Diese Kollisionen wurden von fünf Experimenten aufgezeichnet: hinter den beiden größeren, STAR und PHENIX, stehen jeweils Kollaborationen von mehr als 500 Physikern, die weite Bereiche der Schwerionenphysik abdecken; die übrigen drei, PHOBOS, BRAHMS und pp2pp, sind mit jeweils weniger als 100 Wissenschaftlern deutlich kleiner und auf wenige Themengebiete spezialisiert. Diese Analyse bezieht sich auf Daten, die während einer langen Strahlzeit mit Au+Au-Kollisionen bei der maximalen Energie von $\sqrt{s_{NN}} = 200\,\mathrm{GeV}$ im Jahr 2004 genommen wurden.

Das STAR-Experiment, mit dem die Daten für diese Analyse aufgezeichnet wurden, wird ebenfalls in Kapitel **??** beschrieben. Das Herz von STAR bildet eine große, zylindrische Spurendriftkammer (TPC[1]), die geladene Teilchen mit Rapiditäten bis zu $\eta < 1.8$ und voller azimuthaler Akzeptanz messen kann. Außer der TPC wurde für diese Analyse noch das Elektromagnetische Kalorimeter (EMC) verwendet, das den Mantel und eine Stirnfläche der TPC umschließt und bei vollem Ausbau eine Akzeptanz von $|\eta| < 1$ für den Mantel (engl. Barrel Electro-Magnetic Calorimeter, BEMC) beziehungsweise $1 < \eta < 2$ für die Stirnfläche (engl. Endcap Electro-Magnetic Calorimeter, EEMC), sowie 2π im Azimuth. Während der Strahlzeit 2004 war nur eine Hälfte des für diese Analyse verwendeten BEMC verfügbar, so dass die Akzeptanz auf $0 < \eta < 1$ beschränkt war.

Zur Aufzeichnung der Daten wurde ein Trigger eingesetzt, um Kollisionen mit Teilchen

[1]engl. Time Projection Chamber

auszuwählen, die eine große Energiemenge im BEMC deponieren. Der Triggeralgorithmus wurde auf zwei Ebenen des STAR Triggersystems implementiert: auf der untersten Ebene (Level-0) wurde ein relativ niedriger Schwellwert gefordert, so dass die Ereignisse auch von anderen Analysen verwendet werden konnen. Auf der höchsten Ebene (Level-3) wurde dann eine wesentlich höhere Schwelle verlangt, so dass nur sehr wenige Ereignisse selektiert wurden. Diese Ereignisse wurden dann in einen sogenannten Express Stream geschrieben, der mit höherer Priorität rekonstruiert und analysiert wurde. Für Level-0 konnte auf einen bereits implementierten Algorithmus zurückgegriffen werden, Level-3 musste dagegen erweitert werden, um die Selektion durchführen zu können. Kapitel **??** beschreibt Funktionalität und Aufbau des Level-3 Trigger-Systems sowie die Integration des BEMC, die im Rahmen dieser Arbeit durchgeführt wurde.

Das Kernstück dieser Arbeit bildet Kapitel **??**, das die Analyse von Korrelationen von Photonen und geladenen Hadronen

Contents

List of Figures

Chapter 1

Introduction

During the last century, our understanding of the structure of matter came a long way. Atoms, thought to be indivisible at the end of the 19th century have shown a complex substructure, containing a shell of electrons and a nucleus of protons and neutrons. These particles were soon considered the building blocks of matter: the fundamental role of atoms had been taken over by nucleons and electrons. A series of discoveries starting with the muon in 1937, followed by the pion and the kaon in 1947 laid the foundation for the so-called particle zoo, a list of more than 150 particle known today. The search for a system in the zoo lead to a classification in three categories: *leptons* that only interact electro-magnetically and weakly, *hadrons* that are also subject to the strong interaction, and the mediators of the fundamental forces called *gauge bosons*. The group of leptons only consists of the electron, the muon and the tau, the respective neutrinos and their anti-particles for a total of twelve particles, a tiny number compared to the plethora of known hadrons. The large number of hadrons, and the reactions between them, can be explained with the existence of even smaller particles, the quarks. Based on the substructure of *quarks*, hadrons can be divided into two sub-categories: hadrons containing a quark and an anti-quark are called *mesons*, and hadrons consisting of three quarks are called *baryons*.

The quest for a comprehensive description of these particles and their interactions lead to development of the Standard Model of particle physics (SM). With the electromagnetic, the weak and the strong interaction, it describes three of the four fundamental forces known today. Perhaps the greatest success of the SM is the unification of the weak and the electromagnetic force: the two forces are described as two aspects of an electroweak interaction, with the difference that the electromagnetic interaction is mediated by the photon, and the weak interaction by the Z^0 and $W^\pm$ bosons. Differences between the electromagnetic and the weak interaction are mainly due to the mass of the gauge bosons mediating the force: the massless photon allows for the long range of the electromagnetic interaction, while the large mass of the $W^\pm$ and Z^0 — $80\,\mathrm{GeV}/c^2$ and $91\,\mathrm{GeV}/c^2$, respectively — limits the range and the strength of the weak interaction. Due to the small coupling constant $\alpha \approx 1/137$, even leading- and next-to-leading-order calculations provide predictions that have been tested to extremely high precision with the LEP collider at CERN, Geneva.

This precision is in contrast to the often surprising properties of the strong interaction. Although the unification of the electroweak theory with the theory of the strong interaction is the ultimate goal of particle physicists, so far no such grand unified theory has been found. Instead, the theory of the strong interaction is described by a separate quantum theory. Especially the combination of two seemingly contradictory phenomena made the development of such a theory a difficult task: the confinement of quarks in hadrons and the asymptotic freedom at large momentum transfers.

1.1 Quantum Chromodynamics

Although quarks are fundamental, elementary particles, they have never been observed isolated from other quarks, but only bound in hadrons. Any attempt to forcibly remove a quark from its hadron will result in the production of new hadrons, but will not free the quark: the quark is said to be confined in the hadron. This confinement can be understood assuming a very strong interaction between the quarks.

On the other hand, interactions of hadrons at high energies can successfully be described by a parton model that assumes constituent quarks that move freely within a hadron. In this case of high momentum transfer, the interaction between the quarks in a hadron have to be rather weak, and the quarks are said to be asymptotically free.

The quantum field theory that can explain both effects is Quantum Chromodynamics (QCD): It describes the strong force as an interaction of particles carrying a color charge, the quarks, with gauge bosons called gluons. A central part of QCD is the energy dependence of the interaction strength: for small momentum transfers or large distances between two quarks, α_s becomes very large, which explains the strength of the force necessary for confinement. At small distances, α_s is small and the force is weaker. Therefore, quarks bound in hadrons appear free when probed at high energies that relate to small distances, and confined when probed at low momentum transfers.

The explanation of this mechanism has been a major break-through in the understanding of the strong interaction, and was awarded with the Nobel prize in 2004 [2, 3]. To explain the different strength of the strong interaction for different energy regimes, an energy-dependent coupling constant has to be assumed. A similar energy dependence is known from quantum-electrodynamics, where it is usually explained as the screening of a charge by virtual photons and electron-positron pairs that constantly surround the charge. The charge polarizes the surrounding cloud of virtual particles, and the interaction

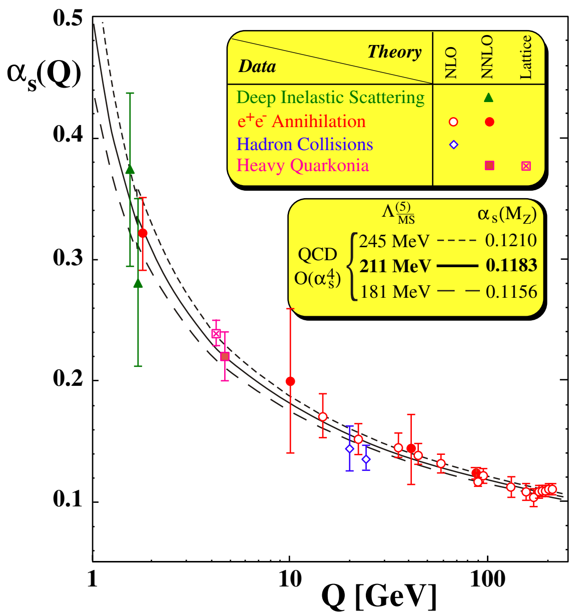

Figure 1.1: Energy dependence of the strong coupling constant $\alpha_s(Q^2)$. A compilation of measurements of α_s is compared to the energy dependence predicted by QCD for three different values of the coupling constant at the mass of the Z^0 boson $\alpha_s(M_Z)$. [1]

strength will depend on how far a probe can penetrate the cloud. In QED, this effect is very small, and leads to a slow increase of the coupling constant for decreasing distance to the probe. In QCD, a strong dependence of the coupling constant and a decrease with increasing momentum transfer would be required to explain asymptotic freedom and confinement with a single theory.

The solution to this problem was the introduction of gauge bosons that carry a color charge and therefore couple to themselves. In this case, the screening behaves in the desired way, showing a strong interaction between well separated quarks, and a relatively weak interaction at high momentum transfers. As the interaction increases with distance, the effect is often called anti-screening. QCD can predict the energy dependence of this effect, and thus the energy dependence of the coupling constant of the strong interaction α_s, although the absolute scale of α_s is not determined by QCD. The measurement of α_s at one energy, e.g. the mass of the Z^0 vector boson, then determines the full behavior of the coupling constant as a function of momentum transfer $\alpha_s(Q^2)$. Figure 1.1 shows that the QCD prediction agrees very well with the available data.

A consequence of the running coupling constant $\alpha_s(Q^2)$ is that perturbation theory is only applicable in the high-energy regime where α_s is sufficiently small. Perturbative QCD (pQCD) can therefore explain hard processes with large momentum transfer very well. But for soft processes with small momentum transfer, pQCD will fail due to the large α_s, and alternative methods have to be used, e.g. calculations in a discretized lattice representation of the QCD fields. These lattice QCD calculations provide insight into QCD phenomena at very low momentum transfers like the structure of hadrons which is directly connected to their masses.

1.2 Quark-Gluon-Plasma

Under normal conditions, nuclear matter exists in the form of protons and neutrons, each containing three valence quarks, plus a sea of virtual quark-antiquark pairs and gluons. Nucleons have a finite radius of about 0.87 fm and a mass of 938 to 939 MeV, which corresponds to an average density of about 0.35 GeV/fm^3. The nuclear density typically found in nuclei is smaller than the density of a single neutron and amounts to about 0.15 GeV/fm^3, indicating that the nucleons are well separated and do not overlap.

It is however assumed that under some circumstances matter exists at much higher densities, for example in the first moments after the Big Bang, or in the center of neutron stars. This opens the question, which form nuclear matter takes under these extreme conditions.

In the case of neutron stars, nuclear matter is compressed by gravity at low temperatures.

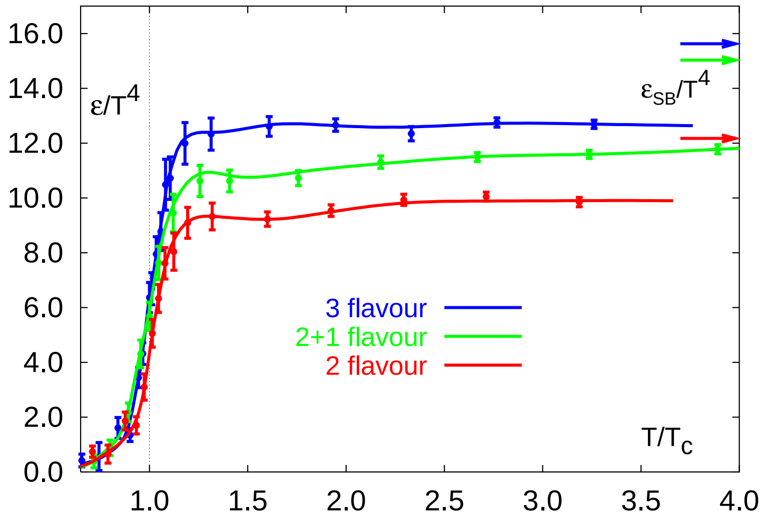

Figure 1.2: Energy density of nuclear matter. The three curves denote the cases for two or three massless quarks, and a case with two massless quarks and a strange quark with a finite, but non-zero mass. All other quark masses are considered infinite.[4]

As the compression increases, at some point the space available for a single nucleon will be smaller than its natural size, and the nucleons will begin to overlap. In this case the partons can no longer be associated with a single nucleon, and the concept of confinement becomes dubious, if not obsolete.

A similar effect can be reached by increasing the temperature of nuclear matter instead of its density: frequent collisions between the nucleons help in breaking them up and freeing the quarks. It is generally believed that the early universe went through a phase like this, where the high temperature prevented the formation of hadrons from the soup of quarks and gluons.

This phase of nuclear matter, where quarks and gluons are no longer bound in hadrons, but can roam freely over a much larger volume like the center of a neutron star or the entire universe at the age of fractions of a milli-second, is called a Quark-Gluon Plasma (QGP).

A primary tool for the theoretical understanding of the QGP are lattice QCD calculations, that relate the fundamental interactions between quarks and gluons with thermodynamical properties of the QGP, like energy density and temperature. These calculations predict a transition from hadronic matter to a phase that is dominated by partonic degrees of freedom. The transition is accompanied by an increase in the number of degrees of freedom in the system that is reflected by the energy density of the system. Figure 1.2 shows the energy density ϵ, divided by the fourth power of the temperature T as a function of temperature T from a lattice QCD calculation [4]. The steep rise around $T \approx T_C$ reflects

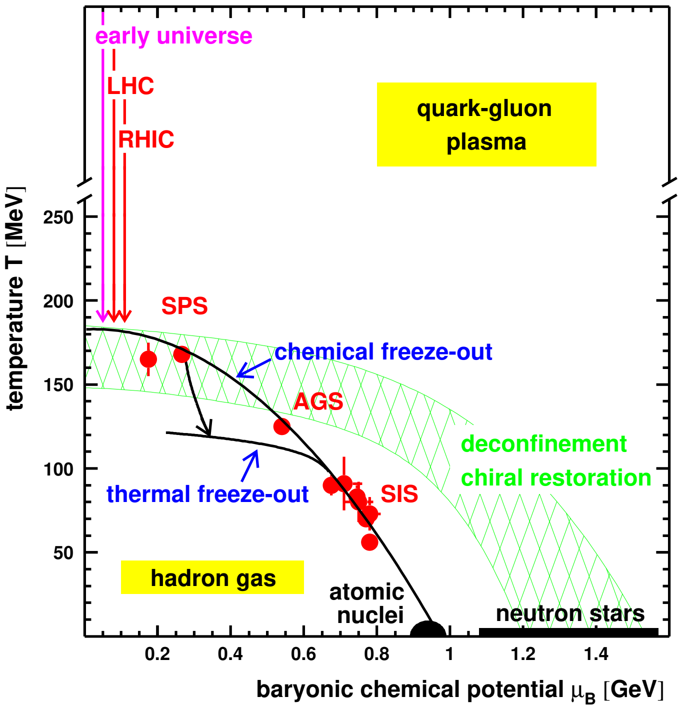

Figure 1.3: Phase diagram of nuclear matter. [5]

the break-up of the nucleons into their constituents and the corresponding increase in degrees of freedom. T_C is called the critical temperature and determines the point where the phase transition from a gas of hadrons to a plasma of quarks and gluons occurs.

As already mentioned, movement of the particles in such a system can influence the properties of the phase transition: the frequent collisions in a hot medium favor the dissociation of the hadrons and reduce the density that is required for this phase transition. Figure 1.3 illustrates this behavior by showing the shape of the phase boundary as a function of temperature T and baryochemical potential μ_B that is closely linked to the density of the system. The two examples given earlier are shown near the axes of the diagram: neutron stars exist at very low temperatures, but might contain a phase of deconfined matter in the center. On the other hand, the early universe had a much smaller density, but due to the movement of the quarks, a formation of hadrons was impossible until the temperature drop below a critical value. The diagram also shows experimental results, that already indicate that this extreme form of matter is accessible in the laboratory.

1.3 Relativistic Heavy Ion Collisions

While the QGP probably existed in the early stages of the universe, and might still – or rather again – exist in the center of neutron stars, it is in these forms not directly accessible by experiments.

With accelerators, a tool is available to focus large amounts of energy to very small spaces, leading to very high energy densities. Usually these accelerators are used to collide electrons or protons, which yields the highest energy densities, but the system size in these collisions is not sufficient for the creation of a thermodynamical system. 30 years ago, in 1975 T.D. Lee suggested to distribute high energy over a large volume to study the bulk properties of a thermodynamical system governed by QCD [6]. The best method to achieve these high energy densities in relatively large systems in the laboratory is to collide heavy nuclei at high energies.

This idea has lead to a line of heavy-ion experiments at several accelerators. The first heavy-ion collisions were produced with the Bevalac at the Lawrence Berkeley National Laboratory in the 1970's. Later, a heavy-ion program was set up at the Alternating Gradient Synchrotron (AGS) at the Brookhaven National Laboratory on Long Island. Both of these accelerators provided heavy ion beams with energies up to several GeV per nucleon for fixed-target experiments, that did not reach the energy densities necessary for the creation of a Quark-Gluon-Plasma. The Super-Proton-Synchrotron at CERN in Geneva featured several fixed-target experiments with beam energies of up to 158 GeV per nucleon, which is equivalent to an energy in the center of mass system of $\sqrt{s_{NN}} = 17\,\mathrm{GeV}$. As illustrated in figure 1.3, the energy density in these collisions approached the phase boundary, and first evidence for a new state of matter was found [7]. Since then, the Relativistic Heavy Ion Collider (RHIC), located again at BNL, started operation in 2000. The collider design with two beams steered into head-on collisions allows energies in the center of mass system of $\sqrt{s_{NN}} = 200\,\mathrm{GeV}$, and opened up new opportunities for a better understanding of the properties of this new state. The next step in the pursuit of higher and higher energies will be the Large Hadron Collider that is currently under construction at CERN and that is scheduled to start operation in 2007 with energies up to $\sqrt{s_{NN}} = 5.5\,\mathrm{TeV}$.

At sufficiently high energies, the matter involved in a heavy-ion collision is expected to go through different phases. In the earliest moments of the collision, the nucleons of the two incoming nuclei collide as if they were independent interactions. It is in this phase that hard scatterings occur and produce heavy quarks and the most energetic partons that will later fragment into jets. Most of the incoming nucleons will however lose much of their kinetic energy in multiple collisions and thus create a region with a very high energy density filled with quarks and gluons. The strong interactions between the particles lead to a rapid distribution of the available energy over the accessible volume and thermal equilibrium. It is assumed that in this phase of the collision, the energy density is sufficient to produce a QGP. The high density and the resulting pressure cause the medium to expand and cool down, so that at some point the temperature drops below the critical temperature, deconfinement is no longer possible and the partons form hadrons again. This is the time when most of the observed particles are created. The dense hadron gas that results from the hadronization of the QGP still allows interactions between the hadrons and alters their kinetic properties. The expansion rapidly cools down the medium until the hadrons stop to interact and leave the interaction region towards the detectors.

The large size of heavy nuclei allows collisions at large impact parameters of up to twice the nuclear radius, which is 7 fm in the case of gold. The impact parameter determines the shape of the interaction region and the amount of nuclear matter that will participate in the collision: At an impact parameter of $b = 0$, the nuclei overlap completely, all nucleons participate in the collision and the collision region is rotationally symmetric. At non-zero impact parameters, the number of participating nucleons decreases, and the overlap region is almond-shaped. The produced hot medium is anisotropic and so is the further evolution of the system.

It is obviously not possible to measure the impact parameter directly, but due to its importance for the amount and shape of the hot matter created, it must be determined. An easy to measure observable that correlates well with the impact parameter, or centrality, of a collision is the particle multiplicity. For technical reasons, the reference multiplicity used to classify the centrality, is often determined from certain species of particles in a defined kinematic regions.

Most of the particles produced in a heavy-ion collision are created very late during the hadronization of the QGP. These particles can therefore only carry direct evidence of the latest stages of the collision, and any statement about earlier times depends on theoretical models extrapolating the measured observables to the initial conditions. As these particles usually carry small transverse momenta of less than 1-2 GeV, the study of these particles is usually called *soft physics.*

A more direct view into the earlier stages is possible with hard probes that are generated in the energetic scatterings in the first moments of the heavy-ion collision. Only these initial collisions provide the energy required to generate quarks, gluons or photons with high transverse momenta of more than 10 GeV/c, or very heavy particles like charm- and bottom-quarks. As the production of these particles occurs only at large momentum transfers, a good reference from perturbative QCD calculations and data from $p+p$ collisions is available. A comparison of heavy-ion and $p + p$ collisions can therefore isolate effects that are specific to the conditions found in the presence of heavy nuclei.

Chapter 2

High-p_T Physics and Jets

High-p_T physics in heavy ion collisions studies the production of particles with high transverse momenta above 5–10 GeV/c in collisions of large nuclei. The production mechanism of these particles is well understood in p+p collisions, which provide a good understanding of the phenomena relevant in these processes. A comparison of data from p+p and Au+Au collisions can then measure modification of high-p_T particle production in the presence of the hot and dense medium created in heavy-ion collisions. This chapter will give an overview over the concepts related to high-p_T particle production in heavy ion collision, as well as an overview of major measurements performed at RHIC.

2.1 Basic Concepts

The dominant production mechanism of high-p_T particles in hadronic collisions are hard scatterings of partons from the two projectiles. As a result of asymptotic freedom, these collisions can be treated as interactions of free particles, that can be calculated in perturbative QCD. These processes will be described in section 2.1.1.

The partons, whose interactions are described by pQCD, are experimentally only accessible in collisions of hadrons that contain these partons. The kinematics of parton collisions within a hadron collision depends on the structure of the hadrons, and can be characterized on a statistical basis. Section 2.1.2 explains the partonic structure of hadrons and the connection between hadronic and partonic collisions.

As quarks and gluons cannot exist freely, the scattered partons will transform into a cluster of hadrons, that are accessible to measurements. These clusters of spatially correlated particles are called jets, and due to momentum and energy conservation, carry information about the original parton. The transformation of a parton into a jet of hadrons is called fragmentation and will be described in section 2.1.3.

The large interest in the study of energetic partons in heavy ion collisions arises from the question about interactions of energetic partons with the hot medium created in these collisions. The production mechanism for hard probes is well understood in nucleon-nucleon collisions, and therefore provides a good reference. Comparing the observed jets in heavy ion collisions with jet production in nucleon-nucleon collisions will reveal the differences, and these differences can be attributed to the presence of the hot medium. The current understanding of this interaction between a QGP and an energetic parton traversing it will be described in section 2.1.4.

2.1.1 Hard Parton Scatterings

On the most elementary level in QCD, the production of hadrons can always be traced back to the production of quarks or gluons. QCD describes all hadronic collisions in terms of these interactions between partons of the incoming hadrons, rather than in terms of the hadrons themselves. In analogy to QED processes, QCD processes are often expressed in the form of Feynman diagrams, that give an intuitive picture of an interaction. The main difference to QED processes is the self-coupling of gluons, that is expressed in Feynman graphs by vertices connecting three gluons.

Figure 2.1 shows the Feynman graphs of a few example processes that can lead to the production of high-p_T partons, or jets. The first three panels show typical dijet production, where two jets are created from a single collision. Annihilation (a) and t-channel scattering (b) are analogous to QED processes, replacing the γ/Z^0 with a gluon. Panel (c) shows a t-channel scattering with a 3-gluon vertex, that is only possible in QCD. The last two feynman graphs depict processes that are no pure QCD process, but also contain the electro-magnetic radiation of a hard photon: panel (d) shows the annihilation of a quark-antiquark pair and creation of a gluon and a photon. The last panel shows a scattering of a gluon on a quark, analogous to an electromagnetic Compton scattering, and often also called (gluon) Compton scattering.

All these processes have in common, that hard particles are always produced in pairs to guarantee energy and momentum conservation. In the first three examples, these particles are partons, that will be observed as jets. Examples (d) and (e) result in $\gamma + \text{jet}$ events, where the momentum of a parton is balanced by a photon. Three-jet events have also been observed, but they can be interpreted as events where two high-p_T partons were created initially, and one of them radiated a hard gluon that appears as a third jet. While these events play an important role in high-energy particle physics, they have not yet been measured in heavy-ion physics.

Using these and higher order Feynman graphs, the cross sections for the relevant processes can be calculated. However, it is necessary, that the strong coupling constant α_s is sufficiently small, so that the series can be cut off at a manageable order while retaining sufficient precision. Perturbative QCD calculation can provide good precision only at sufficiently small α_s, which is why they can only describe particle production at high p_T, but not for soft particles.

2.1.2 Factorization

Although ideally, one would like to study collisions between elementary particles, practically this is not possible for QCD processes, because the elementary quarks and gluons

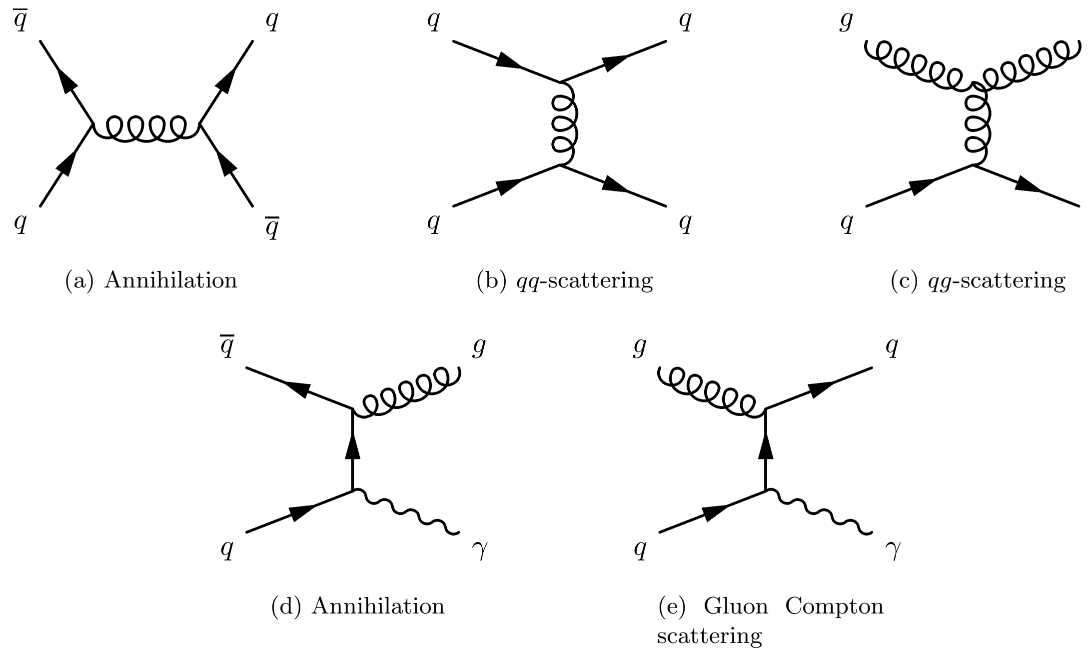

(a) Annihilation (b) qq-scattering (c) qg-scattering

(d) Annihilation (e) Gluon Compton scattering

Figure 2.1: Feynman graphs of typical processes generating high-p_T jets.

do not exist freely. Hadron collisions are thus the only available tool for the study of the strong interaction at high momentum transfers, but in this case, the complex structure of a hadron has to be taken into account.

This can be accomplished by using a feature of QCD called factorization [8], that opens a way to separate perturbative and non-perturbative effects in a hadron-hadron collision. When two hadrons A and B collide, the cross section to produce a jet can be written as:

$$\sigma_{AB\rightarrow jet+X} = \sum_{a,b} \iint dx_a dx_b f_{a/A} f_{b/B} \hat{\sigma}_{ab\rightarrow jet+X'} \tag{2.1}$$

In this formula, the particle distribution function (PDF) $f_{a/A}$, and analogous $f_{b/B}$, describes the probability to find a parton of species a in hadron A, carrying a momentum fraction x_a of the hadron A, i.e. $p_a = x_a p_A$. As these functions describe the non-perturbative domain of hadron structure, they cannot easily be calculated, and are usually measured in experiments. $\hat{\sigma}_{ab\rightarrow jet+X'}$ gives the cross section for the production of a jet in a collision of two free partons a and b, neglecting the fact that they are confined in the hadrons A and B. At sufficiently high energies, this cross section can be calculated in perturbative QCD, and — together with measured PDFs — can be used to calculate the cross section of a specific process in a hadron collision.

Figure 2.2 shows PDFs for different parton species in nucleons for different momentum transfers in the parton-parton collisions that measure the PDF. The shown PDFs are

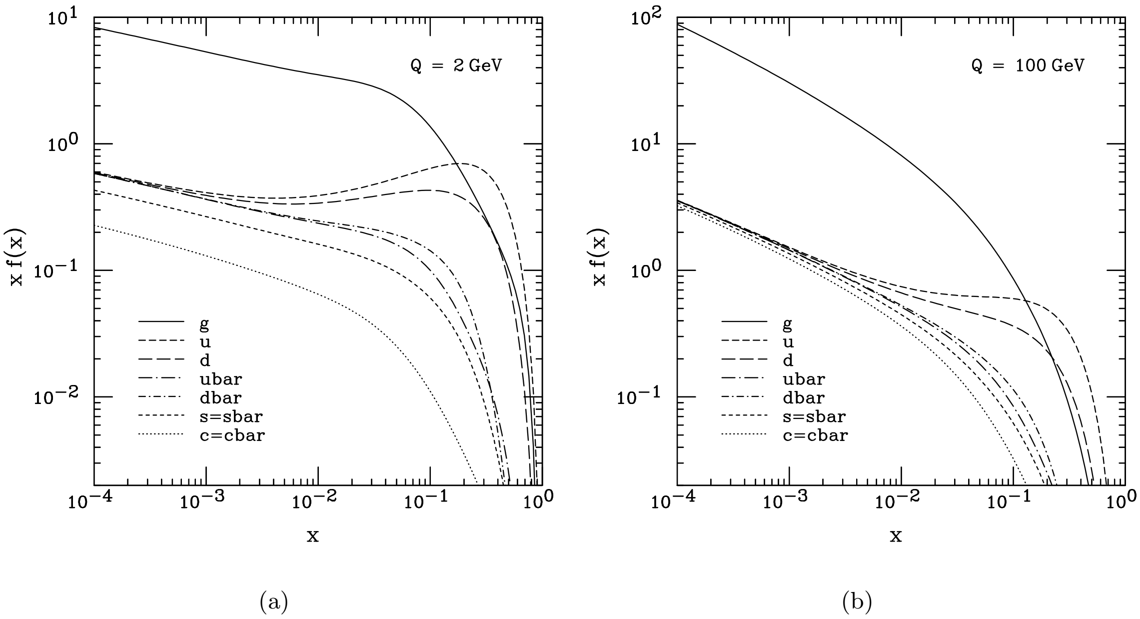

Figure 2.2: CTEQ6M parameterization of particle distribution functions for momentum transfers of $Q = 2\,\text{GeV}$ and $Q = 100\,\text{GeV}$ [9].

parameterizations of the available data [9]. Gluons play a dominant role for all but the highest momentum fractions x, where the contributions of up- and down-quarks increase due to their role as valence quarks. All other quark species, including anti-up- and anti-down-quarks, do not appear in hadrons as valence-quarks, but only as virtual sea-quarks, and therefore do not show this enhancement at high momentum fractions $x \approx 0.3$.

Although the same principles apply for nuclei, there are differences in the PDFs due to the density of strongly interacting matter. For low fractional momenta $x \leq 0.1$, the PDFs are depleted for nuclei, relative to a single nucleon [10] . This effect, called nuclear shadowing, can be explained in terms of fusion of low-x partons, leading to a suppression of low-x partons and shift towards higher x [11].

A consequence of factorizing hadron-hadron collisions into parton-parton collisions and PDFs is, that in general the center-of-mass system (CMS) of the parton-parton collision is not the CMS of the hadron-hadron collision, because the partons carry different momentum fractions of the respective hadrons. As the partons are bound in the hadrons, the momentum components transverse to the beam direction are very small, and so is the transverse velocity of the CMS. The CMS for the parton-parton collision is therefore boosted parallel to the beam axis, leaving the transverse momentum components of the participating particles unaltered, but changing the components parallel to the beam. As a result, the outgoing partons will no longer be back-to-back in three-dimensional space, but only in the projection onto the plane transverse to the beam axis.

2.1.3 Fragmentation

As quarks and gluons cannot exist as free particles, the parton picture can only describe an intermediate, but not the final state of the collision. The partons have to be transformed into hadrons in a process called fragmentation. The name "fragmentation" comes from the break-up of strings that mediate the strong force and connect to the high-p_T partons as they escape. Strings illustrate the long range behavior of QCD in a rather intuitive way. They connect two color charges, and can be seen as a kind of rubber band with a tension of 1 GeV/fm. As the partons fly apart, the string is expanded, and at some point the energy stored in the string is high enough to split the string, produce a quark-antiquark pair, and couple the generated quarks to the new ends of the split string. Along the string, several quark-antiquark pairs are created in this way, and these particles then form the hadrons that can be measured in an experiment. the process can be seen as the opposite of factorization: while factorization describes, how a hadron can be interpreted as a group of partons, fragmentation is a description of how partons can be measured as a group of hadrons.

The kinematic properties of these newly created hadrons are determined by the quarks and anti-quarks from the fragmentation of the string. Their momentum is oriented in the same direction as the expansion of the string, that is in the direction of the initial parton. The string therefore creates a cluster of spatially correlated hadrons, that is called a jet. Although the directions of the momenta of the hadrons in a jet are similar, the magnitude of these momenta can cover a wide range from zero to the momentum of the initial parton, reflecting the movement of the string at the time of breakup. The momentum spectrum of particles within a jet, expressed in terms of $x = p_h/p_{jet}$ rather than the momentum of the hadrons p_h, is called a fragmentation function.

Figure 2.3 shows fragmentation functions as measured by the ALEPH experiment [12], separated for several quark species (left panel) and gluons (right). The particle production is dominated by the low-x region, where hadrons carry a momentum that is only a small fraction of the momentum of the initial parton. On the other side, the probability to find a hadron carrying a large momentum fraction decreases strongly with x.

As a consequence of fragmentation, the measurement of a single particle gives only indirect information about the properties of the initial parton. To extract precise information about the initial parton, all particles of a jet have to be reconstructed to determine the momentum of the jet, and thus of the initial parton. In collisions of simple systems, like $e^+ + e^-$ or $p + p$, it is possible to group the particles into jets, and determine the properties of the partons created in these collisions. A multitude of jet algorithms have been developed to perform this task in these small systems [13, 14, 15], but have not yet been used in the high-multiplicity environment of a heavy-ion collision. The situation might improve with the advent of the LHC, but up to RHIC energies, the background from the underlying event is too high to be distinguished from jets at accessible energies. Thus, heavy ion physics has so far relied on single- or two-particle measurements to extract jet properties, with the result of large uncertainties in the initial parton's properties.

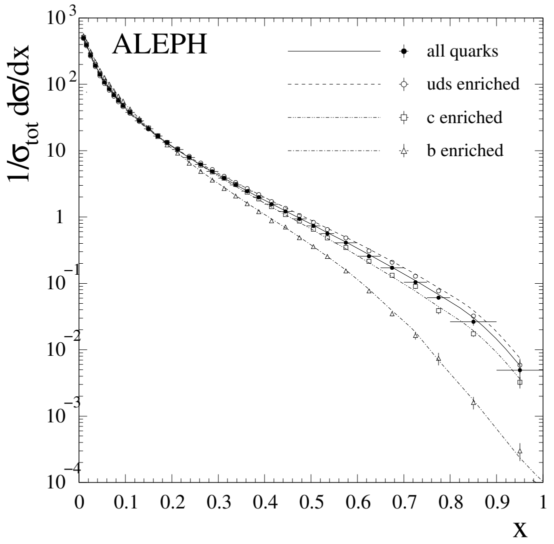

(a)

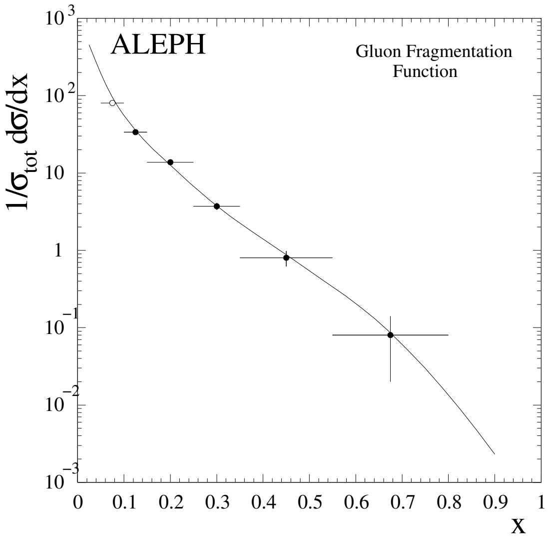

(b)

Figure 2.3: Inclusive fragmentation functions for quarks (a) and gluons (b), measured by the ALEPH Collaboration [12].

2.1.4 Parton Propagation

So far, only high-p_T hadron production in the vacuum has been discussed, where no medium can interact with the parton as it escapes from the collision region. In the presence of hot and dense nuclear matter, the parton could interact with the medium, and loose energy during the traversal. This effect has first been suggested by Bjorken [17], who assumed that an energetic parton traversing a QGP would loose energy in collisions with the partons in the plasma. The energy loss would depend on the travelled distance, and could be seen in the suppression of high-p_T particles from jets. A possible signature of this process has also been suggested by Bjorken: the suppression of di-jet events. Generally, the creation of one jet is accompanied by an opposite jet, but in the case of large energy loss in a medium, one or both jets could be suppressed or “quenched” due to the energy loss, and the event would appear to contain only a single jet. It has later been shown that the collisional energy loss had been overestimated, and could not create such strong effects [18]. It was however realized that radiative energy loss can reach the magnitude originally predicted for collisional energy loss, and although the underlying mechanism of energy loss is different from Bjorken's original scenario, it's consequences still hold on a qualitative basis.

The newly suggested energy loss mechanism is an analogon to bremsstrahlung in QED, i.e. the radiation of a gluon by an energetic parton traversing a medium [19]. In multiple interactions with the medium, gluons will be radiated off the energetic parton, resulting in

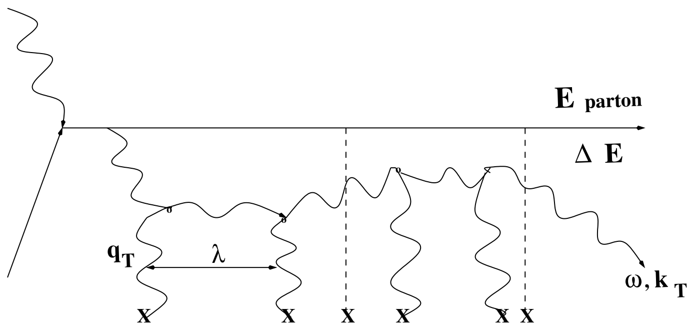

Figure 2.4: Typical gluon radiation diagram [16]

a decrease of the parton's energy, and a depletion of the hadron spectra at high transverse momenta. Due to the self-coupling of gluons, they will interact with the medium after they have been radiated off the parton, in contrast to QED bremsstrahlung, where photons do not interact with each other. Figure 2.4 illustrates these interactions, where the gluon interacts with scattering centers in the medium with a mean free path length of λ [16].

The induced energy loss ΔE of a parton traversing a QCD medium can be calculated within the BDMPS formalism [20]. If the partons travels a distance L within a medium, and suffers N interactions with scattering centers in the medium with a typical momentum kick of μ, and a mean free path length λ, then the energy loss is:

$$\Delta E(L) \sim \alpha_s \frac{\mu^2 L^2}{\lambda} \left(1 + O\left(1/N\right)\right) \tag{2.2}$$

To first order, the total energy loss is proportional to the strong coupling constant, the square of the mean momentum transfer, and the inverse of the mean free path length. Rather surprisingly, it is also proportional to the square of the travelled distance, meaning that the energy loss per unit length is not constant, but increases with distance.

The above equation only holds for a static QCD medium. In relativistic heavy-ion collision, the created medium expands at great speed, and this prerequisite is no longer satisfied. Due to the expansion, the density of the medium decreases, and therefore the energy loss per unit length decreases, counterbalancing the effect of increasing energy loss with travelled distance. For heavy-ion collisions, the energy loss is therefore assumed to be proportional to L, rather than L^2.

It should be noted, that although the parton energy decreases during the traversal through the medium, the lost energy is preserved in the form of the radiated gluons. Furthermore, the parton energy cannot be measured directly, but only after the fragmentation into a jet of hadrons. However, the gluons might fragment into hadrons as well, leading to a second "jet" overlaid over the jet of the energetic parton. In this case, production of low-p_T particles would be enhanced, because more relatively soft gluons would contribute to their production. On the other hand, the decreased energy of the parton reduces the production probability for particles with very high p_T. Particle production is shifted from high-p_T to low-p_T, an effect that could either be described as energy loss of the leading parton — but then the underlying particle production due to hadronization of the radiated gluons, has to be accounted for — or as a modification of the fragmentation function of the energetic parton. As a third scenario, the gluons could deposit their full energy in the medium, heating it up locally.

Depending on the studied energy range, either of these interpretations — energy and momentum transfer to the medium, modification of fragmentation functions, and energy loss of a parton combined with hadronization of radiated gluons — can explain the effects observed in experiments. Hadrons with very high transverse momenta above 3-4 GeV/c will reflect the energy loss, because the reduced energy of the parton suppresses the production of high-p_T particles, and the energy of the radiated gluons is not sufficient to counterbalance this effect in the high-p_T region. In the region of soft particle production, two scenarios mark the extremes, with reality somewhere in between: the radiated gluons might escape the medium without much further interaction, and subsequently fragment in the vacuum, or they might deposit all their energy in the medium, so that the energy and momentum of the hard parton is used to heat up the medium, and accelerate it in the direction of the parton. In reality, part of the energy will be used to heat the medium, and some gluons will escape the medium, leading to an interplay of the two effects.

2.2 High-p_T Physics at RHIC

The following section will summarize some important advances in high-p_T physics from the first RHIC runs, showing both experimental results and their interpretation. In the year 2000, RHIC opened up new possibilities in the exploration of the QGP with hard probes. The large cross section for hard processes at collider energies and the long runs of the dedicated heavy-ion machine allow for the measurement of hard probes with energies of several GeV.

2.2.1 Single Particle Suppression

Already the first run with Au+Au collisions at 130 GeV provided evidence of a suppression of particles with high transverse momentum [22, 23], which was studied in more detail during the following full energy runs [21].

Figure 2.5 shows the invariant p_T distribution of charged hadrons within $|\eta| < 0.5$ for Au+Au and p+p collisions at $\sqrt{s_{NN}} = 200\,\mathrm{GeV}$. A direct comparison of the spectra by eye is difficult due to the logarithmic scale of the vertical axis. For a comparison, the production rate relative to $p+p$ collisions is expressed in form of the nuclear modification factor R_{AA}, which is defined as:

$$R_{AA}(p_T, \eta) = \frac{d^2N^{AA}/dp_T d\eta}{T_{AA} \cdot d^2\sigma^{NN}/dp_T d\eta} \tag{2.3}$$

where $T_{AA} = \langle N_{bin} \rangle / \sigma^{NN}_{inel}$ accounts for the collision geometry. $\langle N_{bin} \rangle$, the number of binary nucleon-nucleon collisions occuring during the collision of the two nuclei, is generally determined by Glauber calculations.

R_{AA}, which is plotted in figure 2.6, clearly shows a suppression of high-p_T particles in central collisions: the yield of observed high-p_T particles is only about 20% of what would be expected if the collisions were a superposition of independent nucleon-nucleon collisions [21]. The data are compared to two different perturbative QCD calculations (pQCD-I [24] and pQCD-II [25]). These pQCD models calculate the energy loss of partons propagating in the dense medium created in heavy-ion collisions. For the pQCD-I model, two calculations that do not include the energy loss are also shown. The models including partonic energy loss can describe the general features of the p_T-dependence of the nuclear modification factor, while the shown models without energy loss can not.

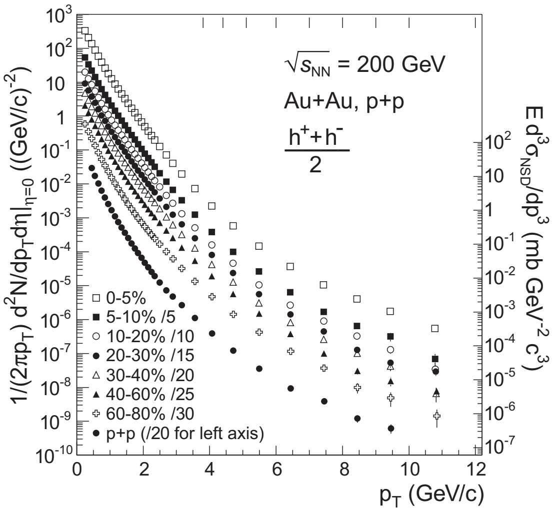

Figure 2.5: Inclusive invariant p_T distribution of charged hadrons $(\mathrm{h}^+ + \mathrm{h}^-)/2$ for Au+Au collisions at different centralities. For $p_T > 4\,\mathrm{GeV}/c$, the bin boundaries are marked at the top. The invariant cross section for p+p collisions is indicated at the right vertical axis. [21]

A different mechanism was suggested to explain the suppression of high-p_T particle production with initial state saturation effects, that would reduce the number of gluons in the incoming nuclei, and thus the number of produced energetic partons or jets. The result would also be suppression of high-p_T particles, that would however also be present in nuclear collisions where no QGP is created. For this cross-check, in 2003 RHIC was operated with a deuteron and a gold beam to provide d+Au collisions, that feature all initial state effects relevant for the relativistic gold nucleus, but do not generate the energy density and system size necessary for the creation of a QGP.

Figure **??** shows the p_T spectra for minimum bias and central d+Au collisions, and p+p reference data. Again, a comparison by eye is difficult, and therefore the nuclear modification factor R_{dAu} is defined in analogy to R_{AA}. R_{dAu} is shown in figure 2.7, and it clearly disagrees with the behavior of R_{AA} in central Au+Au collisions. The suppression of high-p_T particles can therefore be attributed to final state effects caused by the hot and dense medium created in central Au+Au collisions [26].

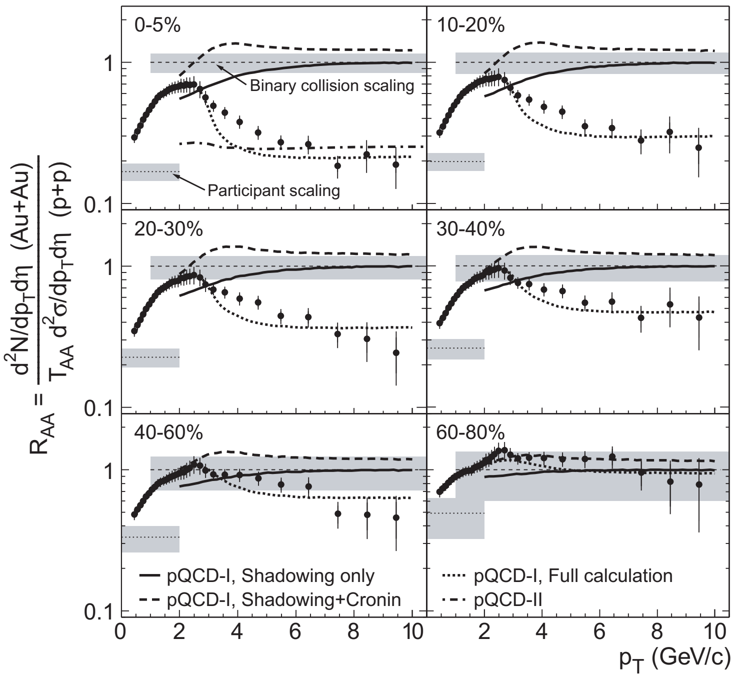

Figure 2.6: The nuclear modification factor $R_{AA}(p_T)$ is the ratio of observed particle yield in AA and pp collisions, scaled with the number of binary collisions. [21]

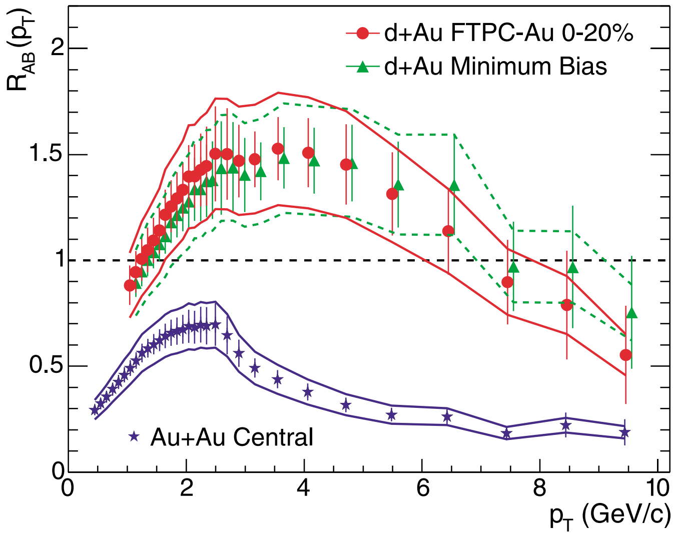

Figure 2.7: Nuclear modification factor $R_{dA}(p_T)$ for central and minimum-bias d+Au collisions, in comparison with R_{AA} from Au+Au collisions. $\sqrt{s_{NN}} = 200\,\text{GeV}$ for all systems. [26]

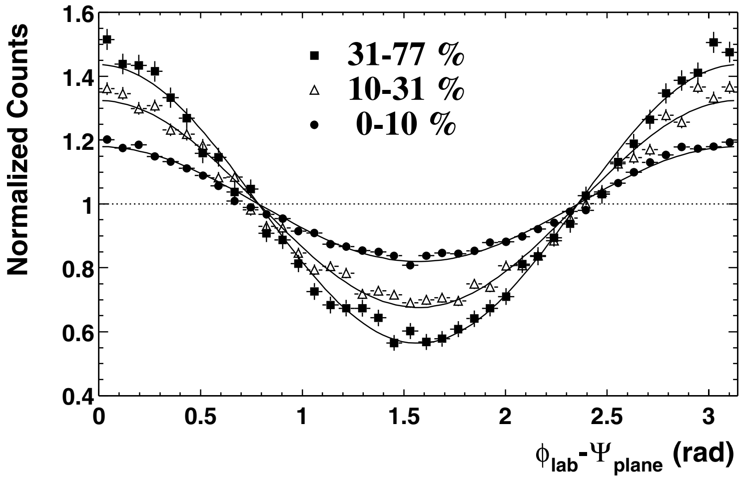

Figure 2.8: Azimuthal angle of high-p_T particles ($2 < p_T < 6\,\mathrm{GeV}/c$) with respect to the reaction plane for Au+Au collisions at different centralities for $\sqrt{s_{NN}} = 130\,\mathrm{GeV}$. [23]

2.2.2 Azimuthal Anisotropy

Unless two heavy nuclei collide at zero impact parameter, the overlap region will be ellipsoidal, rather than rotationally symmetric. This azimuthal asymmetry in coordinate space results in asymmetries of the pressure gradient in the medium, the resulting accelerating force, and finally the particle production. The anisotropy of the particle production is usually parameterized by the coefficients v_n of the Fourier decomposition of the azimuthal distribution of particles relative to the reaction plane. At mid-rapidity, the first azimuth-dependent term v_1 vanishes due to the forward-backward-symmetry of the event. The first non-trivial term is then v_2, which is often referred to as elliptic flow. At low transverse momenta, the asymmetry is well described by hydrodynamical calculations, that treat the medium as an expanding fluid [27].

Due to the asymmetry of the hot and dense phase in the collision, energetic partons created in hard initial scatterings will traverse different path lengths to leave the medium, depending on the emission angle relative to the reaction plane. The average energy loss of a parton is then a function of the azimuthal angle, which introduces further anisotropies in the production of high-p_T particles, apart from hydrodynamical flow. The energy loss of these partons can be combined with hydrodynamical calculation, to account for the evolution of the hot phase, and the path length of energetic partons inside this phase, to predict the anisotropy of high-p_T particle production. The energy loss leads to a reduction of v_2 compared to a pure hydrodynamical calculation [28].

Figure 2.8 from [23] shows the normalized distribution of charged high-p_T particles for different impact parameters, as a function of the azimuthal angle of the particle relative to the reconstructed event plane $\phi_{lab} - \Psi_{plane}$. The anisotropy parameter v_2 is extracted by fitting with a function $1 + 2v_2 \cos 2(\phi_{lab} - \Psi_{plane})$.When the fit is performed for hadrons in

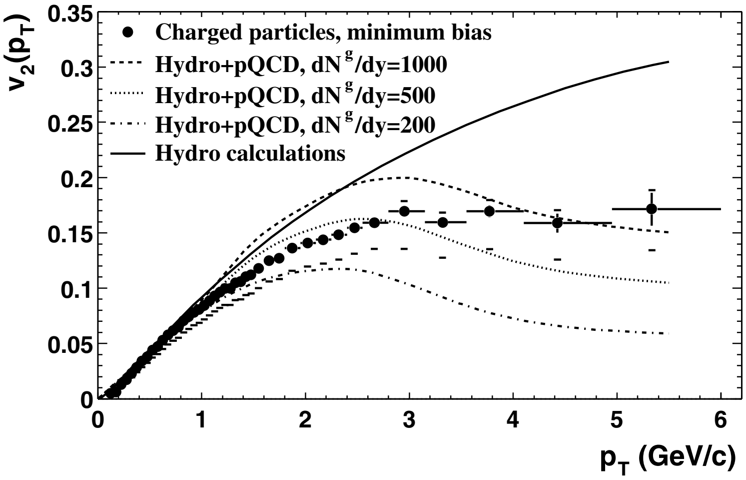

Figure 2.9: $v_2(p_T)$ for minimum bias Au+Au collisions at $\sqrt{s_{NN}} = 130\,\mathrm{GeV}$. The data is compared to a hydrodynamical model with and without partonic energy loss in the medium. [23]

different p_T bins, the anisotropy can be determined as a function of transverse momentum, as shown in figure 2.9. The data are compared to a pure hydrodynamical calculation, and calculations taking different values of partonic energy loss into account. The calculation without energy loss overestimates the anisotropy v_2, by up to a factor two at high transverse momenta. Calculations that take the energy loss into account, give a much better approximation: the saturation of v_2 as well as the magnitude of the effect agree with the data. The decrease at high p_T has however not been observed.

Although this explanation does not rule out alternative models, it supports the interpretation, that single particle suppression is caused by partonic energy loss.

2.2.3 Azimuthal Correlations

Perhaps the most spectacular manifestation of high-p_T suppression during the first RHIC runs was the disappearance of back-to-back correlations of high-p_T particles in the most central events.

Jets are usually produced in pairs, that are back-to-back in the transverse plane, and are separated by an azimuthal distance $\Delta\phi \approx \pi$. The jets themselves are closely correlated clusters of particles. They can be revealed by studying azimuthal correlations between a trigger particle with very high transverse momentum, and associated high-p_T particles from the same event. The first analysis of RHIC data using this method [29] selected charged trigger particles with a transverse momentum $p_T^{trigger} > 4\,\mathrm{GeV}/c$, where multiple trigger particles per event were allowed. Associated particles with $2 < p_T^{assoc} < 4\,\mathrm{GeV}/c$ were then chosen from the same event, and combined to pairs with the trigger particles.

The distribution of azimuthal angles between trigger and associated particles for different impact parameters is shown in figure 2.10. The data shows a sinoidal background, and on top of the background two peaks at $\Delta\phi \approx 0$ and $\Delta\phi \approx \pi$.

The level of background increases from peripheral to central events due to an increasing probability for random combinations of particles fulfilling the cuts for trigger and associated particles. The shape of the background is caused by anisotropic high-p_T particle production as described in the previous section: the $\cos(2\phi)$ shape of the distributions for trigger and associated particles also leads to a $\cos(2\phi)$ shape for the difference of the azimuth for random combinations of trigger and associated particles, as described in detail in appendix B. The random background can be determined by fitting the measured distribution between the two peaks with a function of the expected form.

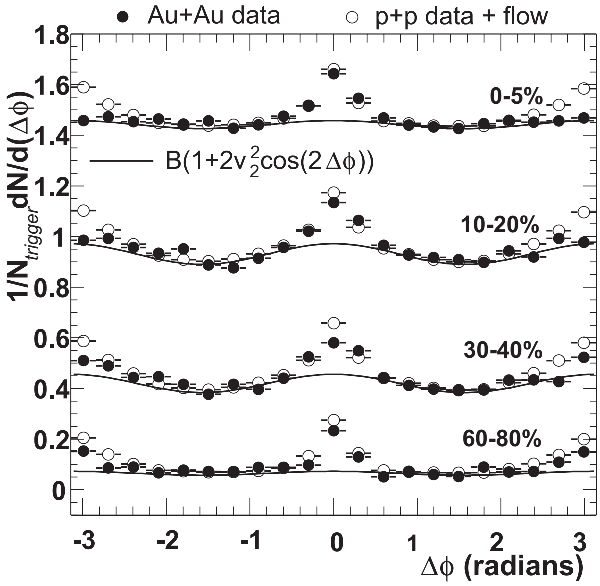

Figure 2.10: $\Delta\phi$ correlations of trigger particles with $4\,\mathrm{GeV} < p_T < 6\,\mathrm{GeV}$ and associated particles with $2\,\mathrm{GeV} < p_T < 4\,\mathrm{GeV}$. Au+Au data is compared to p+p reference data and the modeled background in nuclear collisions due to flow. [29]

The two peaks on top of the background are attributed to particles from the same jet (near-side, $\Delta\phi \approx 0$), and the opposite side jet balancing the momentum (away-side, $\Delta\phi \approx \pi$). For comparison, p+p reference data is shown on top of the background for all centrality bins. It can be seen, that the number of associated particles per trigger particle on the near-side does not depend strongly on centrality, and even in p+p collisions, a similar value is observed. It seems that the jets that actually escape the medium show very similar fragmentation to jets in the vacuum. The yield of jets per binary collision is different for p+p and peripheral and central Au+Au collisions, but as the yield is normalized to the number of trigger particles instead of the number of binary collisions, this is not seen in the correlation plots.

On the away-side, the correlation disappears when going from p+p over peripheral to central Au+Au collisions. In this case, both partons created in a hard scattering have to traverse the medium in opposite directions, and therefore the chance that at least one will loose a large amount of energy and "disappear" is very large.

The evolution of near- and away-side peak is shown in figure 2.11. The number of associated particles above background in the near-side peak increases slightly for increasing centrality. On the away-side, a dramatic decrease of the correlated yield is observed: the data is consistent with a complete disappearance of the away-side peak in central collisions.

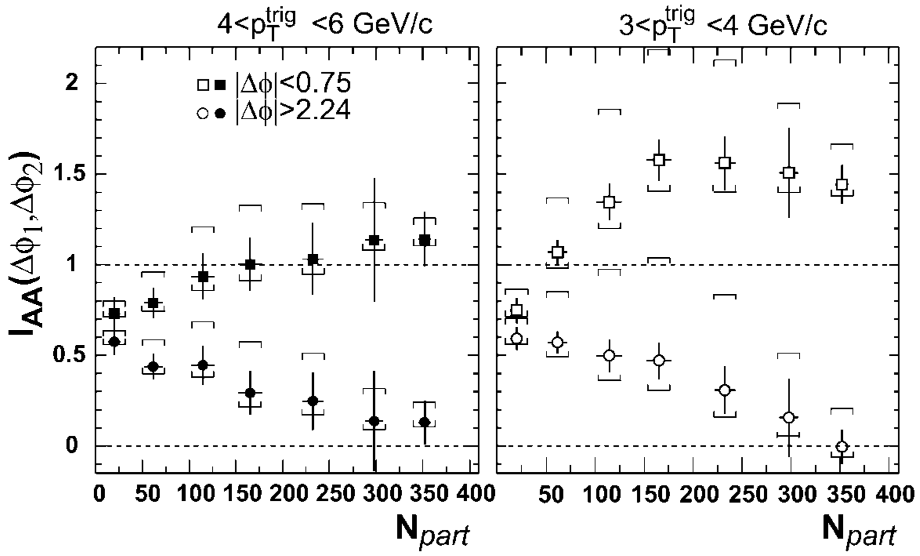

Figure 2.11: Associated near- and away-side yield for $\Delta\phi$ correlations [29]

The strong modification of the away-side, and the small near-side effects can be explained by a scenario called surface emission: only partons that were created close to the surface of the medium can escape radially outwards and will survive, while the opposite parton, that travels into the medium, will loose much of its energy, and no longer be visible.

Large energy loss of energetic partons can reduce the energy of the jet sufficiently, that the fragmentation into particles with transverse momenta $p_T > 2\,\mathrm{GeV}/c$ is strongly suppressed, and thus gives a natural explanation for the disappearance. However, alternative calculations claimed to provide an explanation that did not require the existence of a QGP, but a modification of the initial state of the colliding gold nuclei. Initial state effects would also be seen in d+Au collisions, that can be used to distinguish the scenarios.

The measurement of azimuthal correlations in d+Au events was possible with the d+Au data from the RHIC run in 2003. Figure 2.12 shows a comparison of azimuthal correlations in p+p, d+Au and Au+Au collisions. The strong suppression of the away-side peak is unique for central Au+Au collisions, and is not visible in any other system. We can conclude, that the suppression is a final state effect, that depends on the presence of the hot and dense matter created in heavy ion collisions.

2.3 Summary

High-p_T physics has become one of the major topics of heavy-ion physics in the RHIC era. Clear evidence of hard initial scatterings and the production of jets was obtained during the first RHIC runs from spectra and azimuthal correlation measurements. A strong suppression of high-p_T particle production has been observed in central Au+Au collisions,

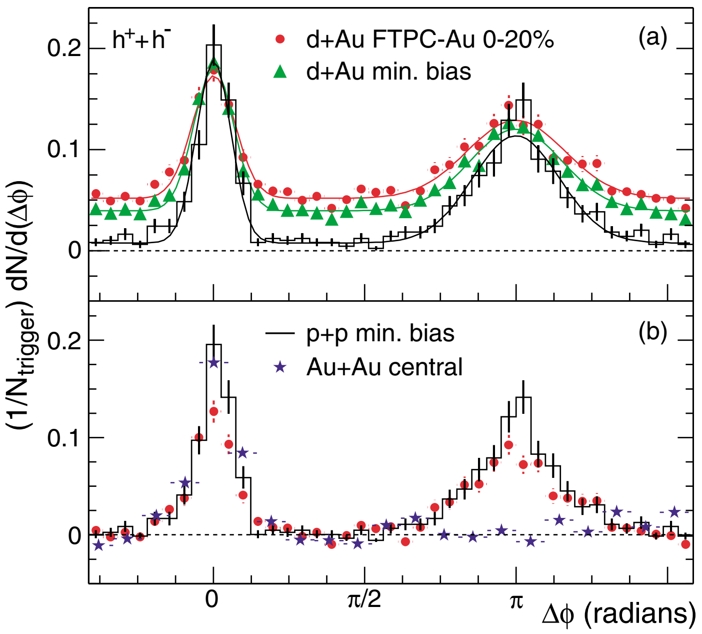

Figure 2.12: $\Delta\phi$ correlations in d+Au and central Au+Au collisions [26]

both for single particles as well as correlations. The comparison with peripheral Au+Au, d+Au and p+p reference data indicates, that this suppression depends on the presence of a large volume with strongly interacting matter at high temperature and density. The suppression can be attributed to the energy loss of partons traversing a hot and dense QCD medium.

Although large partonic energy loss is established and generally accepted in the community as a qualitative effect, the data available from the first three RHIC runs does not provide the means to reach a quantitative understanding of the interaction between an energetic parton and a QGP.

The field of $\Delta\phi$ correlations seems to be very promising for the near future. First analyses measure the “lost” energy, that is radiated in the form of gluons, and has to lead to increased particle production at low transverse momentum [30].

It will be interesting to raise the energy of the trigger particle, to see when the energy of a parton can no longer be absorbed by the medium, and when the away-side peak will reappear. In this case, one would still have to deal with the energy loss of the jet containing the trigger particle. Because it is unknown, where in the medium the jet was created, it is also unknown how large the energy loss was until the parton reached the vacuum. The already unprecise correspondence between the momentum of the trigger particle and of the initial parton is smeared out even more.

An ideal probe to study the energy loss of a parton are $\gamma +$jet events, where one energetic parton is not balanced by another parton, but by a photon. The photon does not interact with the medium and is not subject to fragmentation. It can therefore provide the best determination of the jet energy that is possible in the high-multiplicity environment of a heavy-ion collision.

Chapter 3

Experimental Setup

3.1 The Relativistic Heavy Ion Collider

The data for this thesis has been taken at the Relativistic Heavy Ion Collider (RHIC) at the Brookhaven National Laboratory (BNL). The BNL has been the primary site for heavy ion research in the United States since the construction of the Alternating Gradient Synchrotron (AGS), and this role was confirmed by the choice to build RHIC at the BNL.

The main focus of RHIC — as already the name implies — is on relativistic heavy ion physics, the discovery and study of the quark-gluon-plasma. However, a second scientific program investigates the spin structure of the proton and the polarization of gluons. This spin program requires polarized proton beams that can also be produced with RHIC.

Several experiments use the RHIC facility to take data: STAR[1] and PHENIX[2] are two large collaborations that participate in the heavy ion as well as in the spin physics programs at RHIC. PHOBOS[3] and BRAHMS[4] are smaller experiments that concentrate on the heavy ion program, and the youngest and smallest experiment pp2pp concentrates on the spin program.

3.1.1 The RHIC Complex

Before RHIC, heavy ion physics was done at fixed-target experiments where a beam is steered onto a solid target in front of the experiment. While this concept allows for high interaction rates, it is not suitable to achieve very high energies. To achieve these energies, it is preferable to use two beams and bring them into head-on collisions; an accelerator based on this concept is called a collider.

To reach energies much higher than those achieved in previous heavy ion programs at

[1] Solenoidal Tracker At RHIC

[2] Pioneering High Energy Nuclear Physics Experiment

[3] The proposal for mars MARS (Modular Array for RHIC spectroscopy) was rejected, but later a similar proposal under the name PHOBOS, one of the moons of mars, was accepted.

[4] Broad Range Hadronic Spectrometers Experiment at RHIC

Figure 3.1: The RHIC Accelerator Complex

the AGS and SPS[5] at CERN, the new machine had to be built as a collider. The result was an increase of more than a factor of 10 in the available energy in the center-of-mass system (CMS): the SPS used a Pb-beam with an energy of 158 GeV per nucleon to achieve an energy of only $\sqrt{s_{NN}} = 17\,\mathrm{GeV}$ per nucleon pair. This compares to an energy of $\sqrt{s_{NN}} = 200\,\mathrm{GeV}$ per nucleon pair for the two colliding $100\,\mathrm{GeV}/u$ Au-beams at RHIC.

The collider concept requires two accelerators that overlap only in a few regions where the beams are steered into head-on collisions, but that use different beam-lines for the rest of the beam trajectories. In the case of RHIC the two accelerators that are called yellow and blue ring intersect in six interaction regions. These interaction regions are located on six straights which are connected by six arcs that give RHIC its distinctive hexagonal shape. The experiments are located at the interaction regions.

As RHIC cannot accelerate particles from rest, the existing AGS complex is used to prepare the beams for injection into RHIC. In the case of heavy ions, the way to RHIC begins in the Tandem Van De Graff facility, where gold ions are accelerated to an energy of $1\,\mathrm{MeV}/u$

[5]Super Proton Synchrotron

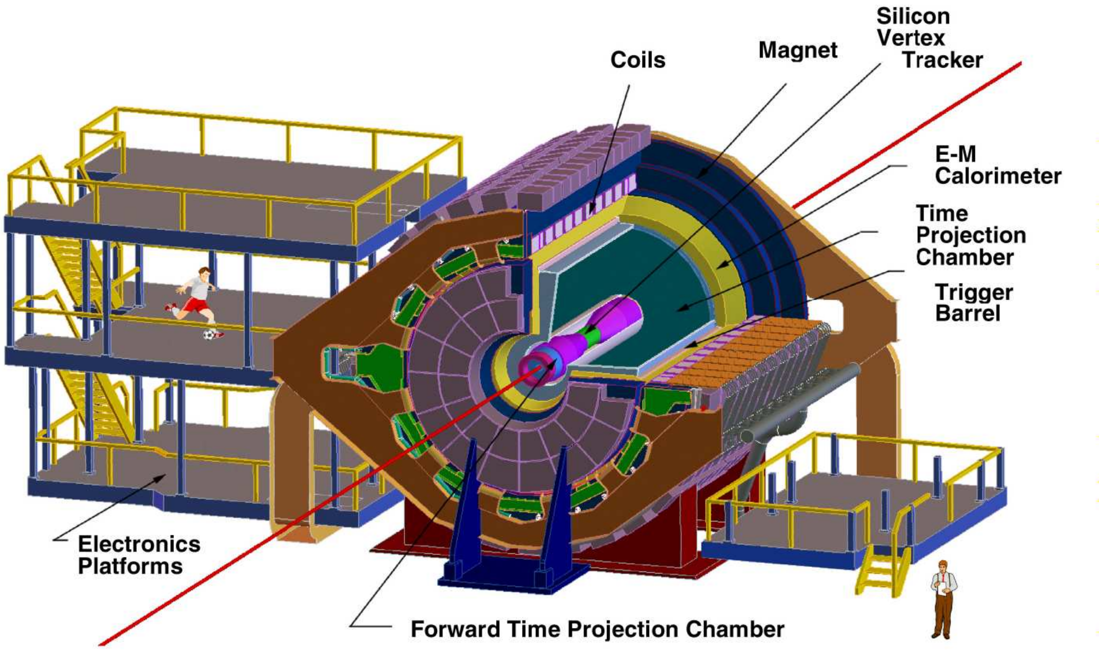

Figure 3.2: View of the STAR Experiment

and stripped to a charge of $Q = +32$. These ions are then guided through the Tandem-to-Booster transfer line to the Booster Accelerator, where they are accelerated to $95\,\mathrm{MeV}/u$. After leaving the Booster, the ions are further stripped to a charge of $Q = +77$ and injected into the AGS. After acceleration to $10.8\,\mathrm{GeV}/u$, the beam leaves the AGS into the AGS-to-RHIC transfer line, where the last two electrons get stripped, and the resulting Au^{79+} ions get injected into RHIC. RHIC then accelerates the ion beams to a maximum energy of $100\,\mathrm{GeV}/u$ and steers the beams into collision.

For proton running, the Linac is used as the source instead of the Tandem Van De Graff. The protons produced by the Linac are injected into the Booster, from where they take the same way as heavy ions.

3.2 The STAR Experiment

The Solenoidal Tracker at RHIC, or STAR, is one of the two bigger experiments taking data at RHIC. The collaboration consists of more than 500 people at 51 institutions in 12 countries.

The ability to measure decay products and large-angle correlations played a key role in the design of STAR. This goal was achieved by providing full azimuthal coverage in the mid-rapidity region from $-1 < \eta < 1$. Several other detectors provide additional coverage in the forward region.

The principal detector of STAR is the large volume Time Projection Chamber (TPC). The TPC has a cylindrical shape with a length of 4.2 m and a radius of 2 m, aligned along the beam pipe. It provides tracking information in the mid-rapidity region and limited particle identification using the specific energy loss of particles traversing the gas volume. A short overview will be given in 3.2.1, and a more detailed description can be found in section [31].

Inside the TPC, the Silicon Vertex Tracker (SVT) and the Silicon Strip Detector (SSD) provide additional tracking information to improve the extrapolation of tracks to the vertex [32, 33]. The primary goal for these detectors was the measurement of the secondary decay vertices of strange particles, that can improve the signal-to-background ratio for these signals. Analyses using only TPC data performed surprisingly well in the reconstruction of strange particles. By now, upgrades the silicon detectors in the inner tracking system are planned, which will be able to reconstruct secondary vertices of the decay of charm- and bottom-quarks.

Surrounding the TPC is the Central Trigger Barrel (CTB), an array of 240 scintillator modules acting as a trigger and multiplicity detector. It is planned to replace the CTB with a Time-of-Flight detector (TOF) to improve the particle identification. Prototypes for a TOF have already been in operation for several runs, but only with very limited coverage, replacing 2-3 CTB modules. When a large-acceptance TOF replaces the CTB, it will also take over triggering capabilities.

The outermost layer of detectors is the Electromagnetic Calorimeter (EMC), useful for the detection of photons, identification of electrons and the reconstruction of neutral pions. The EMC is divided into two sections: the Barrel EMC covers the mid-rapidity region between $-1 < \eta < 1$ and the Endcap EMC, mounted between the endcaps of the TPC and the magnet, extends the coverage to $\eta = 2$.

These detectors are enclosed in a solenoidal magnet providing a field of $B = 0.5\,\mathrm{T}$ [34]. The magnetic field bends the trajectories of charged particles and thus permits momentum measurements.

The Forward Time Projection Chambers (FTPCs) extend the tracking capabilities of STAR to the forward and backward regions from $2.5 < \eta < 4.0$ [35]. The FTPCs also provided a centrality measure for the d+Au run in 2003, where a TPC based centrality as used for Au+Au would have introduced a large bias.

Two Zero-Degree calorimeters (ZDC)are located 18.25 m from the center of the interaction region, between the beam-pipes for the two RHIC rings. Spectator neutrons produced in nucleus-nucleus collisions will travel along the beam-pipe, and finally hit the ZDCs. The signal from these spectator neutrons can then be used as a trigger for STAR.

3.2.1 Time Projection Chamber

The Time Projection Chamber (TPC) is the main tracking detector of STAR. It covers a rapidity region from $-1.8 < \eta < 1.8$ through the full azimuthal angle. Momentum information is available for particles in a momentum range between $100\,\mathrm{MeV}/c$ and $30\,\mathrm{GeV}/c$,

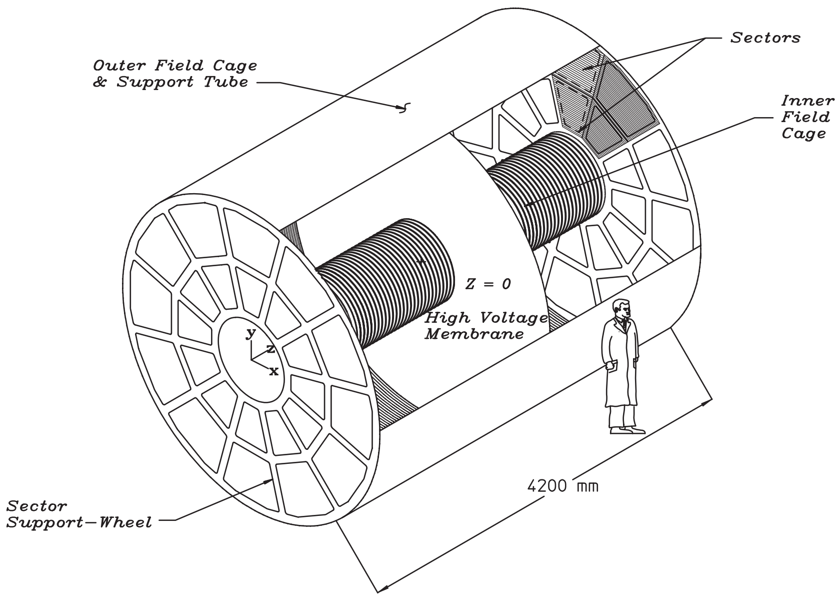

Figure 3.3: Schematic view of the TPC. A voltage of 28 kV between the central membrane and the endcaps generates an electric field that lets ionization electrons drift to the read-out sectors in the endcaps. Inner and outer field cage ensure a uniform electric field in the drift volume [35].

and particle identification is possible up to 1 GeV/c. The TPC can handle the high multiplicities of several thousand tracks within its acceptance for the most central Au+Au collisions [31].

The TPC is a large volume filled with P10 gas, consisting of 90% argon and 10% methane. The gas is contained in a cylinder with a length of 4.2 m, an outer radius of 2 m and an inner radius of 0.5 m, as shown in figure 3.3. In the center of the TPC, perpendicular to the cylinder axis, is the central high voltage membrane, which in conjunction with the inner and outer field cages and the endcaps provides a nearly homogeneous electric field of 135 V/cm.

The TPC is located inside the magnetic field of $B = 0.5$ T which forces charged particles on helix-shaped trajectories and allows the determination of a particle's momentum from the curvature of the helix. When a charged particle traverses the gas, it ionizes the argon atoms along its path. The electric field inhibits the recombination of the generated electrons and the ions and drifts the electrons to the endcaps. Collisions with the gas molecules balance the electric force, so that the electrons drift with constant velocity of 5.45 cm/μs.

The drift of the ionization electrons ends in the endcaps of the cylinder, where the read-out system is located. Each endcap consists of 12 multi-wire proportional chambers (MWPCs)

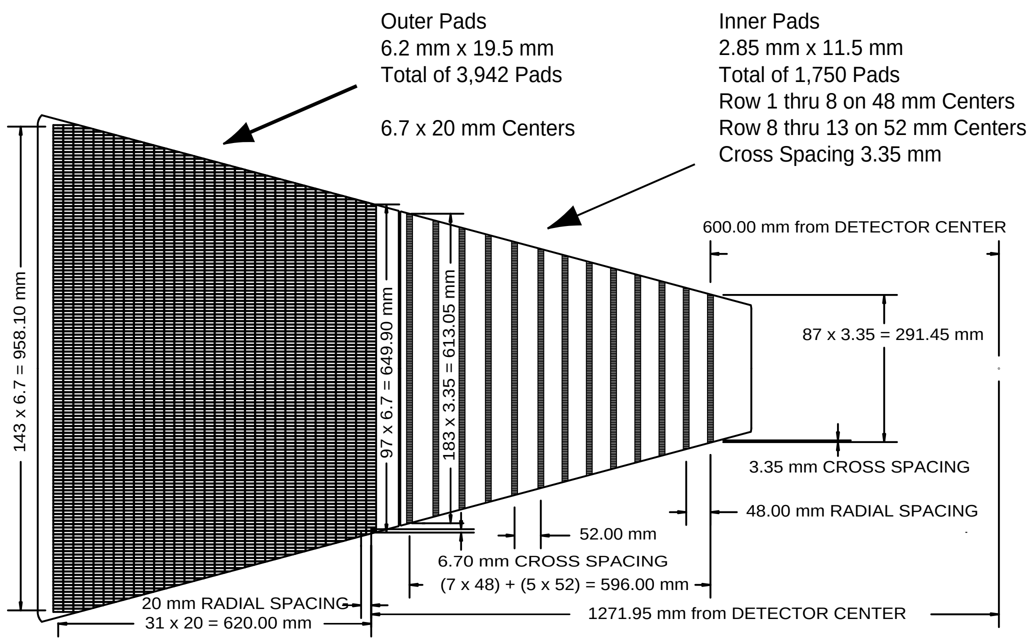

Figure 3.4: Pad-plane of the TPC. The inner 13 padrows with small pads provide good position and two-track resolution, while the outer 32 rows with larger pads are densely packed to optimize the collection of ionization electrons.

with pad readout, each covering one sector of 30°. In the MWPCs, 20 μm thick anode wires produce a radial electric field strong enough to let the electrons avalanche, leading to an amplification of the ionization signal. After the electrons from the avalanche have been absorbed by the anode wires, the remaining ions generate an image charge on the readout pads, which is amplified electronically and digitized.

The pad layout of one MWPC can be seen in figure 3.4: the plane is divided in an inner sector with a large number of small pads, that are organized in widely spaced rows, and an outer sector with larger pads in densely packed rows. The design was optimized for good position and two-track resolution in the inner region with higher particle densities, and precise measurement of the energy loss by ionization in the outer region with lower particle densities.

For each collision, each pad is read out 512 times, giving timing information for every electron cloud reaching the MWPC. The drift time between the collision and the arrival of the electron cloud at the MWPC can be converted the distance that the cloud drifted. Using this distance and the pad position allows to reconstruct the location of primary ionization, where a charged particle traversed the TPC volume.

The use of TPC information requires the reconstruction of the particle trajectories. This is done in two steps: in the first step, called cluster-finding, contiguous regions of ionization within the same padrow are localized. For each of these clusters, the center-of-gravity of

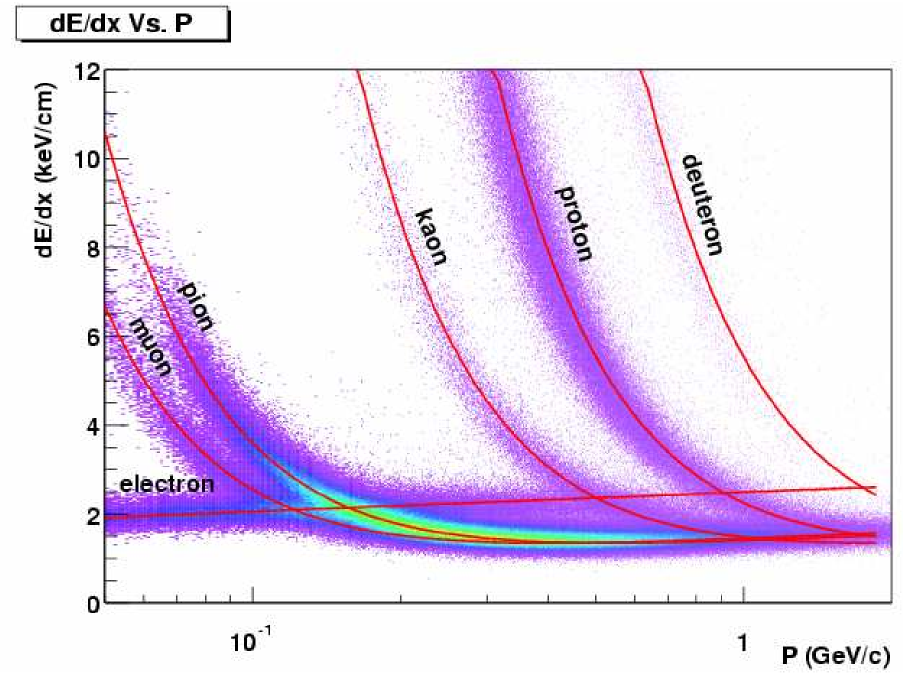

Figure 3.5: Specific energy loss of charged particles measured by the TPC. Each charged particles species shows a separate band, allowing for limited particle identification up to $1\,\mathrm{GeV}/c$. [31]

the charge distribution as well as the total charge is recorded. The result is a set of space-points, where charged particles ionized the drift gas. In a second step, called track-finding, clusters from the same particle have to be identified and combined to tracks. These tracks are fitted with the model of a helix, that describes the trajectories of charged particles in the homogenouos magnetic field. The momentum measurement of the particles uses the curvature of the helix in the transverse plane caused by the magnetic field. Thus the momentum resolution is determined by the resolution of the curvature and therefore by the spatial resolution of the TPC.

The TPC also has limited particle identification capabilities taking advantage of the specific energy loss of charged particles in a medium as described by the Bethe-Bloch formula:

$$\frac{dE}{dx} = -\frac{2\pi N_A z^2 e^4}{mc^2\beta^2}\frac{\rho Z}{A}\left\{\ln\frac{2mc^2\beta^2 E_M}{I^2(1-\beta^2)} - 2\beta^2\right\} \tag{3.1}$$

The charge z and the velocity β of the particle traversing the TPC gas are its only properties entering in this formula. The relevant properties of the drift gas are atomic number Z, mass number A, density ρ and the specific ionization I. E_M is the maximum energy transfer in one interaction. Apart from this, the mass m and charge e of the electron, the speed of light c and the Avogadro number N_A enter into the formula [36].

Most of the particles seen by the TPC carry a single unit charge e, and therefore the ionization is simply a function of the velocity β of the particle. Figure 3.5 shows the specific energy loss for different particle species.

3.2.2 Electromagnetic Calorimeter

While the TPC is a versatile tool for the measurement of charged particles, it is blind to neutral particles. Probably the most important class of neutral particles for the understanding of heavy-ion collisions are photons, which can be detected by their creation of electromagnetic showers in a high density material: in the presence of a heavy nucleus, an energetic photon can be converted into an electron-positron-pair. The nucleus, or a different particle, is necessary to allow for energy and momentum conservation. The electron and positron will again interact with the material, usually in bremsstrahlung processes that create energetic photons again. The mutual creation of photons on one and electrons and positrons on the other side continues until the energy of the particles is no longer sufficient for bremsstrahlung and pair-production. The cascade of electrons, positrons and photons is called an electromagnetic shower. Of course, a shower can also be created by an electron that traverses the medium. It should also be noted, that one of the most abundant hadrons, the neutral pion, decays almost exclusively into two photons, and is usually detected by measuring the daughter photons of this decay.

Experimentally, electromagnetic showers are used in electromagnetic calorimeters that consist of a high-density material for the creation of the cascades, and detector elements to detect the shower. The calorimeters can be classified in two groups: homogeneous calorimeters, where one material takes over the roles of shower and subsequent signal generation simultaneously, and heterogeneous sampling calorimeters, where passive high-density material is used for the creation of showers, and active detector components are incorporated in the structure to sample the created showers.

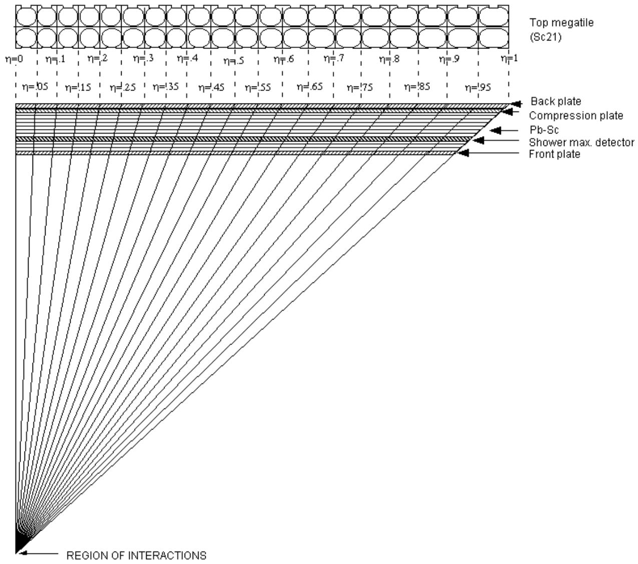

Figure 3.6: Side vie of a BEMC module, showing the projective geometry of its towers, pointing to the interaction region. [37]

In STAR, electromagnetic calorimetry is provided by two calorimeters: the Barrel Electro-Magnetic Calorimeter (BEMC) surrounding the outer field cage of the TPC is designed to cover the mid-rapidity region from $-1 < \eta < 1$, and the Endcap Electro-

Magnetic Calorimeter (EEMC), mounted on the inside of the magnet endcap, covers the pseudo-rapidity region from $1 < \eta < 2$. Although built as two separate subsystems, the calorimeters have a very similar design. Due to the large coverage — $60\,\mathrm{m}^2$ for the BEMC — a cost-efficient technology had to be chosen: the calorimeters have been constructed as sampling calorimeters using lead as passive material and plastic scintillator for signal generation.

The BEMC is divided into 120 modules, each covering one unit in rapidity and 6°in azimuth. 60 of these modules surround each half of the TPC, giving full azimuthal coverage. The cross section of one module is shown in figure 3.7. Each module consists of 20 layers of 5 mm thick lead plates, alternating with 21 layers of plastic scintillators. The total radiation length of this structure is $20X_0$ at $\eta = 0$. The scintillators are subdivided into 2 sections in azimuth by 20 sections in pseudo-rapidity. A stack of corresponding sections in all 21 scintillator layers is called a tower. The subdivision of the modules is projective, meaning that all towers are oriented towards the interaction region in the center of STAR, as illustrated in figure 3.6. Each of these towers measures 0.05 units in pseudo-rapidity by 3°or about 0.05 radian in azimuth. The constant tower size in units of pseudo-rapidity results in an increasing size of the towers in z-direction.

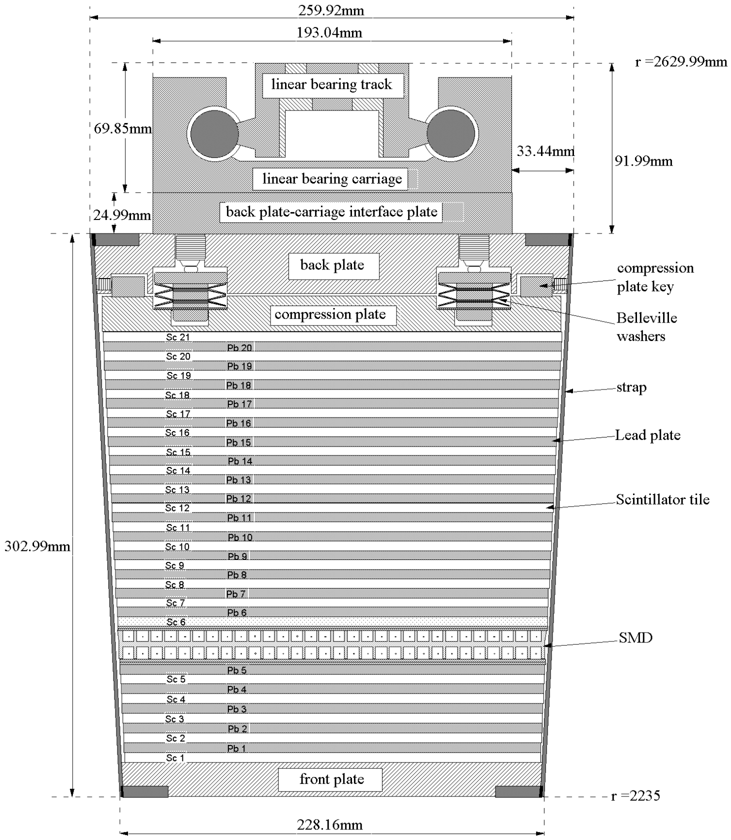

Figure 3.7: Cross section of a BEMC module. Layers of lead to generate electromagnetic showers alternate with scintillators to collect the signal. The SMD is located behind the fifth layer. [37]

The signals from the scintillators of one tower are transferred via fiber links to a photomultiplier tube (PMT), that converts the light pulse to an electrical signal, that is digitized by a 12-bit ADC. The gain of the PMTs can be adjusted by the high voltage applied to the dynodes to the tube. This gain adjustment is used to calibrate the EMC, so that the ADC values are proportional to E_T and can be used to trigger on towers with high transverse energy deposition.

The coarse spatial resolution of the towers is improved by a Shower Maximum Detector (SMD) that is located behind the fifth layer of lead. The SMD is a wire proportional counter with gas amplification. Its structure is based on an extruded aluminum profile with channels running parallel to the module. Each channel features an anode wire that provides gas amplification for charge deposited in the gas in the channel. Segmented PCBs cover the open sides of the extrusion profile, and sense the induced charge from the charge amplification. The induced charge can be amplified and digitized, and provides information about the shower activity in the area covered by the segment of the PCB. The PCBs are divided into strips that run across the module in the front and along the module in the back plane of the SMD. The strips on the front plane measure about 23 cm or 0.1 radians by 0.0064 in η. The strips on the back plane have a length of 0.1 units in η by 1.33 cm. This two-layer design allows independent measurements of the shower profile in η and ϕ with a spatial resolution of a few mm [37].

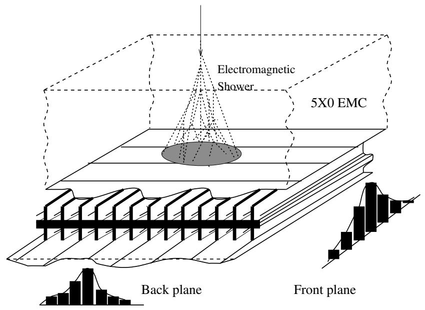

Figure 3.8: Schematic view of the Shower Maximum Detector of the Barrel EMC. The profile of an electromagnetic shower is measured in η and ϕ direction by two independent wire proportional counters with pad readout. [37]

3.2.3 Trigger Detectors

Most detectors of STAR are too slow to be used in trigger applications: The bunch crossing rate is almost 10 MHz, which means that the trigger detectors have to be read every 107 ns. Only few detectors in STAR were designed to meet this requirement, making them available for trigger algorithms.

The Zero-Degree-Calorimeters (ZDC) measure the energy deposited by spectator neutrons from nucleus-nucleus collisions. These neutrons leave the interaction region along the beam pipe and pass the magnets controlling the ion beams without deflection. The ZDCs are located on both sides of STAR behind these magnets, collecting spectator neutrons from both of the colliding nuclei. The ZDCs can be used as a minimum bias trigger, but it is also possible to use the energy deposition, which relates to the number of spectator neutrons, for the definition of a centrality trigger. Timing information about the arrival of the neutrons in both detectors allow the reconstruction of the primary vertex of a collision on the trigger level.

The Central Trigger Barrel (CTB) is an array of 240 scintillator slats surrounding the TPC. The signal of each slat is approximately proportional to the number of charged particles that traversed it; the signal sum is thus a direct measure for the charged particle multiplicity of an event within $|\eta| < 1$.

For the centrality trigger used during the first RHIC runs, a combination cut on the CTB sum and the energy deposition in the ZDCs was used to select the most 7% most central events.

Most trigger detectors are used to measure global event properties, like the particle multiplicity, the event vertex or just the occurrence of a minimum-bias collision. This allows for unspecialized datasets that are suitable for almost all analyses, but are rather inefficient in the search for rare signals: if a rare event can be identified on the trigger level, only a small subset of all events must be saved, dramatically reducing storage and offline processing requirements.

For some signatures, this identification on the trigger level can be provided by the BEMC and EEMC. Timing constraints of the trigger system admit only the use of tower data, but not the data from the SMD. To fit into the level-0 timing constraints, the data is packed, so that for a level-0 decision, only information about the highest tower and energy deposition in a jet-patch is provided, i.e. an area of about 1×1 units in pseudo-rapidity in azimuth. To reduce the complexity of the electronics, the ADC values are converted from 12 bits to 6 bits before they are sent to the trigger system. For the conversion, the original 12-bit values are right-shifted by 5 bits, and the two highest bits of the original ADC value are combined into a single overflow flag, that is stored in the highest, sixth bit of the trigger ADC. Pedestal subtraction is applied, mainly to allow the calculation of energy sums for jet triggers. The resolution of the trigger ADC is $2^5 = 32$ times the resolution of the original ADC, or about 250 MeV per trigger ADC.

The most important trigger using EMC data is a high-tower trigger that fires if at least one tower in the event is above a preset ADC threshold, selecting towers with energy deposition above a E_T threshold. In p+p collisions, a jet-patch trigger is also used to select events with an energy deposition in one jet-patch above threshold, that are an indication for a high-energy jet.

3.2.4 Trigger

STAR uses a complex trigger system with 4 levels. A detailed description can be found in [38], while this section summarizes its general features and capabilities used for this thesis. The levels are numbered from 0 to 3 and ordered by their timing constraints and analysis capabilities. The Level-3 trigger will be explained in a separate section, because its design as an online reconstruction farm differs from the other trigger levels that only have a small part of the event data available for their decision.

Level-0 samples data from the fast detectors for every bunch crossing, and accepts events if the data from the detectors fulfill certain trigger conditions. The level-0 trigger uses coarse information from the trigger detectors to select events based on global event characteristics or very clear signals. Typical algorithms include minimum bias triggers that select an event sample that represents natural distributions of events, centrality triggers that enhance the sample of collisions with small impact parameters or high-tower triggers that look for hits in the EMC with high energy deposition. High-tower triggers allow to select events with hard processes like high-energy jets or J/Ψ and Υ production.

To allow level-0 to issue a trigger decision for every bunch crossing, i.e. every 107 ns, a complex system is required. Therefore, level-0 has been designed as a tree of Data Storage and Manipulation (DSM) boards. The tree consists of four layers of DSM boards, and each layer feeds the output of its DSM boards into the inputs of the DSM boards of the next layer. The number of DSM boards decreases with each layer, down to only one board in the last layer, the so called last DSM board. Each of these DSM boards has 128 input bits, grouped into 8×16 bits, and 32 output bits. These boards contain a ring buffer and an FPGA. The ring buffer stores the data for 64k bunch crossings so that it is available after the event has been accepted and the data is requested by DAQ to be included into the data stream. The FPGA[6] is an integrated circuit that can be programmed with logical functions to perform a wide range of manipulations of the data, e.g. summing of ADC values, or finding maximum values. The output of the FPGA is then used as an input to the next layer of DSM boards, or — in the case of the last DSM board — into the Trigger Control Unit (TCU). The TCU uses the output of the last DSM and the live bits representing the status of the detector subsystems to make a decision for each bunch crossing and issue a trigger to the rest of the system if the event is to be recorded.

Level-1 is currently not used for event selection. It is however a working part of the current system and is responsible for the bookkeeping of events in the trigger subsystem.

In the original design described in [38], level-2 was a VME CPU connected only to the trigger network. In 2002 it was replaced by an AMD Athlon CPU running Linux, that also has a connection to the myrinet network used by DAQ and Level-3. This connection is used to ship the full BEMC tower data to Level-2, improving its capabilities significantly. Instead of a resolution in $\Delta\eta \times \Delta\phi$ of 0.2×0.2, the full tower resolution of 0.05×0.05 can be used. This facilitated complex algorithms like the reconstruction of the invariant mass of electron pairs to trigger on J/Ψ and Υ candidates.

3.2.5 Data Acquisition

The data acquisition (DAQ) is responsible for the collection of the data from all detectors, the assembly of a single data block containing all detector contributions, the writing of these blocks to a file on disk, and the transfer of these files to the long term storage system HPSS[7] [39].

Detector Brokers and Receiver Boards Data from slow detectors, i.e. detectors that are not part of the trigger system and are read out for every event crossing, is sent to the DAQ system over optical links that end in the Receiver Boards. In the case of TPC, FTPCs and SVT, each of these Receiver Boards features three Intel i960 CPUs that perform 10-to-8 bit conversion, zero suppression, cluster finding and data formatting. The cluster-finder was intended for the Level-3 Trigger, but is also used as part of the DAQ100 concept to increase the event rate of STAR, as explained in chapter 4.3.

[6] Field Programmable Gate Array
[7] High Performance Storage System

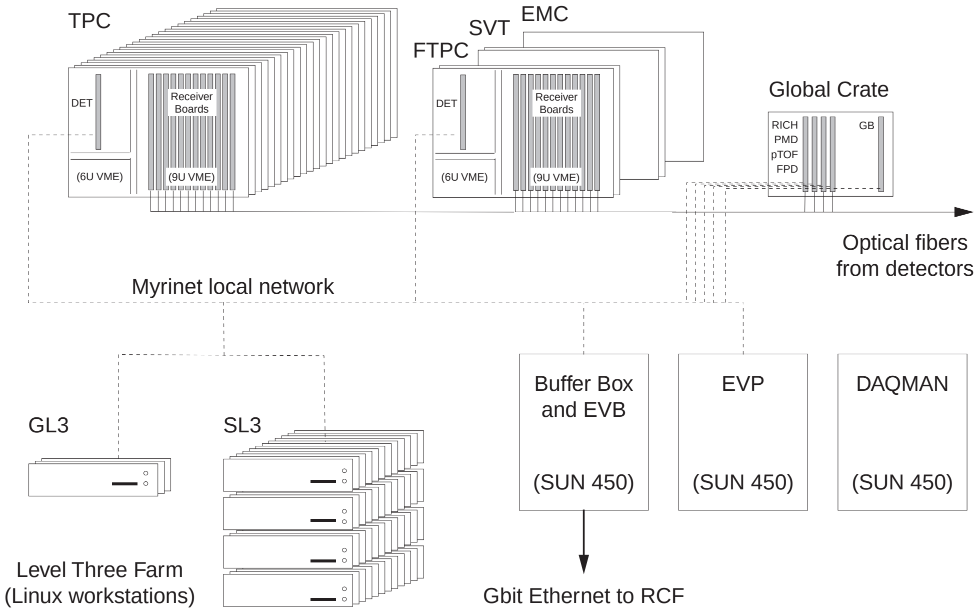

Figure 3.9: Schematic layout of the DAQ network [39]

The Receiver Boards for the EMC are much simpler and do not contain i960 CPUs for extensive online processing. Some smaller detectors like the PMD or FPD send the data over a 100 Mbit/s Ethernet connection.

For each detector, there are one or more Detector Brokers (DET) that control several Receiver Boards. These DETs provide a detector independent interface to the DAQ network. In the case of the TPC, there are 12 DETs, each handling data from 2 physical sectors.

Event Builder The Event Builder (EVB) collects data from all detectors, and assembles the data for one event in a structure suitable for storage in a file and offline processing. The events are then saved to local disk, with each file containing several hundred events. These files are then transferred to the RHIC Computing Facility and saved in HPSS.

The original Sun 450 system used as EVB, still visible in figure 3.9 has been replaced by four Linux systems. By using four EVBs working in parallel, the maximum data rate could be enhanced, the total storage for local event buffering could be increased to 8 TB (2 TB per EVB), and the redundancy ensures high availability.

Global Broker The Global Broker (GB) is the central control instance for the DAQ system: it receives notification about new events from the trigger system, and then controls the data transfer between the DETs, the L3 CPUs and the EVB.

Network connections The components of the DAQ system are connected using Myrinet [40, 41]. Myrinet is a high-performance, low-latency interconnect designed for cluster computing with a maximum transfer rate of 1.28 Gbit/s in full duplex mode. This network is used for control messages and data transfers. Data transfers can be handled with minimal CPU load due to the directed send capability of Myrinet, which allows data to be transferred directly into the receiving node's memory using a DMA engine in the network card.

Access to HPSS is provided over a standard gigabit Ethernet connection. However, due to limitations of the recording hardware in HPSS, not the full bandwidth of the gigabit Ethernet connection is available, but only about 50 MB/s.

The data flow through the DAQ system is described by the proprietary Inter-Crate Communication Protocol ICCP [42].

3.3 Level-3 Trigger

The STAR detectors are designed to be read out at an event rate of $100\,\mathrm{s}^{-1}$, which corresponds to a data rate of several 100 MB/s for zero-suppressed AuAu events. As the original STAR design aimed at a data rate of only 20 MB/s to tape, a further reduction of the data rate was necessary. To achieve this reduction, an online event filter, the Level-3 Trigger was designed.

The Level-3 Trigger (L3) is not part of the Trigger system, but connects to the DAQ system to analyze the events after all detectors have been read out, but before the event is built by the EVB and saved to disk. It performs online reconstruction of TPC data and can run algorithms on the reconstructed data to accept events for offline reconstruction or reject them.

As maintenance and further development of the Level-3 Trigger was a large part of the work conducted for this thesis, it will be described in more detail in the next chapter.

Chapter 4

The Level-3 Trigger

4.1 Concept

As explained in the previous chapter, the maximum raw data rate of the STAR detectors exceeds the data sinking capabilities of the storage system: STAR can theoretically run at 100 events per second with a raw, non-zero-suppressed event size of almost 100 MB, yielding a total rate of up to 10 GB/s. The original design of DAQ, storage system and offline computing allowed for a data rate of only 20-30 MB/s, which was enhanced to 80 MB/s during the first four runs. The largest fraction of the data is generated in the tracking devices: the TPC followed by the FTPC and SVT. For these detectors, zero-suppression is performed which reduces the event size by a factor of 10 for the events with the highest detector occupancies, or even more for events with lower occupancy. Although this is lossy compression, it is very well understood and only has minimal effects on data quality.

This still leaves a discrepancy of several 100 MB/s of DAQ input rate, and a data sinking rate of only up to 80 MB/s. For further rate reduction, two principal approaches are possible: compression or selection.

- **Data compression** Loss-less compression like Huffman-coding [44] or more recent algorithms like Lempel-Ziv [45] or Burrows-Wheeler [46] only achieve small reduction factors of usually less than 2 for binary data of high entropy like the zero-suppressed raw data. Combined with the high CPU requirements of these algorithms, this effectively excludes the feasibility within the STAR experiment.

  An even higher compression can be achieved by lossy compression. The most promising method is to include the first step in offline reconstruction — cluster-finding — into online processing. An online cluster-finder is already available in STAR for the Level-3 Trigger, which makes this feasible. However, a problem with the calibration of the detectors could render the online cluster-finding unreliable. As an extreme consequence, the full dataset of a run period could turn out to be unusable.

- **Event selection** A safer approach is to select only a subset of all events, but save

> the full, zero-suppressed data for reproduction. This is practically the concept used by trigger to reduce the beam crossing rate of 10 MHz to a readout rate of less than $100\,\mathrm{s}^{-1}$ for the slow detectors. As raw data is available for a every event, reprocessing is possible in the case of major problems, making the loss of large fractions of the data less likely. The reduction in the number of recorded events compared to an approach using compression can be balanced by a trigger that selects events with the desired signal.

The design of STAR includes a Level-3 Trigger to perform event selection before recording the data on tape. As the data rate had to be reduced by a factor of up to 50, the Level-3 Trigger had to use very selective algorithms, that need detailed data about the event. The chosen way to achieve these rejection factors was the use of the main tracking detector, the TPC, for the trigger decision. The amount of data processing involved in the reconstruction of clusters and tracks from the raw data requires a complex system of CPUs working in parallel: 432 Intel i960 CPUs reconstruct clusters, 48 Alpha CPUs are used for tracking, and 3 CPUs collect the information from the tracking nodes and run selection algorithms.

This system has been used for the first runs of STAR, and several analyses used the Level-3 Trigger to improve statistics for rare signals: specific energy loss in the TPC gas has been used to identify anti-nuclei [47], a sample of high-momentum particles traversing the RICH[1] detector was produced [48] and ultra-peripheral collisions were identified [49].

Closer studies of the cluster-finder used in the Level-3 Trigger and the experience from using it in trigger applications revealed that its quality was comparable to the performance of the cluster-finder used in offline production at that time. The availability of a reliable cluster-finder for online use enabled STAR to switch from event selection to online compression of the data by writing cluster data. This change increased the maximum event rate of STAR from $20\,\mathrm{s}^{-1}$ to $80\,\mathrm{s}^{-1}$, but the large number of events will push the offline infrastructure to its limits, introducing long delays until all data from a run would be available. As the Level-3 Trigger was no longer needed to reject events, it was used to tag events with very rare signals for prioritized offline processing, speeding up the analyses of these signals. The implications for the Level-3 Trigger will be discussed in section 4.3.

4.2 Implementation

This section summarizes the setup of Level-3 as it was used during the first two runs, as a baseline for the changes that were implemented in the course of this thesis. This system has been described in Clemens Adler's thesis in great detail [50], and therefore the explanation in this section can be rather terse.

[1] Ring Imaging Cerenkov Detector, installed in STAR until 2001

4.2.1 Cluster Finding

The first step of processing for the Level-3 Trigger is already performed in the Receiver Boards (RBs) of the DAQ system: the integrated i960 CPUs reconstruct the charge clusters in the pad-planes due to ionization by charged tracks. For each pad, the digitized signal is analyzed for a sequence of rising and falling ADC values. These sequences begin with the first time-bin of the pad, or the first bin after a local minimum in the ADC sequence, rise to a maximum, fall off again and end with the next local minimum. For each of these sequences with a ADC sum above a threshold, the total charge and the weighted mean in time direction is saved. By combining the sequences of neighboring pads to clusters, the centroid of the charge distribution and its position in pad-timebin coordinates can be determined.

By implementing the cluster-finder in the RBs, a high level of parallel processing can be achieved: the TPC has a total of 144 Receiver Boards with three i960 CPUs each, so the cluster-finding is performed by 432 CPUs in parallel. As cluster-finding is performed locally on each pad-row of the TPC, interprocess communication during the cluster-finding is not necessary. After the cluster finding has been finished, the cluster data from the 12 RBs of each DET, which corresponds to two physical TPC sectors, is shipped to one Sector-Level-3 CPU.

The cluster-finder was originally implemented in C++ with certain parts in i960 assembler language for optimal speed. A modified version of the cluster-finder replaces the assembler parts with C++ code, so that the it can be run on other platforms as well, making it accessible for offline testing and evaluation.

4.2.2 Sector-Level-3: Tracking

In the next step of event reconstruction, these clusters have to be connected to tracks that represent particle trajectories. As the magnetic field in the TPC is nearly homogeneous, a helical track model is used for the reconstruction. Track reconstruction proceeds from the outermost to the innermost pad-rows of the TPC. It starts by finding track seeds, that are constructed by starting from one cluster and finding the closest neighboring cluster in the next pad-plane. This step is repeated, and the closest neighbor of the newly added cluster is located, until the seed contains a configurable number of clusters. Then, the track model of a helix is fit to the track seed, and this helix can then be extrapolated to the next pad-plane to find the next point on the track. This procedure of fitting, extrapolation and search for a matching cluster is repeated until either no cluster could be associated for several pad-rows or the innermost pad-row of the TPC has been reached. This type of algorithm is called a follow-your-nose tracker [51, 50].

The Level-3 track-finder employs two strategies for maximum speed of the algorithm: *conformal mapping* and *data organization in sub-volumes.*

The helix track model is not ideal for fast computation: as the projection in the x-y-plane gives a circle, fitting and extrapolation is relatively slow. Level-3 uses conformal mapping to transform these circles into straight lines. This transformation requires one point (x_t, y_t)

known to be on the helix and is computed:

$$x' = \frac{x - x_t}{(x - x_t)^2 + (y - y_t)^2}, y' = \frac{y - y_t}{(x - x_t)^2 + (y - y_t)^2} \tag{4.1}$$

Applying this transformation simplifies the problem from handling circles in the real x-y-plane to fitting and extrapolating straight lines in conformal space.

The other method used to speed up the algorithm is efficient data organization: instead of having one large container for all clusters, the volume of the TPC is divided in smaller sub-volumes. Locating a cluster close to another cluster or an extrapolation point does not require to loop over all clusters, but only a small fraction located in few of these sub-volumes.

Track finding is performed by a cluster of 48 Compaq Alpha systems running Linux. As these computers process the data of one logical TPC sector, equivalent to two physical sectors, they are called Sector-Level-3 computers, or SL3. 12 of these SL3s work in parallel on the reconstruction of one event. The data from these 12 SL3s then gets shipped to a Global-Level-3 computer.

4.2.3 Global-Level-3: Trigger Decision

The final step in Level-3 processing is the assembly of all data, and the decision if an event is to be saved or rejected. All data is sent to one of three Global-Level-3 computers (GL3) by the SL3s handling this event. The GL3 then copies the track information into a global data structure, optionally tries to merge tracks from different sectors and fills trigger information into the global data structure. To get a decision for the event, user-provided algorithms are run on the data, that can use TPC, BEMC and trigger data for their analyses. After the algorithms are finished and returned their decisions, the GL3 reports this decision to the Global Broker, that will either start the data transfer from the DETs to the EVB or abort the event, depending on the L3 decision.

The GL3s are also responsible for the book-keeping of processed events. It keeps counters how many events were processed, accepted and rejected for each algorithm. The counters are written into the Level-3 contribution to the DAQ stream, and since 2004 also to a separate database.

4.2.4 Event Display

A fraction of the events processed by Level-3 are saved to a local disk and can be displayed on a live event display. The event display shows a wire framework of the TPC, the SVT and the FTPCs, and the clusters and tracks reconstructed by Level-3. It has recently been updated to display data of the Barrel- and Endcap-EMC (see section 4.4).

It is not only very useful in monitoring the quality of the taken data, but has also gained a certain fame by producing the first images of RHIC collisions that appeared on the front page of magazines like the *CERN Courier* and *Physical Review Letters*.

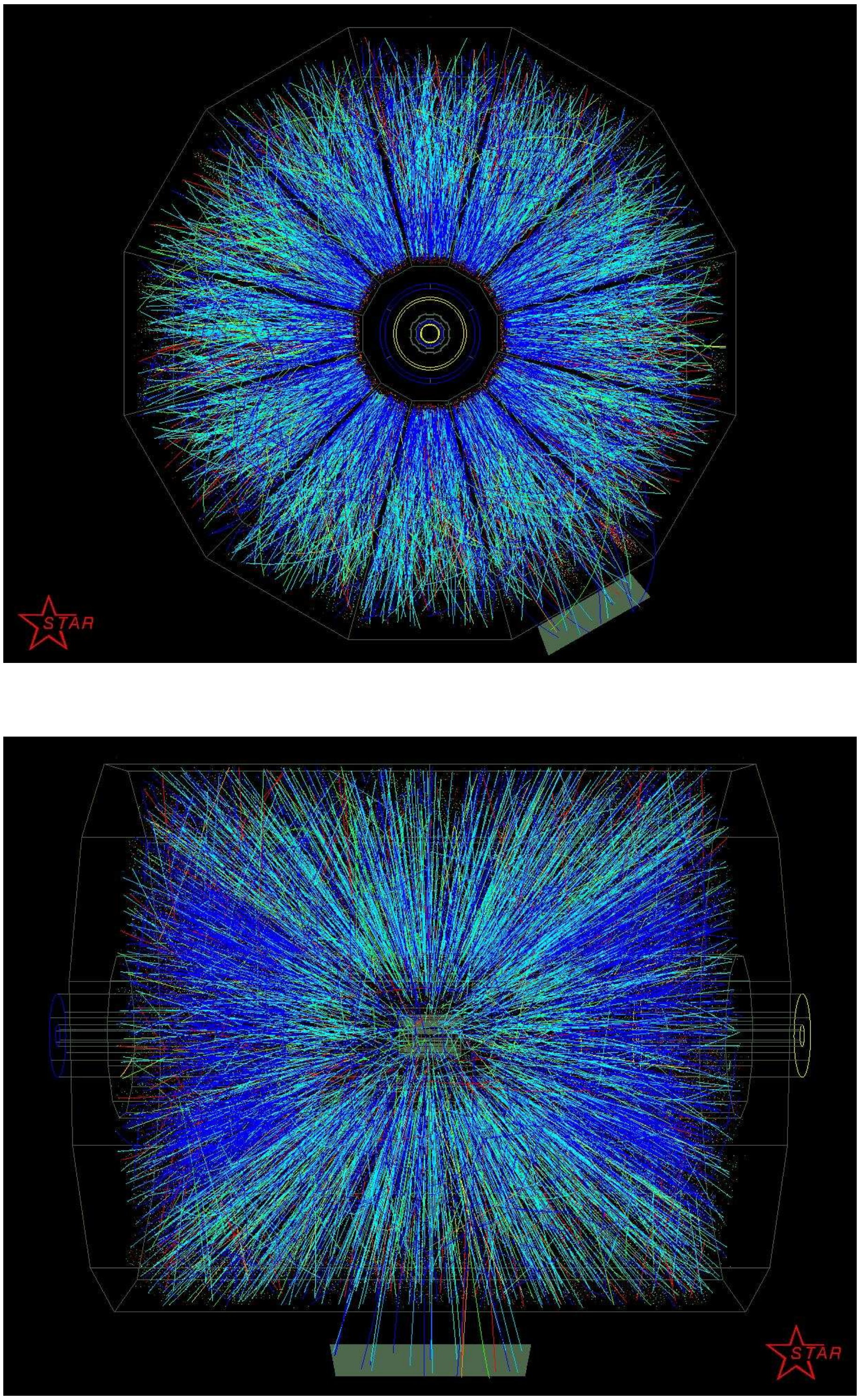

Figure 4.1: Front- and side-view of a Au+Au collision at $\sqrt{s_{NN}} = 200\,\mathrm{GeV}$. The tracks are colored according to their energy loss in the gas of the TPC.

4.2.5 Network and Data Flow

The Level-3 Trigger is integrated into the DAQ Myrinet network, enabling fast transfers between DETs and SL3s. All data transfers and messaging related to the data flow between DAQ and Level-3 use this Myrinet network. An Ethernet network is used for NFS, remote access to the nodes, and connections to the RunControl application.

The typical data flow through the Level-3 system starts at the Global Broker that receives the information about new events from the trigger system. GB determines which detectors provide data for Level-3 and assigns the SL3s and a GL3 that will process the data. The assignment of SL3s to DETs takes the network topology into consideration and only uses SL3/DET pairs that are connected over no more than two switches to reduce the risk of lockups of the network. Load-balancing is achieved by using a round-robin scheme. The GB sends an announcement message to the selected GL3 containing a list of detectors to be used by Level-3 and the assigned SL3 nodes.

After receiving the message, GL3 allocates a buffer for the event and announces it to all SL3 nodes. The SL3 nodes then request the data from their assigned DETs. After each SL3 received the data from the DET, it checks for the detector type, and starts processing as necessary: in the case of TPC data, the track-finder is invoked. The reconstructed track data is then sent to the GL3. As soon as the GL3 received data from all contributing SL3s, it starts to merge the data and run the analysis algorithms to determine the Level-3 decision. The decision is sent to the GB, that initiates the data transfers from all subsystems to the EVB, from where the data is finally transferred to HPSS.

4.3 DAQ100 and Express Streams

In October 2001, Jeff Landgraf and Tonko Ljubicic proposed an upgrade to the DAQ system that would allow to write cluster data for all events taken by STAR [52]. This upgrade included minor technical upgrades and changes in the DAQ data flow as well as the proposal to drop zero-suppressed raw data in favor of cluster data. A detailed comparison between the old offline and Level-3 cluster finder revealed that the performance of both was comparable, and a decision was made to switch to the Level-3 cluster-finder, which was subsequently called "DAQ100 cluster-finder". As a result, STAR was capable of recording all events taken by the slow detectors and the requirements for online event selection with the Level-3 Trigger changed entirely.

Although the data taking capabilities had been improved, there was no substantial upgrade to the offline reconstruction and analysis farms. It was predicted that a full-energy Au+Au run with all DAQ100 modifications would produce about ten times more events than the same run with the old scheme, and that a long run could yield up to 100 million events. Despite some savings due to the removal of the cluster-finder from the offline production software, this amount of data would take 1-2 years for a single reconstruction pass, not including any test or calibration production. This additional delay of at least one year and the availability of the Level-3 online analysis farm led to the idea of *express streams*: instead of using Level-3 as a trigger, it would be used to flag very few events for preferred offline processing. These events are then copied to a second set of data files containing only a very small fraction of all events, the *express stream*.

The advantage of this combination of DAQ100 and express streams is that it is possible to have the maximum statistics for analyses that cannot use the Level-3 Trigger to select a subset for their analyses, and it still allows analyses that can provide a selective Level-3 algorithm to get access to the full dataset in a timely fashion. An additional benefit is the possibility to reprocess the express stream if an error was found in a production, something that will not be possible with the main data stream.

A flagged event is copied to a second data stream, i.e. the same event is written twice. This small overhead simplifies the consistent analysis of non-express-stream data, because each file of the main data stream forms a representative sample of events. If only one copy of the event would be written, all files of a run would be required to form a representative sample with express-stream- and unflagged events. If any file from a run would be lost, a readjustment of the ratio between flagged and unflagged events would be necessary for virtually all analyses, a complication that can be avoided by writing flagged events twice.

Of course, the express stream has to remain small in comparison to the full dataset, a requirement that becomes even stronger due to the overhead introduced by saving two copies of flagged events. To minimize the impact on the usable data rate to HPSS and offline production, a goal was set to write only 1% of all data into the express stream.

4.4 EMC Integration

One of the main applications for the Level-3 Trigger are quarkonia, heavy quark-antiquark-systems like J/Ψ or Υ that decay into e^+e^--pairs. To distinguish the decay products from the large hadronic background, good electron identification is necessary. In STAR, this particle identification is provided by the electromagnetic calorimeters. To enhance the electron identification of the Level-3 system, the Barrel- and Endcap-EMCs have been integrated into the GL3 framework. The integration of the EMCs can also be used for the measurement of energetic photons and neutral pions, that decay into photons.

The tower data from the Barrel-EMC has been available to Level-3 since the d+Au run of 2003. During the Au+Au run in 2004, Endcap-EMC tower data was integrated as well. The data is accessible from within the GL3 analysis framework and also in the event display. During the d+Au run, the BEMC was used in the development and testing of J/Ψ algorithms for the Level-2 and Level-3 Triggers. In the Au+Au run of the following year, it has been used to select Υ candidates and events with very high towers and high-p_T-tracks for the express stream.

As for the TPC, a SL3 is assigned for BEMC and EEMC tower data by the GB. When the EMC tower data is received by the SL3, it forwards the data to the GL3 without any processing. The EMC data bank is copied into the Level-3 event structure in the same format that is used in DAQ raw data files.

Technically, access to EMC tower data from within the GL3 framework is provided by a class called `gl3EMC`, that reads the EMC data and stores it in an array of instances of `gl3EmcTower`. During the reading of the tower data, the ADCs are converted to energy using the class `l3EmcCalibration` that holds a local copy of the offline calibration tables for the EMCs. Access to the EMC tower data is organized by tower ID, although access via η and ϕ coordinates could be implemented if required. For each tower, energy, ADC, η and ϕ can be retrieved.

4.5 Level-3 Applications during the 2004 Au+Au Run

During the 200 GeV Au+Au run from January to March 2004, Level-3 has been used for several applications: attempt of a first measurement of the decay $\Upsilon \rightarrow e^+e^-$ in heavy ion collisions; high-p_T correlations between neutral particles measured with the BEMC and charged tracks from the TPC; the search for strangelets in the ZDCs and the search for heavy anti-nuclei.

4.5.1 Upsilon

The modification of quarkonium states has been suggested as a signature of the quark-gluon-plasma. In the SPS program the suppression of the J/Ψ was measured by the NA-50 collaboration, but the production cross section of the Υ was too small for a measurement. Calculations for RHIC energies predict that a measurement might be possible.

The two decay modes that are easiest to identify are $\Upsilon \rightarrow e^+e^-$ and $\Upsilon \rightarrow \mu^+\mu^-$. As STAR does not have myon identification capabilities, the only channel accessible in STAR is the electronic decay mode. The electron momenta in the rest frame of the decay are back-to-back and correspond to half of the mass of the Υ:

$$|p_e| = \frac{1}{2} m_\Upsilon c = 4.730\,\mathrm{GeV}/c \tag{4.2}$$

Because the Υ does generally not decay in rest, the momenta of the electrons in the laboratory frame will be boosted, leading to a broad distribution of electron momenta and opening angles in the laboratory frame.

As the production rate of the Υ is very low, an efficient trigger is essential to minimize losses and extract a signal. For this application, three of STAR's four trigger levels were used:

- **Level-0:** A preselection on Level-0 used a high-tower trigger with a threshold of 13 trigger-ADC counts, corresponding to a threshold of $E_\perp \approx 3\,\mathrm{GeV}$. As this cut was applied to the highest tower of the event, not the highest-energy cluster in the event, energy sharing between towers had to be taken into account by a lower trigger threshold.

  The resulting event rate of about $20\,\mathrm{s}^{-1}$ was well within the capabilities of the Level-2 Trigger.

- **Level-2:** With full BEMC tower information available, Level-2 performed a reconstruction of electron candidate pairs, and used these to estimate the invariant mass of a possible parent particle. The energy of an electron shower is often distributed over more than one tower, and therefore the consideration of neighboring towers improves the energy resolution of the electron candidates. After applying energy cuts on the decay daughters to reduce the background and the time necessary for processing all cluster pair combinations in an event, the invariant mass of the particle can be estimated by assuming a decay vertex at the center of the collision region and straight electron trajectories to the cluster positions. The trigger algorithm cuts on the opening angle and the invariant mass of the parent.

- **Level-3:** On the last trigger level, the information from the EMC and the TPC can be combined to reject photons or neutral pions, and to improve the invariant mass resolution. As most calorimeter hits with high energy originate from $\pi^0 \to 2\gamma$ decays, the requirement of a high-momentum track pointing to each of the clusters can significantly reduce the background. An improvement of the invariant mass reconstruction is also possible, because the momentum resolution of the TPC is better than the energy resolution of the EMC in the applicable region, and because the better vertex resolution improves the determination of the opening angle. However, as the track requirement provided a sufficient reduction of the event rate, no cut was made on the invariant mass.

A more detailed description and an analysis of the express stream data can be found in Thorsten Kollegger's thesis [53].

4.5.2 Strangelets

Strangelets, a form of matter containing roughly equal amounts of up-, down- and strange-quarks are predicted by some theories to be meta-stable, or even absolutely stable. These strangelets might be produced in the dense and hot conditions of relativistic heavy-ion collisions, like in the Au+Au collisions at RHIC, and some speculations even predicted the destruction of the earth by a strangelet [54].

Zhangbu Xu and Aihong Tang suggested to measure strangelets in STAR with the ZDC detectors. A signature would be an abnormally high energy deposition in one of the calorimeters. As the production rate is expected to be higher in central collisions, the requirement would be combined centrality cut using the CTB.

This trigger used a combination of Level-0 and Level-3: On Level-0 a cut on high CTB multiplicity selects central events, and a cut above some ZDC threshold triggers on high energy deposition in at least one ZDC. On Level-3 the cut is refined with a polynomial parameterization of the ZDC-CTB-correlation, that is used as a better reference for anomalously high energy deposition in a ZDC.

This analysis have been presented to the public at the QuarkMatter 2004 conference [55], and a paper with the final results is in preparation.

4.5.3 Anti-Nuclei

In collision of relativistic heavy-ion collision, the abundance of anti-nucleons allows the formation of light anti-nuclei. As these anti-nuclei cannot be fragments of the incoming nuclei, they must be produced in the hadronization of the fireball. The production of these anti-nuclei is sensitive to the conditions at the freeze-out of nuclear matter, and therefore allows to draw conclusions about the parameters governing the hadronization process.

Already in the first full-energy Au+Au run, a Level-3 trigger for heavy anti-nuclei has been used to measure $\overline{^{3}\mathrm{He}}$. Although 221 $\overline{^{3}\mathrm{He}}$ ions were found, no $\overline{^{4}\mathrm{He}}$ nuclei could be identified due to a lack of statistics [47, 56].

The next long, full-energy Au+Au run in early 2004 promised to provide higher statistics and facilitate a measurement of $\overline{^{4}\mathrm{He}}$. As a base trigger on Level-0, a high-tower trigger with a threshold of about 3 GeV was used, which concentrated the search on anti-nuclei that annihilated in the EMC. The analysis is currently worked on by Sören Lange.

4.5.4 High-p_T Trigger

As high-p_T physics evolved into one of the main fields of interest of STAR and the other RHIC experiments, and high-p_T probes are rarely created in heavy-ion collisions, a means to trigger on these probes was sought.

On the lower trigger levels, only the BEMC can provide energy information and thus a trigger for probes with high transverse momentum. But as the BEMC is only sensitive to photons, electrons, and neutral pions via their photonic decay channel, no trigger for charged hadrons is available before Level-3. Level-3 performs full event reconstruction, including tracking of the TPC, and can therefore provide a trigger for these particles.

The first trigger for high-p_T physics was implemented on Level-3 for the first full-energy Au+Au run in 2001, when charged high-p_T tracks pointing to the Ring-Imaging Cerenkov Detector [57] were selected for later identification after full offline reconstruction [48].

For the Au+Au run in 2004, a new algorithm was implemented, that used not only data from the TPC, but also the BEMC to find particles with large transverse momentum. The algorithm selects an event, if a tower with high energy deposition and a charged high-p_T track are found in the same event, or if a tower with very high energy deposition was found, the requirement of a charged track was dropped. In that case, the algorithm worked like a normal high-tower trigger. The dataset taken with this trigger forms the basis for the analysis presented in this thesis.

Chapter 5

Analysis

Correlations of charged particles from dijets provide a wealth of information about the modification of jets in the presence of the hot medium created in heavy ion collision. But in dijets not only the jet opposite to the trigger particle is affected by the medium, but also the jet containing the trigger particle. The resulting bias can be avoided by studying correlations with a trigger particle that can escape the medium without interactions: prompt photons.

This chapter will present the technical aspects of an analysis of correlations using photon candidates as trigger particles and charged associated particles. An interpretation of the results will be given in chapter 6.

The first section will give an overview of the dataset used in this analysis, including a review of the integrated luminosity sampled for this analysis, a description of used trigger algorithms and a list of problems encountered with the recorded data. A baseline for comparisons and the study of detector effects will be established in section 5.2, that summarizes PYTHIA and GEANT simulations made for this thesis.

Trigger and associated particles and azimuthal correlations are discussed in the last three sections of the chapter: section 5.3 describes the definition of trigger clusters, the rejection of charged particles and the energy resolution of the clusters. The selection of associated particles is briefly explained in section 5.4, and section 5.5 describes the analysis of correlations between trigger and associated particles, discussing background, near- and away-side yield, and the extraction of the correlation strength of azimuthal correlations.

5.1 Dataset

The dataset used for this analysis has been taken during the long Au+Au run at RHIC top energy of $\sqrt{s_{NN}} = 200\,\mathrm{GeV}$ between January and March 2004. The use of a Level-0 trigger increased the statistics available for this analysis beyond the number of recorded events. The key figure is therefore no longer the number of events on tape, but the number of events that were offered to the trigger system while the detectors were ready to be read out (*live*). This number is directly proportional to the integrated luminosity, where the

	bemc-ht-13 offered	bemc-ht-13 triggered	highpt-L3 triggered	mb-zdc-narrow × prescale	integrated luminosity	lifetime
All runs	19.65 M	5.88 M				29.9%
Good runs	14.36 M	5.14 M		347 M	$48\,\mu b^{-1}$	35.8%
Express stream	8.70 M	3.50 M	31003	287 M	$40\,\mu b^{-1}$	40.2%
Old parameters	3.50 M	1.53 M	13588	110 M	$15\,\mu b^{-1}$	43.8%
Final parameters	5.19 M	1.96 M	17415	177 M	$25\,\mu b^{-1}$	37.8%

Table 5.1: Event numbers and sampled luminosity of the bemc-ht-13 and highpt-L3 triggers. 83% of the usable luminosity sampled by the high-tower trigger was also available to the highpt-L3 trigger and written to the express stream. With the final parameters, the algorithm sampled more than half of the integrated luminosity.

proportionality factor is the Au+Au cross section.

RHIC reports an integrated luminosity delivered to STAR during this run of $1270\,\mu b^{-1}$. Downtimes of STAR, limited livetime, availability of the high-tower trigger and stricter event selection cuts reduce this number considerably.

Downtimes of STAR are mainly caused by two reasons: for each new fill of RHIC, the detectors are put into a stand-by mode with reduced voltages to protect them from damages that could be caused by high radiation levels in the case of a beam loss. After the beam has been stabilized at the beginning of a new store, the detectors are brought up to operational settings again. This procedure takes some time during the highest luminosity phase of the store, which remains unused. The other reason for downtimes of STAR are technical defects, preventing some or all of the subsystems to take data. The amount of missed integrated luminosity due to these STAR downtimes is unknown.

The slow detectors of STAR can only process a single event at a time, therefore, after receiving a trigger, they cannot accept another trigger until they are finished processing the previous one, they are said to be *dead*. For rare triggers, the dead-time should be as low as possible to maximize the probability of being ready to take the event when it is offered. This however requires a low event rate, which is in conflict with the goal to take a large amount of bulk data with minimum bias and central triggers at high rate. As a compromise, STAR takes data at a dead-time of about 60%, reducing the sampled integrated luminosity by more than a factor of two.

Another difference between the luminosity numbers of STAR and RHIC is the definition of an event. While RHIC counts the coincidence of signals in both ZDCs as a collision, STAR also requires a ZDC-based vertex cut and signals in the CTB to reject various background processes.

As the Barrel EMC was used as a trigger detector for this analysis, data-taking was only possible after the EMC had been calibrated. The calibration took about one month, which made the first month of the run unavailable to this analysis. There was also a problem with the level-3 trigger system which was unavailable for about the same time.

Level-0	
ZDCE && ZDCW	Signals in both ZDCs
ΣCTB > 75	Veto of ultra-peripheral events
$\lvert$ZDC vertex$\rvert < 30\,\mathrm{cm}$	Time difference between ZDC hits
Trigger ADC(high-tower)> 13	High-tower cut on trigger ADC
Level-3	
ADC(high-tower)> 992	High-tower cut on raw ADC
$\Sigma E_T(EMC) < 2\,000\,\mathrm{GeV}$	Removal of corrupted events

Table 5.2: Cuts applied on level-0 and level-3 triggers. The ZDCE, ZDCW, CTB and ZDC vertex cuts are identical to the minimum bias trigger. The high-tower cut on level-0 is a strict subset of the level-3 cut.

The integrated luminosities sampled by the *highpt-L3* trigger algorithm, that was used for this analysis and is described in section 5.1.1, as well as the standard high-tower trigger *bemc-ht-13* are listed in table 5.1. The integrated luminosity is measured with the *mb-zdc-narrow* minimum bias trigger, that required signals in both ZDCs within a time window that corresponds to a vertex cut of $|z_{vertex}| < 30\,\mathrm{cm}$ and and a non-zero signal from the CTB. For the conversion from minimum bias events to integrated luminosity, the number of minimum bias events was multiplied by the applied prescale and the sampled hadronic cross section, which was assumed to be 7.2 b.

The *highpt-L3* trigger sampled 83% of the luminosity available to the high-tower trigger, the difference is due to downtimes of the level-3 system caused by problems in the interplay with other detector subsystems. The *highpt-L3* trigger algorithm with the final parameters, that provided the dataset for this analysis, sampled $25\,\mu\mathrm{b}^{-1}$ or more than half of the integrated luminosity recorded by STAR with the *bemc-ht-13* trigger.

5.1.1 Trigger Algorithm

On level-0, the standard high-tower trigger for the 2005 Au+Au run, called *bemc-ht-13*, was used. The trigger algorithm required the conditions for the *mp-zdc-narrow* minimum bias trigger and at least one tower with more than 13 trigger ADC counts, which corresponds to an E_T threshold of about 3 GeV. For a description of trigger ADCs, refer to 3.2.3 or [38]. Due to a calibration error, the threshold was η-dependent and about 4 GeV near the end of TPC and BEMC.

Level-3 then refined the decision of level-0. The algorithm used for this analysis triggered if one of two conditions was met: either the event contained a tower above a very high threshold, or it contained a tower above a second, lower threshold and a high-p_T-track. The thresholds for tower energies and the p_T-cut were configurable parameters used to adjust the rate of this trigger to the assigned bandwidth. The analysis presented here only includes events that fulfill the condition of a single very high tower in the event. The requirement of a second track within the event has not been used, and therefore, only the

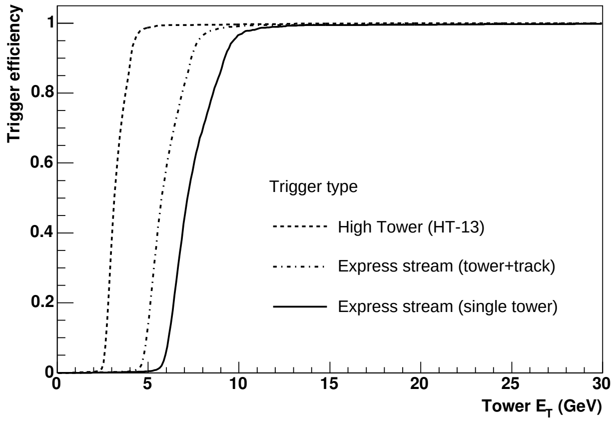

Figure 5.1: Efficiency of a high-tower trigger as a function of energy deposited in the tower. The efficiency reaches 90% around a threshold of 9 GeV.

single-tower condition of the algorithm will be explained.

As the quality of the BEMC calibration available early in the run was unknown, it was decided to base the level-3 decision on raw ADC values rather than the transverse energy that takes pedestals and gains of each tower into account. The algorithm accepted an event, if at least one tower had an ADC value that was greater or equal to the threshold.

The initial setting of the ADC threshold for a single tower was 1312 ADC counts. However, it turned out that this threshold resulted in a very low trigger rate that was well below the allotted bandwidth. To make use of this bandwidth, the threshold was lowered to 992 ADC counts on February 24, 2004. From then on until the end of the run on March 24 these final parameters were used. The previous, old parameter set has not been used for this analysis.

The onset of the trigger efficiency as a function of transverse energy deposited in a tower is shown in figure 5.1. Note that this is probability that a transverse energy deposition in a tower yields an ADC above threshold, and not the efficiency to trigger a particle with a given transverse energy. The shape differs from the ideal step function behavior and shows a slow transition from the insensitive low-energy region to the high-energy region with a trigger efficiency of close to 100%. The transition region extends from 6 to 9 GeV, corresponding to an increase in trigger efficiency from 5% to 90%. The reason for this slow rise is a mistake in the calibration of the BEMC, which was set to produce ADCs proportional to $E_T \cdot \sin\Theta$ instead of E_T. The result was a large fraction of events with triggers from the transition region, that are unusable for the analysis because of the biased pseudo-rapidity distribution of trigger towers.

Tests of the algorithm revealed a very high sensitivity to the problems described in section 5.1.2, and corrupted events accounted for a large fraction of all express stream data, because they were accepted by the algorithm with high probability. The measures taken to prevent these false triggers are described in that section as well.

5.1.2 EMC Problems

The faulty calibration of the BEMC hardware gains has already been mentioned. Although this problem lead to a large fraction of unusable events in the express stream, it did not have any further impact on this analysis. The threshold for the trigger particle simply had to be chosen high enough to avoid the transition region, otherwise the additional $\sin\Theta$ term would have introduced a bias on the pseudo-rapidity distribution of the trigger towers.

The most obvious problem with the BEMC is occasional data corruption. In a few percent of all events, the data bank containing the BEMC data is corrupted and does not contain useful data. This problem had been spotted using the level-3 event display and manifested itself in the form of large sections of the BEMC showing high values. In the ADC spectra, these corrupted events produce sharp peaks at every 256 ADC counts as seen in the top panel of figure 5.2, indicating a problem with the data transfer from the detector to the DAQ system. A check of the bank header of the BEMC contribution from each crate for valid data can detect this type of corruption. The middle panel of 5.2 shows that the removal of events with data corruption eliminates this problem.

At the time of data taking, this header check has not been available, therefore the simpler cut on the transverse energy sum was used, rejecting events with an unphysically high energy deposition. Although this cut did not remove all corrupted events, it reduced the false trigger rate to acceptable levels.

After removing events with BEMC data corruption, the raw ADC spectrum still shows a sharp peak at ADC values around 2070. This peak is caused by a single tower with a flaky highest bit. This tower was removed, both in the level-3 trigger algorithm and in the offline analysis. The removal leaves a clean ADC spectrum shown in the bottom panel of figure 5.2. The two sharp thresholds at 800 and 992 ADC counts from the tower-track and the single-tower conditions of the highpt-L3 algorithm are clearly visible. Although only express stream data has been used for this plot, a peak around ADC$\approx$500 is visible from the standard high-tower trigger. This is because for some time, when STAR ran without the level-3 trigger system, every high-tower trigger was written to the express stream.

The last problem, not visible in a simple ADC spectrum, are faulty towers. The first symptom, a flaky bit, has just been described, but the more frequent problems are dead and hot towers. A comprehensive description of possible tower problems can be found in [53], however this analysis is not sensitive to all of these problems. Dead regions of the BEMC, caused by single dead towers or defective crates, do not affect this analysis: as the goal of the measurement is not a cross section, but the yield of associated particles per trigger particle, it is not necessary to explicitly remove or even know the fraction of inactive BEMC regions: all inactive regions will not generate trigger particles, and will therefore be ignored implicitly.

While the absence of triggers from dead regions of the BEMC is not an issue for this analysis, fake triggers from hot towers are. The reasons for these hot towers can be manifold, from insufficient optical isolation over electronic problems to incorrect gain calibrations, but the result is the same: a tower generates trigger particles from either much less ener-

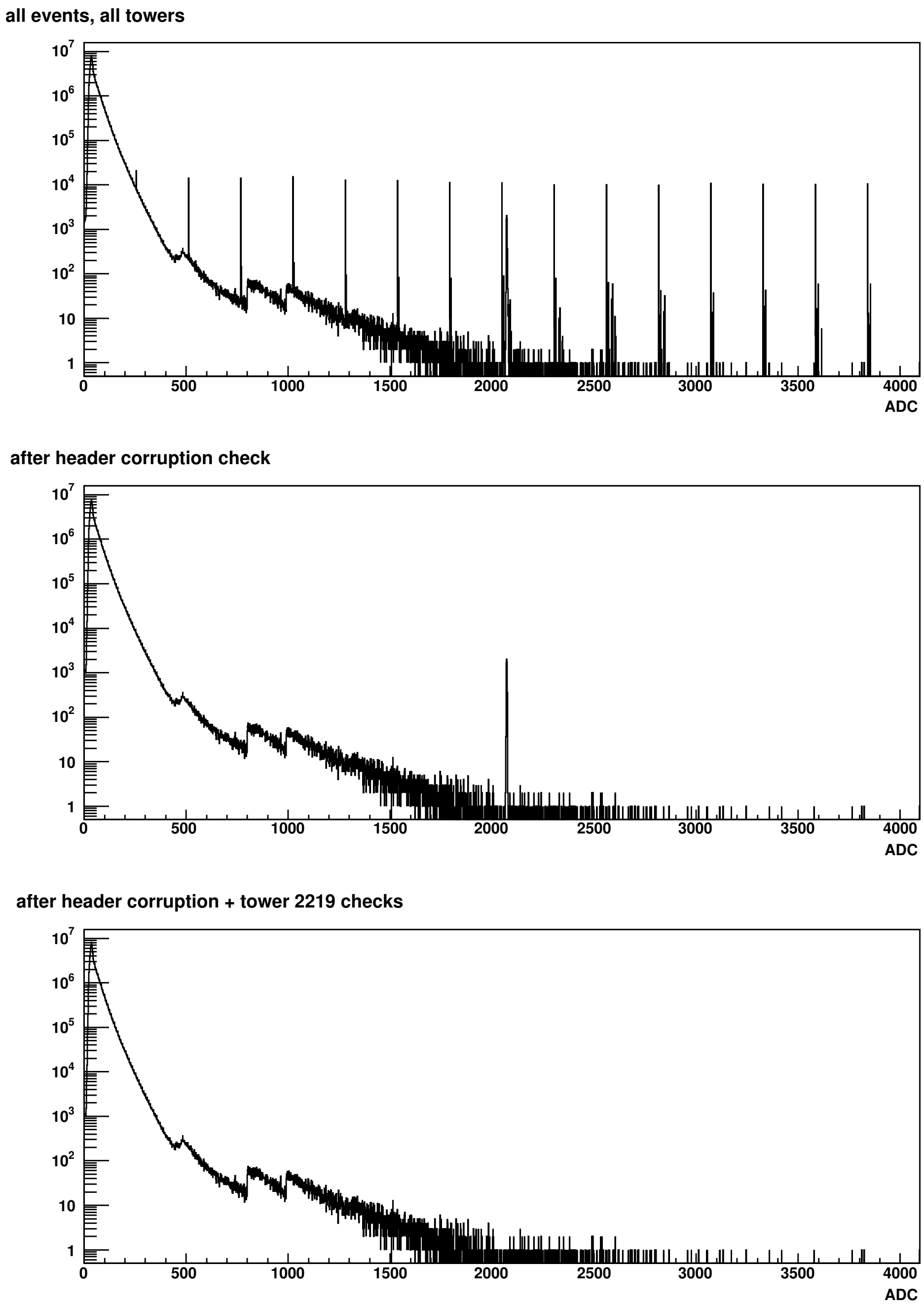

Figure 5.2: Cleanup of two different types of EMC corruption. The spikes at a distance of 256 ADC counts (top panel) are from events with a corrupted EMC data bank that can be removed with a check of the bank header. The peak at ADC≈2070 is due to a flaky bit of tower number 2219 (middle). After removing this tower, the spectrum is clean (bottom).

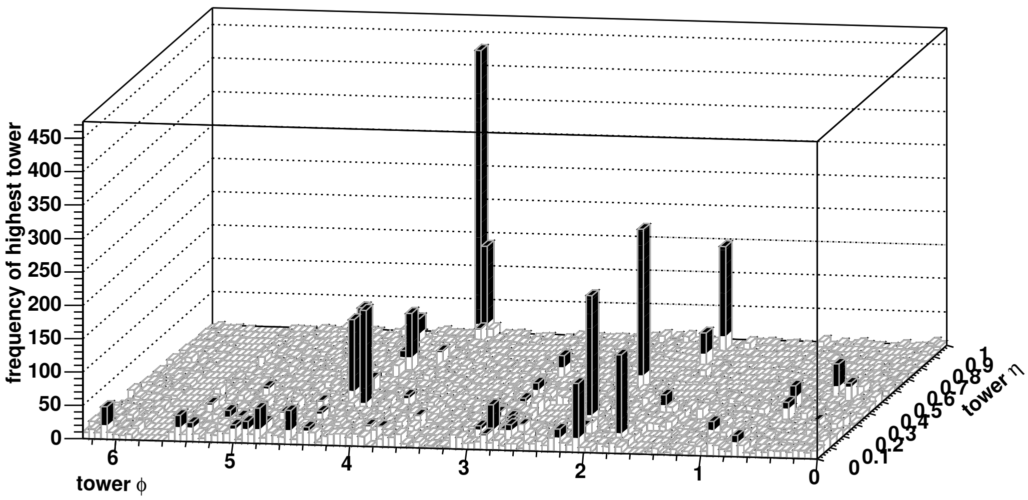

Figure 5.3: Location of highest tower in highpt-L3 triggered events. Towers that frequently show very high energy deposition are most likely faulty and must be removed. The black tops mark towers with more than 30 entries, indicating hot towers.

getic particles or pure noise. To avoid the contamination of the set of trigger particles with these fake triggers, the hot towers have to be determined and excluded from the analysis. The detection of hot towers used a phenomenological approach by counting how often each tower was the leading tower of the event, i.e. how often it contained the highest energy deposition. The determination used the highpt-L3 triggered data from the express stream. Figure 5.3 shows the distribution of leading towers in these events. While on average, each tower is found to be the leading tower in 6.8 events, some towers are the leading tower several hundred times. Towers with more than 30 entries were marked bad and ignored for this analysis. This threshold is illustrated in the figure by marking all entries above 30 in black. Therefore, all towers with a black top in the histogram have been marked bad. With this method, 32 towers were marked as hot, which corresponds to 1.3% of the 2400 towers of the available half of the BEMC.

5.2 Simulations

5.2.1 Pythia Reference

The dataset used for this analysis only contained Au+Au collisions. Although peripheral collisions can be used as a reference that minimizes the effects due to the presence hot nuclear matter, an external reference is desirable. In this case, p+p collisions simulated with the PYTHIA event generator take this role and approximate the particle production in real p+p collisions. This simulation does not only provide a reference for the Au+Au

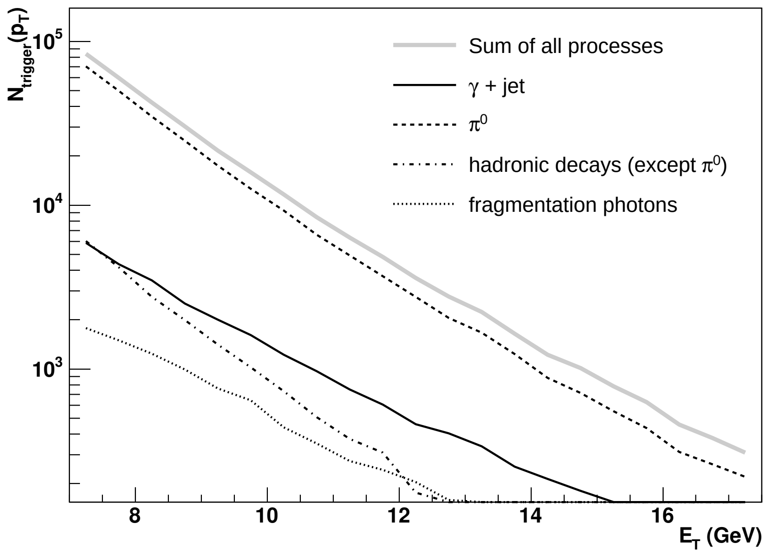

Figure 5.4: Spectra of trigger particles from a PYTHIA simulation. For description of processes see text. $N_{trigger}$ has not been normalized to the number of events.

data, but also allows to study the species-dependence of several analysis steps and cuts.

The PYTHIA event generator is a standard tool in particle and heavy-ion physics. It allows to simulate collisions between various particle species at a wide range of energies [58]. For this analysis, p+p collisions at $\sqrt{s_{NN}}$ =200 GeV were simulated, which featured either a QCD di-jet or a $\gamma +$ jet process. To reduce computing time, the minimum transverse momentum of the scattered particles was required to be greater than 5 GeV/c for $\gamma +$ jet events and greater than 8 GeV/c for di-jet events. In dijet events, a higher p_T limit can be used, because the momentum of the trigger particle is much lower than the momentum of the scattered parton because of fragmentation. Apart from the selection of processes and the kinematic cut, PYTHIA was run with its standard parameters. The output of the PYTHIA simulation was not processed with detector simulation and subsequent event reconstruction software, but analyzed directly.

Only particles within the acceptance of the STAR TPC and the full BEMC ($|\eta| < 1$) were used. Although only half of the BEMC was available in the data, the simulation used the full BEMC to improve statistics. Total yields can therefore not be compared, but azimuthal correlations are unaffected, because the acceptance for associated particles is symmetric for trigger particles in the two halves of the BEMC. The particles from the PYTHIA output were grouped in several categories, tailored to the requirements of this analysis: neutral pions were treated as stable, i.e. as the final state measured by the experiment, because the daughter photons cannot be cleanly separated with the used detectors (see section 5.3). For all other particles, the standard decay modes and final states were used. Photons were subdivided based on their origin: decay of hadrons (except for neutral pions), so-called fragmentation photons that are radiated off a gluon, and prompt photons that are directly created in hard scatterings of partons of the incoming protons. Finally, all charged pions, kaons and (anti-)protons were subsumed under a group of (meta-)stable charged particles.

The detailed results of this simulation will be presented below as required. Here, only a resume of the outcome shall be presented. Figure 5.4 shows the p_T spectrum of the neutral pions or photons with the highest transverse momentum of each event. This spectrum cannot be compared directly to the usual pion- and photon spectra, as those are not restricted to the leading particle of each event. It can be seen that in p+p collisions, neutral pions are the dominant source of energy deposition by neutral particles in the BEMC. Prompt photons from γ+jet events are already down by a factor 5-10, depending on transverse momentum. The contributions from other hadronic decays and fragmentation photons are even smaller, and will often be neglected in the following discussions.

Figure 5.5 displays azimuthal correlations with different particle species as trigger particles. These correlations will be used as reference and compared to measurements in Au+Au collisions in the following.

5.2.2 BEMC Detector Simulation

Detector effects were studied independently from the PYTHIA simulation. For this purpose, GSTAR [59] has been used to simulate the BEMC response to the trigger particles from this analysis. GSTAR is based on GEANT [60], an established tool for the detailed simulation of detectors, and is the standard simulation tool for particle detection with the STAR detector. Neutral pions and single photons with high transverse momenta were simulated within the BEMC acceptance and run through the GSTAR simulation software. The phase-space was limited to $6\,\mathrm{GeV}/c < p_T < 20\,\mathrm{GeV}/c$ and $|\eta| < 1.2$, covering the relevant region for this analysis. Results of this analysis will be shown in section 5.3.2.

Charged particles have not been simulated within the scope of this thesis, as good parameterizations of the efficiencies of the reconstruction software are available.

5.3 Trigger Particles

Correlation analyses between high-p_T particles use a trigger particle that is assumed to be the product of a initial hard parton scattering, and study associated particles from the same or the opposite jet. Past analysis usually studied correlations between charged particles, and were therefore sensitive to correlations within dijets. This analysis extends the field to photons measured with the BEMC. Photons can be produced in a variety of reactions, as has already been shown in section 5.2.1. A large fraction of photons come from the decay of neutral pions, but as the opening angle of this decay is usually very small, the daughter photons deposit their energy in neighboring towers, and can not be clearly separated. The SMD detector can provide information about the number of photons contributing to a cluster and their positions, it does not provide precise information about their energies. All other significant sources of photons either produce single photons or photon pairs with

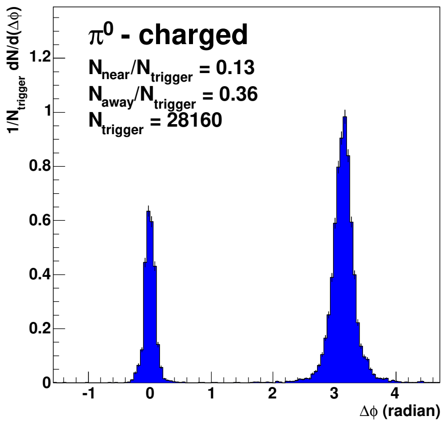

(a) π^0

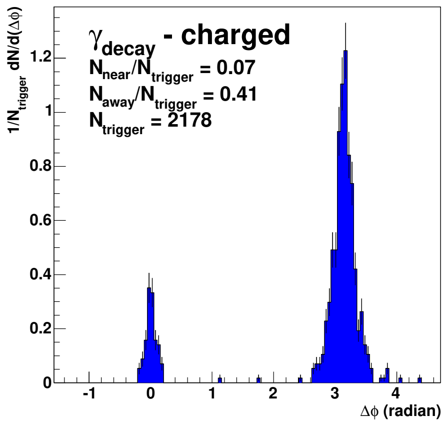

(b) hadronic decay photon (except π^0)

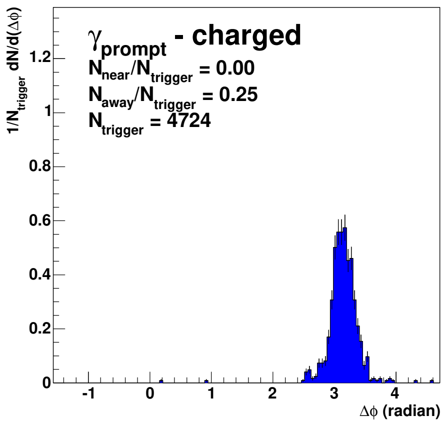

(c) prompt photon

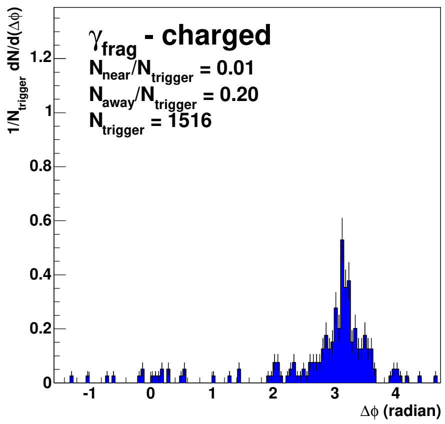

(d) fragmentation photon

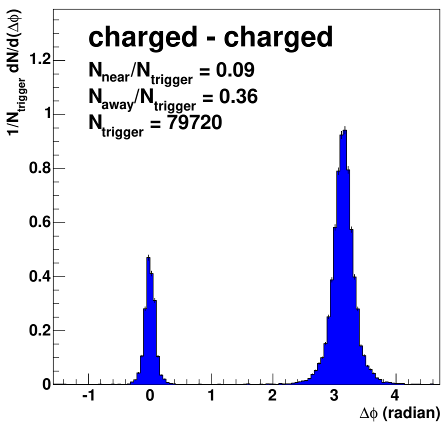

(e) charged hadron

Figure 5.5: Azimuthal correlations from PYTHIA simulations for different species of trigger particles. The plots show the distribution of the azimuthal angle between the highest trigger particle of the specified species with $E_T^{trigger} > 10\,\mathrm{GeV}$ and all charged particles from the same event with $4\,\mathrm{GeV} < p_T^{assoc} < \frac{1}{c}E_T^{trigger}$. For definition of particle species see text, for information about azimuthal correlations section 5.5.

a large opening angle that ensures that the photons leave well separated clusters.

This definition of trigger particles does not try to distinguish between neutral pions and single photons. Trigger clusters are constructed from towers that passed the level-0 and level-3 triggers, i.e. that had an ADC≥ 992. These towers are then used for clustering by adding the energy of the highest neighboring towers to account for energy sharing between towers. The influence of the cluster size on the reconstructed energy is described in section 5.3.2

While most energy deposition in the BEMC is caused by neutral particles, about 10% of the BEMC hits with high energy can be associated with charged particles. To remove this contribution, clusters with matching TPC tracks are vetoed as described in section 5.3.1.

For azimuthal correlations, the position of the pion or photon has to be reconstructed. This position is approximated by the center of the highest tower of the cluster. The resulting resolution of the azimuth of one tower or 50 mrad is sufficient for this analysis. Improvements would only be possible by using the SMD information, but this would require a separation of the showers generated by the two daughter photons of the neutral pion, which is not possible with the high efficiency necessary for this analysis.

5.3.1 Charged Track Veto

Although the main source of electromagnetic energy deposition in the calorimeters are photons from neutral pion decays and, in the most central events, direct photons production in hard scatterings, there is also a contribution of about 10% from charged particles. These particles are often electrons that develop an electromagnetic shower, or in fewer cases hadrons that shower with a smaller probability and a different shower profile and composition.

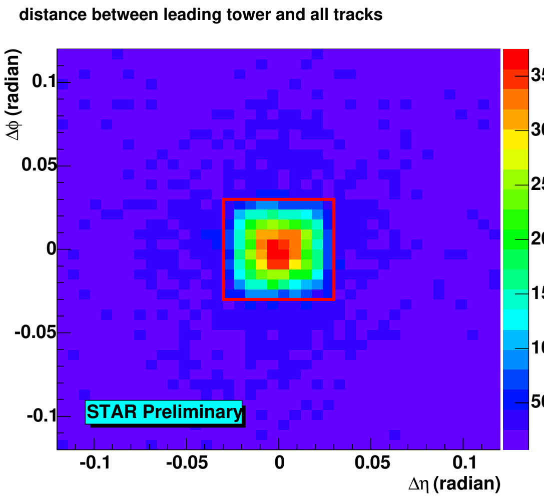

Figure 5.6: Distance between the trigger cluster of each event and all charged tracks with $p_T > 1\,\mathrm{GeV}$.

Both particle species can be vetoed by removing clusters that have a charged TPC track pointing to them. Figure 5.6 shows the matching between the trigger tower and tracks with $p_T > 1\,\mathrm{GeV}$ from the same event. The trigger cluster of the event was identified, and then all tracks matching the momentum cut were extrapolated to the BEMC. The distance in pseudorapidity $\delta\eta$ and azimuth $\delta\phi$ is then shown in the figure. Using a small δ rather than a capital Δ should emphasize the difference to the the variable $\Delta\phi$, which is frequently used for jet-like correlations, and which is measured at the vertex rather than the extrapolation to the BEMC. The rectangular shape of the tower with edges measuring 0.05 in pseudo-rapidity η and azimuth ϕ is clearly visible. The background consists of combinatorial background and jet-like correlations of charged particles with a leading neutral pion that are smeared out over a larger volume, because the width of a correlation due to jets is much bigger than a single tower, and because of the difference between the momentum direction at the vertex and at the radius of the BEMC.

Technically, the charged track veto cut is implemented using the isolation distance d_{iso}, which is the determined by finding the the track with $p_T > 1\,\mathrm{GeV}$ that extrapolates closest to the trigger tower, when measured in the maximum norm $\max(\delta\phi, \delta\eta)$:

$$d_{iso} = \min\{\max(\delta\phi_i, \delta\eta_i) : p_T(i) > 1\,\mathrm{GeV}/c\} \tag{5.1}$$

The maximum norm $\max(\delta\phi, \delta\eta)$ is preferred over the euclidean norm $\sqrt{\delta\phi^2 + \delta\eta^2}$, because it provides a quadratic rather than a circular area, matching the shape of BEMC towers.

The box in figure 5.6 marks the veto cut that was used throughout this analysis to remove charged tracks, unless otherwise noted: a trigger tower is rejected if a charged track with $p_T > 1\,\mathrm{GeV}$ extrapolates to within $|\delta\phi| < 0.03$ and $|\delta\eta| < 0.03$ from the center of the tower. This cut can be formulated as $d_{iso} \geq 0.03$. The quadratic veto area defined by this cut measures 0.06×0.06 in $\delta\phi$ and $\delta\eta$, and is slightly larger than a single tower. The effect of this cut on $\Delta\phi$-correlations will be studied in more detail in section 5.5.3, after these correlations are formally defined.

5.3.2 Energy Resolution

The two main sources of trigger particles are neutral pions and single electrons from prompt photon production or hadronic decays other than neutral pion decays. Photons produce only a single shower, and most of them deposit a large fraction of their energy in this single tower due to the Molière radius of $R_M \approx 1.6\,\mathrm{cm}$ in lead and the tower size of about $10\,\mathrm{cm} \times 10\,\mathrm{cm}$ in the central region. Only photons that hit the BEMC close to a tower boundary will produce showers that extend over two or more towers.

The situation for neutral pion decays into two photons is different. The opening angle for the decay $\pi^0 \to 2\gamma$ is at least 30 mrad for 10 GeV pions, which is not much smaller than the tower size of the BEMC (Figure 5.7). The two daughter photons will therefore either hit two neighboring towers, or a single tower near its edges, causing the

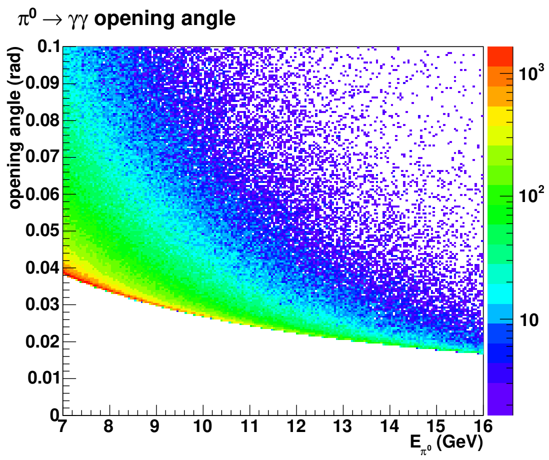

Figure 5.7: Opening angle of $\pi^0 \to \gamma\gamma$ decay. The opening angle of 30 mrad is close to the size of a tower ($\Delta\phi \times \Delta\eta \approx 0.05\mathrm{mrad} \times 0.05$)

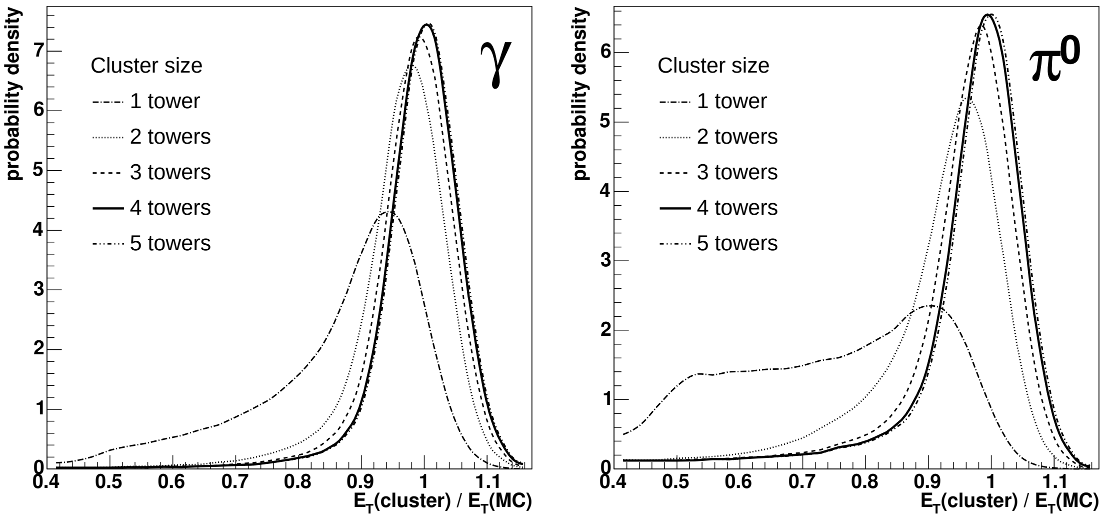

Figure 5.8: Energy resolution of photons and neutral pions for different cluster sizes. The reconstructed energy is divided by the simulated energy to determine deviations.

showers to deposit significant amounts of energy in the neighboring towers. In either case, the energy of the pion is distributed over several towers, and summation over these is necessary for a good energy resolution.

The number of towers that are used to form the cluster can be varied from 1 (only the tower that triggered on level-0/3) to 9 (all 8 neighbors are used). Figure 5.8 shows the ratio of reconstructed over simulated transverse energy as a function of cluster size for single photons (left panel) and neutral pions (right panel). On average, single photons deposit about 90% of their energy in a single cluster, with a tail towards lower fractions due to hits near the tower boundaries that develop showers that extend into the neighboring towers. Already a second tower in the cluster can recover most of the energy, and provides a nearly Gaussian distribution of measured energies, but with an offset of about 4% towards lower energies. When adding more towers to the cluster, the reconstructed energy moves closer to the energy of the simulated photon, and the spread gets smaller. Using more than four towers for the clustering does not change the reconstructed energy any further. For clarity, the curves for larger cluster sizes have been omitted.

For neutral pions a single tower is a poor approximation for the total energy. The energy of the highest tower can be between 40% and 100% of the originally simulated energy, with a peak around 90%. This large spread is caused by the large opening angle between the daughter photons giving a high probability for them to hit separate towers or the same tower near its edges, so that large parts of the showers develop in the neighboring towers. As more towers are added to the cluster, the accuracy improves, seen both by the reduction of the systematic shift of the reconstructed energy, and the decreasing width of the distribution.

The decision of trigger levels 0 and 3 was based on the energies of single towers, without

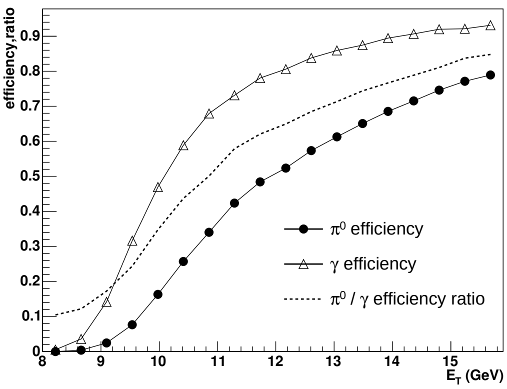

Figure 5.9: Trigger and reconstruction efficiency for photons and neutral pions, with a single tower threshold $E_T > 9\,\mathrm{GeV}$.

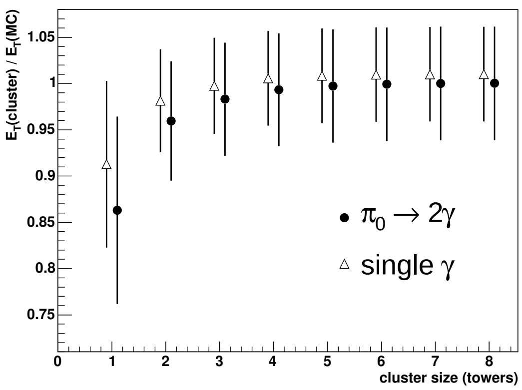

Figure 5.10: Transverse energy resolution of trigger clusters, with a single tower threshold $E_T > 9\,\mathrm{GeV}$.

any clustering. Therefore, the effect of the energy resolution on the trigger efficiency of the express stream trigger has to be taken into account. As explained in section 5.1.1, a threshold of $E_T > 9\,\mathrm{GeV}$ has to be applied to avoid the pseudo-rapidity dependence introduced by the incorrect calibration of the BEMC gains. The effect of this cut is shown in figure 5.9, that shows the efficiency to reconstruct a neutral pion or single photon as a function of transverse energy, if one tower with $E_T > 9\,\mathrm{GeV}$ is required.

After applying this cut, the energy resolution for different cluster sizes is shown in figure 5.10. It can be seen that the energy is underestimated by about 14% for neutral pions and 9% for single photons, when 1-tower clusters are used. With increasing cluster size, both the systematic undershoot as well as the event-by-event spread of the reconstructed value improve, up to a cluster size of four towers. Using a cluster size of five or more towers does not improve the precision significantly.

5.3.3 Definition of Trigger Particle

Trigger particles are built according to the following algorithm: towers that fulfill the level-0 and level-3 trigger cuts, i.e. that have an ADC> 992, and that have a higher transverse energy than all their neighbors are used as seeds. For each seed, the three neighbors containing the highest transverse energy are added to the cluster. For each event, only the cluster with the highest transverse energy is kept. The cluster is checked for matching charged tracks as described in section 5.3.1 to veto charged particles depositing energy in the BEMC. The transverse energy of the cluster is defined as the transverse energy of the seed plus the two neighbors that have been added. The center of the seed tower is used as the position of the cluster. If the cluster passes these cuts, it is called a *trigger cluster*. In the analysis, only trigger clusters with certain energies, usually $E_T > 10\,\mathrm{GeV}$ are used.

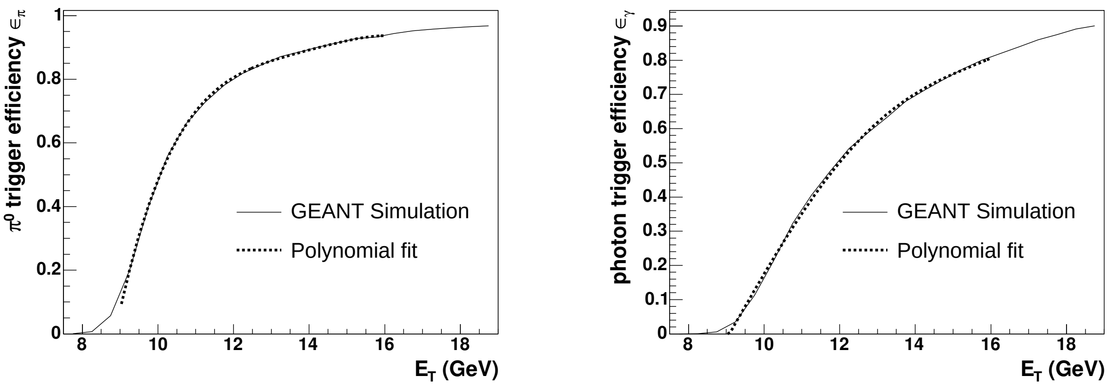

(a) single photons

(b) neutral pions

Figure 5.11: Parameterization of trigger efficiency for single photons and neutral pions. The GEANT simulation (solid line) is fitted with a fourth order polynomial in the range between 9 and 16 GeV (dashed line).

5.4 Associated Particles

To extract jet-like correlations, the trigger clusters that have been described in the last section are associated with charged tracks. These tracks are reconstructed with the TPC, STAR's main tracking device that is used as a standard tool in most analyses. The common quality cuts for TPC tracks have been applied in this analysis: tracks marked as bad by the reconstruction software were rejected as well as tracks with less than 20 hits. Primary tracks were selected for the analysis by requiring that the distance of closest approach (DCA) between the track and the primary vertex of the event was less than 1 cm. Only associated tracks with a transverse momentum of at least 2 GeV/c were used.

As the efficiency of reconstructing associated tracks enters directly into the correlation functions, it has to be determined and corrected for. For the determination of the efficiency, charged pions were simulated with GEANT and embedded into real events from different centrality classes. Figure 5.12 shows parameterizations of the efficiency for three different centrality classes. The efficiency decreases from about 80% in peripheral to 70% in central events. With increasing centrality a pseudo-rapidity dependence emerges, with the highest efficiency around $|\eta| \approx 0.8$, a minimum at mid-rapidity and a decrease towards the end of the TPC at $|\eta| = 1$.

5.5 Azimuthal Correlations

The next step is to correlate trigger clusters and associated particles. Each trigger cluster is combined with all tracks from the same event that fulfill the requirements for associated

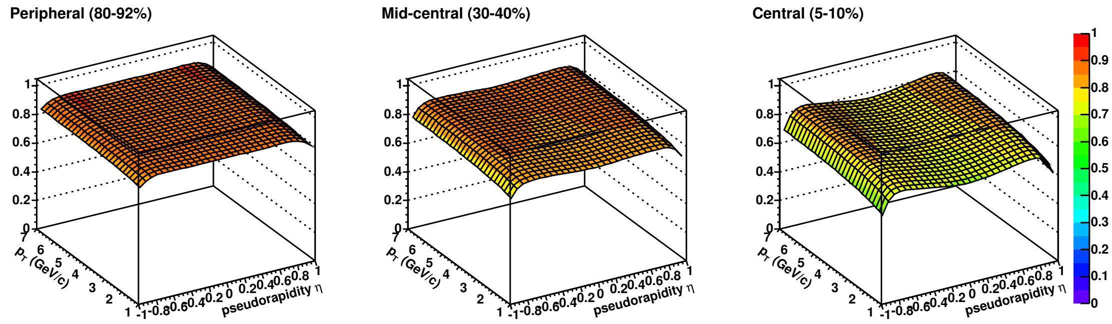

Figure 5.12: Reconstruction efficiency of charged particles, for peripheral (left), mid-central (middle) and central (right) events, as a function of pseudo-rapidity and transverse momentum.

particles. For each combination, the difference of the azimuthal angle of the trigger cluster and the momentum of the associated track at the primary vertex is calculated and moved to a range between $-\frac{1}{2}\pi < \Delta\phi < \frac{3}{2}\pi$. This difference of the azimuthal angles $\Delta\phi$ is then weighted with the inverse of the efficiency ($w = 1/\epsilon$) for the associated track to correct for reconstruction losses, and filled into a histogram.

Figure 5.13 shows an overview of the available data. $\Delta\phi$ correlations are shown for minimum bias Au+Au collisions at $\sqrt{s_{NN}}$ =200 GeV. With the available data set, the accessible transverse momentum ranges extend to more than 15 GeV for trigger and more than 9 GeV for associated particles. It can be seen that the background does not depend on the choice of the trigger particle, but only on the associated particle. For associated particles with transverse momenta below 4 GeV/c, a large random background can be observed, that decreases rapidly with an increasing cut on the momentum of the associated particle. For transverse momenta above 4 GeV, the background is still visible, but corresponds to 0.01 to 0.02 per radian and event, or less than one particle in ten events. This background is extremely low compared to correlations between charged particles that have been analyzed with previous datasets [61, 30]. Therefore, the systematic uncertainties due to background subtraction are greatly reduced, and allow the extraction of near- and away-side yields per trigger particle even with the low numbers of collected pairs.

On top of the background sit the two characteristic peaks of jet-like correlations. The near-side peak at $\Delta\phi \approx 0$ is due to charged particles from the same jet as the neutral particle that generated the trigger cluster, and that is usually a neutral pion that decayed into two photons. In $\gamma +$ jet events, the trigger photon is not part of a jet, and these events do therefore not contribute to the near-side correlation. The away-side correlation at $\Delta\phi \approx \pi$ is a mixture of $\gamma +$ jet and dijet contributions, where the opposite jet is measured that balances the momentum of the trigger photon or the jet that contains the trigger pion.

The difference of azimuthal correlations in central and peripheral events is shown in figure 5.14. The background is higher for central events, due to their higher multiplicity. As in correlations between charged particles, the away-side yield decreases with increasing

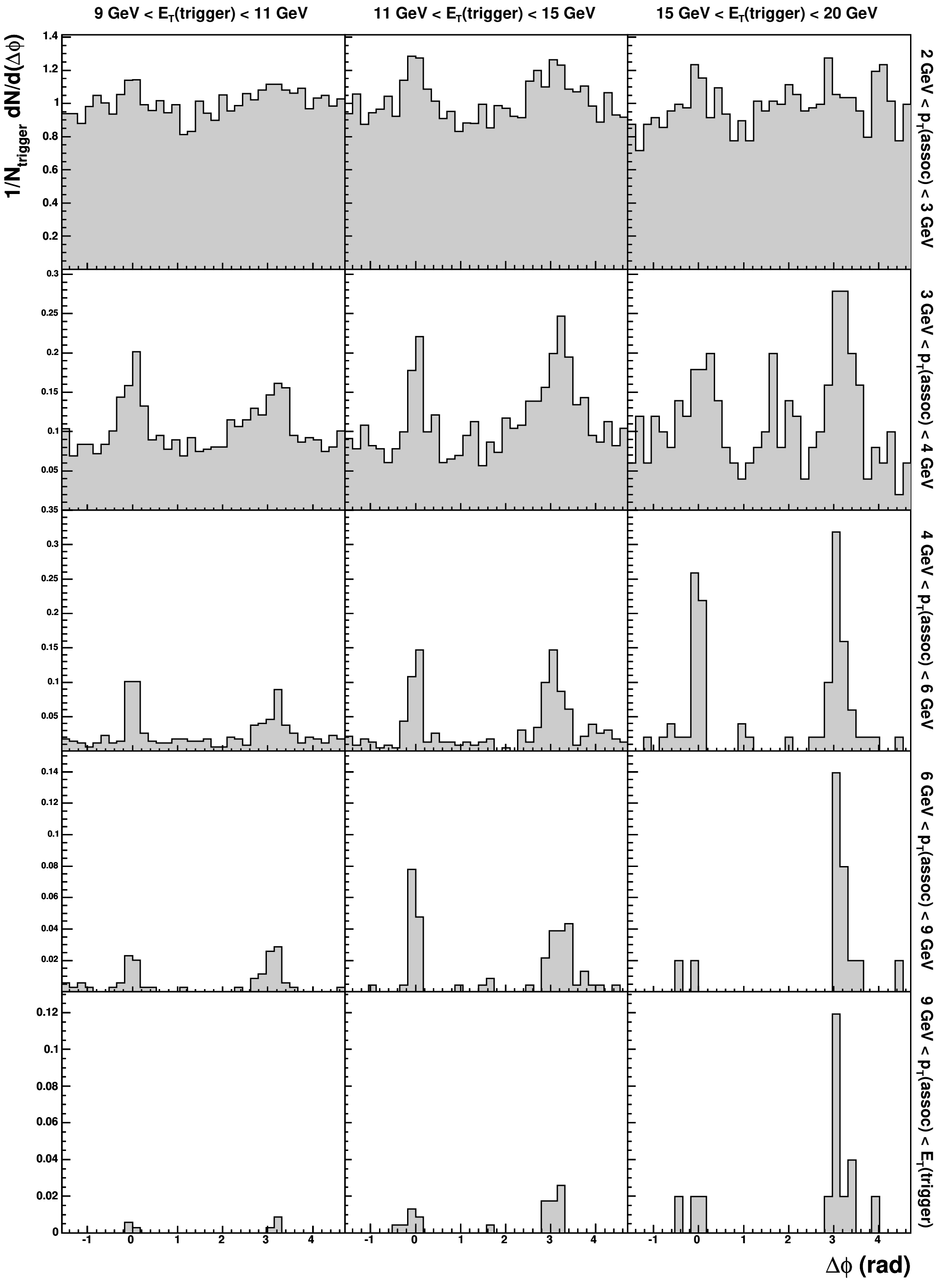

Figure 5.13: $\Delta\phi$ distributions in minimum-bias events for different $E_T^{trigger}$ and p_T^{assoc} ranges. The distributions are corrected for the tracking efficiency of the associated particle. A charged track veto has been applied.

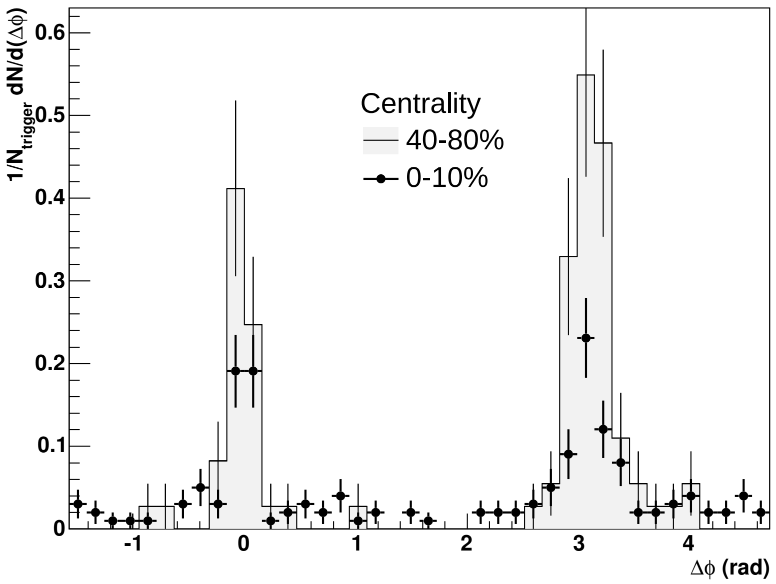

Figure 5.14: $\Delta\phi$ distributions with $E_T^{trigger} > 11\,\mathrm{GeV}$ and $4\,\mathrm{GeV}/c < p_T^{assoc} < E_T^{trigger}/c$ in central (solid circles) and peripheral events (shaded area).

centrality, a phenomenon that is explained by energy loss of the parton traversing the medium created in a heavy ion collision.

The behavior of near-side correlations is different: while no decrease in the associated near-side yield has been observed in correlations of charged particles, there is a clear reduction of the near-side yield in correlations between neutral trigger and charged associated particles. The reason for this decrease is the large fraction of $\gamma +$ jet events, that will be discussed in the next chapter (6.3).

The low available statistics do not allow for a detailed analysis of the shape of the correlation function, that would reflect modifications of the spatial structure of the jet when traversing the medium. A strong broadening, as it has been observed at lower transverse momenta of the associated particles [30], is not visible at these energies.

5.5.1 Background Shape

The background comes from random combinations of trigger clusters with high-p_T-tracks from the underlying event. The azimuthal distribution of these particles is not uniform, but depends of the azimuthal angle relative to the reaction plane of the collision, and therefore random combinations of particles will not result in a uniform distribution of the difference between the azimuthal angles of the combined particles. The calculation of the background shape for is carried out in appendix B. When the azimuthal anisotropy of trigger and associated particles is approximated by $dN/d\phi = C(1 + 2v_2 \cos 2\phi)$, then the shape of the background is given by:

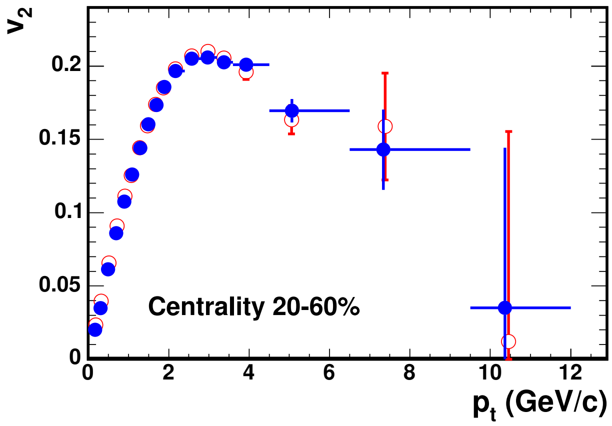

Figure 5.15: Azimuthal anisotropy $v_2(p_T)$ from a modified reaction plane (solid symbols) and two-particle cumulant method (open symbols) from [62].

$$\frac{dN(\Delta\phi)}{d\Delta\phi} = C\left(1 + 2v_{2T}v_{2A}\cos\left(2\Delta\phi\right)\right) \tag{5.2}$$

This formula, that is derived in appendix B shows that the background for the two-particle correlations has the same cosine-shape as the azimuthal anisotropy, but the relevant parameter describing the relative strength of the cosine term is the product of v_2 for the trigger and associated particles. The azimuthal anisotropy has been measured in [62] and is shown in figure 5.15. It is known with good precision for charged particles with transverse momenta up to 6–7 GeV/c, covering most associated particles used in this analysis. The momenta of trigger particles are not covered with high precision: statistical errors get very large for transverse momenta above 7 GeV/c, and for the last bin at $p_T \approx 10\,\mathrm{GeV}/c$, the measured v_2 is below 0.05, with a large statistical error of more than 0.1. This data point is the best available approximation for the trigger particles used in this analysis, which are chosen with a transverse momentum of $p_T > 10\,\mathrm{GeV}/c$. Using the nominal v_2 for trigger and associated particles, the product $v_{2T}v_{2A}$ would be less than 0.01. The large error bars make it consistent with zero, but would also allow for values up to 0.03. It should be noted, that these values are for mid-central events, where the azimuthal anisotropy is maximal; for central events, the values would be even smaller. The large error bars do not allow for a precise determination of the background from this measurement, but the small inhomogeneity and the low level of the background for the correlation functions result in small errors of the extracted yields.

5.5.2 Determination of Associated Yield

For quantitative statements, the background-subtracted near- and away-side yields have to be determined. This is possible by integration of the $\Delta\phi$-histograms, or by fitting a

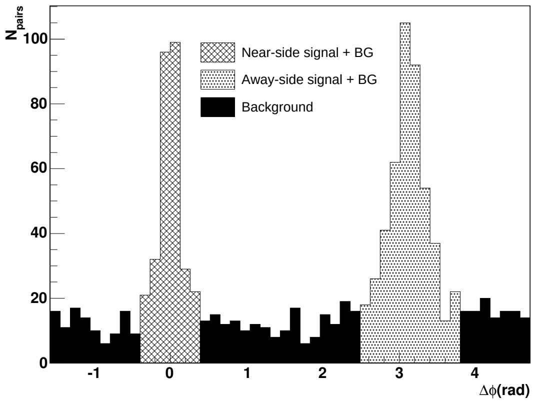

Figure 5.16: Extraction of yields by integration of background and near- and away-side peaks.

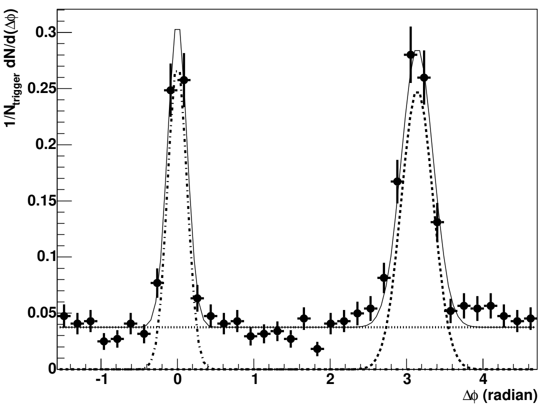

Figure 5.17: Extraction of near- and away-side yield by fitting of a constant background and Gaussian near- and away-side peaks.

function describing the background as well as near- and away-side peaks. In either case, a model for the background is necessary. As explained in the last section, a flat background is assumed.

The first method, the determination of associated yields by integration of $\Delta\phi$-histograms, is illustrated in figure 5.16. The histogram is divided into three regions: near-side, away-side and background region. The near-side region is centered around $\Delta\phi = 0$, and should contain the complete near-side peak and as little background as possible. A typical cut would be $|\Delta\phi| < 0.3$. Analogous, the away-side peak is centered around $\Delta\phi = \pi$, but as the away-side peak is wider than the near-side peak, the window should be wider as well. In this case, a typical cut is $|\Delta\phi - \pi| < 0.6$. The background region is everything that is not covered by either near- or away-side peak. In a first step, the background is determined by integrating the region between near- and away-side peaks. The associated yields are then calculated by integrating the near- and away-side regions, and subtracting the previously found background level.

The other method, the determination by fitting an appropriate function, is illustrated in figure 5.17. The fit function is the sum of a constant background and two Gaussian with fixed means at $\Delta\phi = 0$ and $\Delta\phi = \pi$ to describe near- and away-side peak. The fit function has five free parameters, one for the background term, and two for the width and the integral of near- and away-side peak.

Changes of the extracted yield for different extraction methods are compared in figure 5.18. The fit method (open symbols) is compared to the integration method (solid symbols) with three different integration ranges of $|\Delta\phi|$ <0.3, 0.4 and 0.5 for the near-side peak and twice the size on the away-side. The methods agree well for correlations with high transverse momenta of the associated tracks above $4\,\mathrm{GeV}/c$ (left panels). The largest deviations between the variations of the integration method for these associated momenta can be seen in the determination of the background in the most peripheral collisions. Due

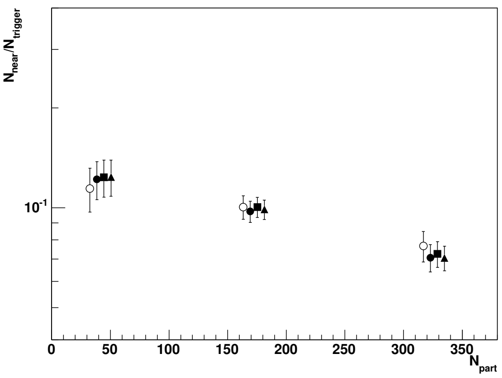

(a) near-side, $4\,\mathrm{GeV}/c < p_T^{assoc} < E_T^{trig}/c$

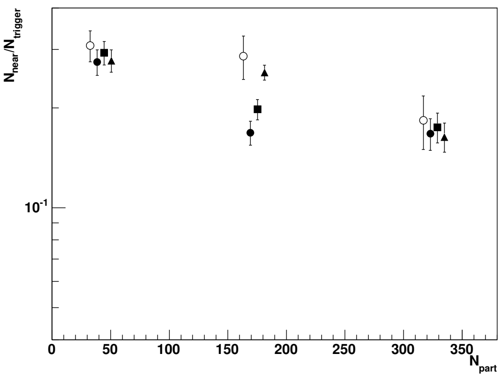

(b) near-side, $2\,\mathrm{GeV}/c < p_T^{assoc} < 4\,\mathrm{GeV}/c$

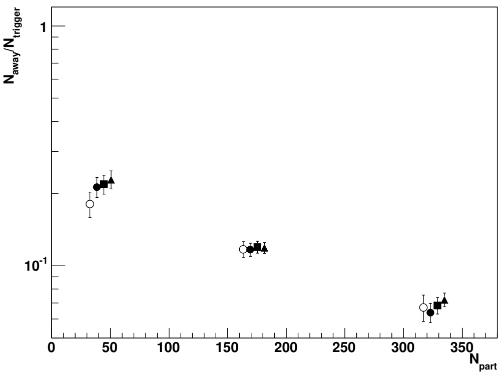

(c) away-side, $4\,\mathrm{GeV}/c < p_T^{assoc} < E_T^{trig}/c$

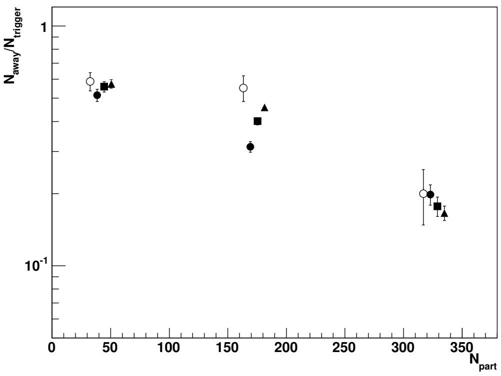

(d) away-side, $2\,\mathrm{GeV}/c < p_T^{assoc} < 4\,\mathrm{GeV}/c$

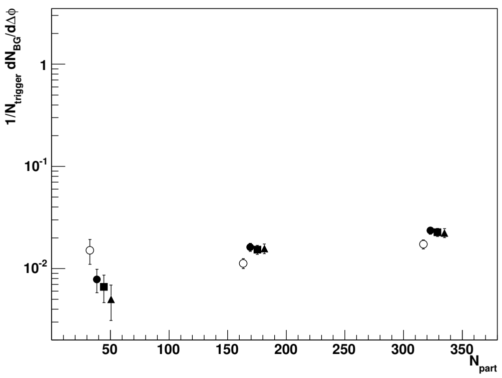

(e) background, $4\,\mathrm{GeV}/c < p_T^{assoc} < E_T^{trig}/c$

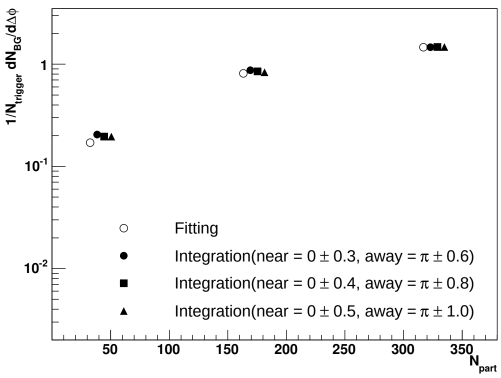

(f) background, $2\,\mathrm{GeV}/c < p_T^{assoc} < 4\,\mathrm{GeV}/c$

Figure 5.18: Associated near- and away-side yield and background in minimum bias Au+Au collisions for yield extraction by integration varying integration windows (solid symbols) and fitting of a constant background and Gaussian near- and away-side peaks (open). Data points are offset horizontally for clarity. The track veto cut has been applied, but not corrected for. Tracking efficiency of associated particles was corrected for.

to the large signal-to-background ratio (S/B), the extracted near- and associated yields are however hardly affected. The fitting method shows a tendency to underestimate all three values, near- and away-side yield as well as background in these cases. When the p_T cut for the associated track is lowered, the background level increases and unprecise background determination has a stronger impact on the extraction of near- and away-side yields. Especially in the case of mid-central events, the differences between the different integration regions become rather large.

From a statistical point of view, narrow integration windows around near- and away-side peaks are favorable, because they provide a broad region allowing for precise background determination, and small background contributions in the regions around the peaks. On the other hand, if the peak regions are chosen too narrow, too many associated tracks from jet-like correlations are found in the background region, increasing the reconstructed background and decreasing the associated yield.

The fitting method does not always reproduce the results of the integration method, especially for high transverse associated momenta it often undershoots those values. One source of disagreement could be the shape of near- and away-side peaks, which are not necessarily Gaussian as assumed in the fit function. It has also been observed that the determination of a background from a sparsely populated histogram does not yield reliable results. A last problem with the fitting method is of technical nature: the fit does not always converge, making it an uncomfortable choice for automated yield extraction.

In the following, preference is therefore given to the integration method. As a compromise between statistical and systematic uncertainties, the integration windows have been chosen as $|\Delta\phi| < 0.4$ for the near side and $|\Delta\phi - \pi| < 0.8$ for the away side.

5.5.3 Correction of Track Veto Cut

The charged track veto described in section 5.3.1 has a large impact on the extracted yields as well. On the near-side, the requirement not to see a charged track extrapolating to the trigger tower vetoes a certain fraction of neutral trigger particles, where an associated track from the same jet is falsely identified as the track generating the energy deposition. While it is not possible to avoid this misidentification on an event-by-event basis, it is possible to determine the strength of this effect and correct for it.

This misidentification effect can be studied by varying the size of the keep-out window. Figure 5.19 shows the variation of the extracted background as a function of the isolation distance d_{iso}, as defined in section 5.3.1. Subfigure (a) shows a clear enhancement of near-side correlations in Au+Au data, when only a small isolation distance is required. The additional yield is generated by charged particles that deposit energy in the BEMC, which is then correlated with the track measured by the TPC. To remove these auto-correlations, the required isolation distance has to be increased to at least the tower size, which is visualized by the shaded area in the plots. In this thesis, a track veto cut of $d_{iso} \geq 0.03$ is used unless otherwise stated.

The reduction of the observed near-side yield can be corrected by extrapolating the behavior for large isolations distances to an d_{iso}-cut of zero. The error bars leave the shape

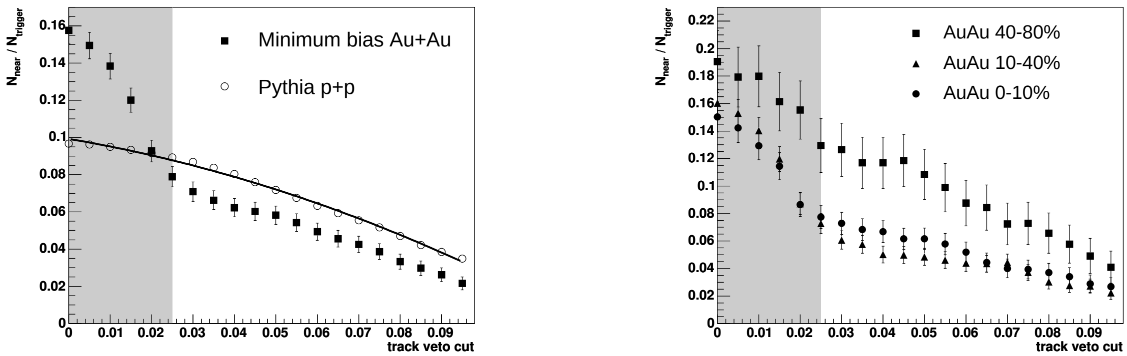

(a) near-side

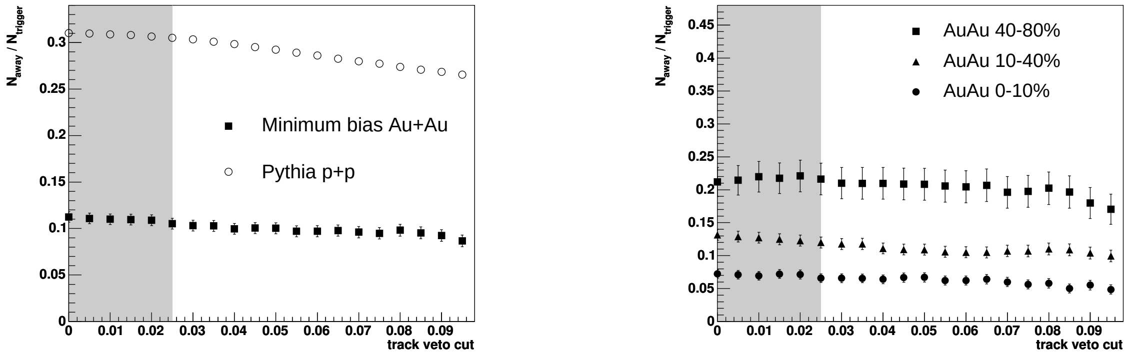

(b) away-side

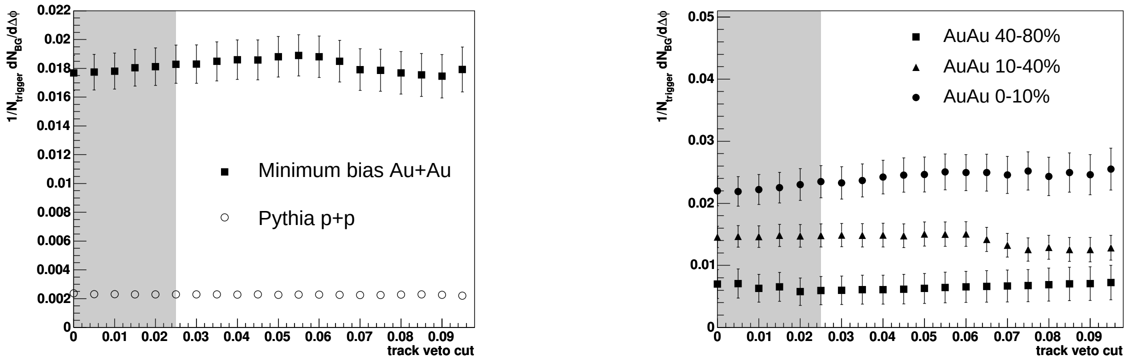

(c) background

Figure 5.19: Associated near- and away-side yield and background in minimum-bias Au+Au collision as function of isolation distance d_{iso}. Left panels show the PYTHIA simulations and minimum bias Au+Au data, right panels Au+Au data for different centralities. The shaded area visualizes the BEMC tower size.

of the functional dependency of the observed yield on the track veto, and especially its extrapolation to $d_{iso} \geq 0$, uncertain. A better handle is provided by a simulation, that only contains neutral trigger particles. In that case, the reduction can easily be determined. From the ratio of no extracted yield for no charged track veto cut, and the standard cut of $d_{iso} \geq 0.03$, the efficiency of this cut is retrieved as 89%. The extracted near-side yield will have to be corrected for this efficiency.

The away-side yield does not show the prominent enhancement from charged tracks, because these can only contribute to the near-side yield. A small dependency is however visible in the PYTHIA simulation. The dependency can be explained by the bias that the requirement of a track near the leading particle has on the jet properties: the absence of a very close energetic track will favor near-side jets with lower energies, lower multiplicities and wider profiles. It should also be noted that $\gamma+$jet events would not be vetoed by this cut. A precise correction for the reduced away-side would have to take these effects into account, and therefore require a good understanding of them. As these effects are very small and negligible in comparison to statistical uncertainties in the available dataset, they will not be corrected for in this analysis.

The background levels do not show any significant dependence on the veto cut, and are therefore not corrected.

5.5.4 Associated Yields

With the tracking efficiency of associated particles and the effect of the charged track veto cut, everything is known to calculate the associated yield per trigger particle. The yields presented in this section are determined with the procedure laid out on the previous pages:

- **Trigger particles** are found by constructing clusters around towers that were accepted by the level-0 and level-3 algorithms.
- A **charged track veto cut** is applied to remove charged particles from the trigger sample.
- **Associated particles** are chosen from the charged particles of the same event, if they fall within the correct transverse momentum bin.
- **Azimuthal correlations** between trigger and associated particles are determined by histogramming $\Delta\phi$, the difference of the azimuthal angle between trigger and associated particles.
- The **tracking efficiency** for the associated particles is corrected for by applying a weight $w = 1/\epsilon$ when histogramming $\Delta\phi$.
- **Associated near- and away-side yields** are calculated by integrating the regions around near- and away-side peaks, and subtracting the background level determined from the region between the peaks.

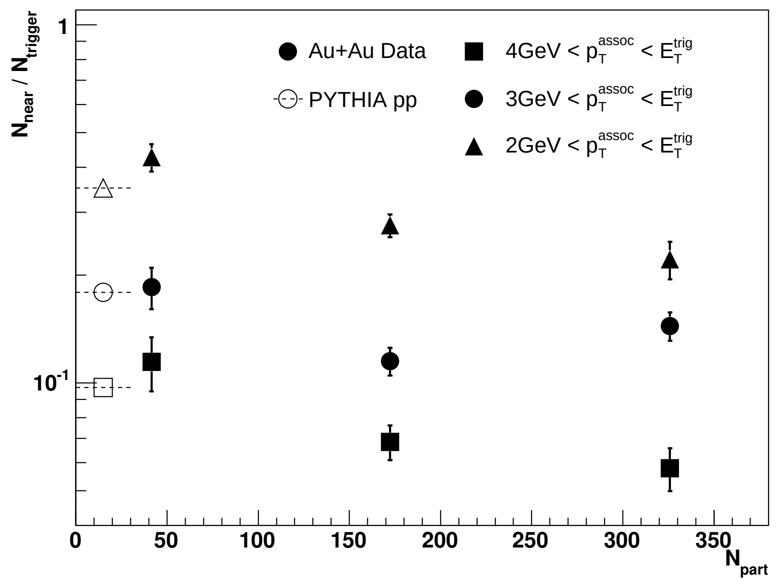

(a) near-side

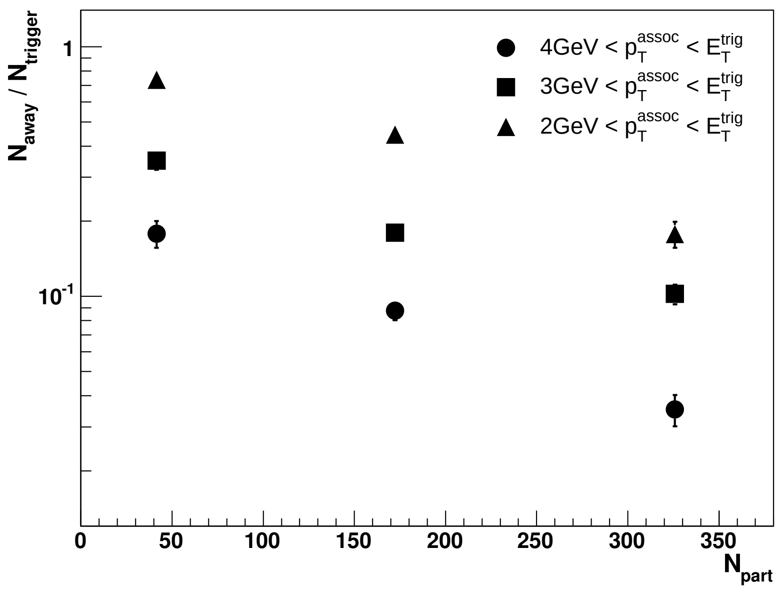

(b) away-side

Figure 5.20: Number of associated particles per trigger particle for near- and away-side correlations. The correlations strength is given for $10\,\mathrm{GeV} < E_T < 15\,\mathrm{GeV}$ and three different p_T^{assoc}-bins in three centrality classes of Au+Au collisions, and a PYTHIA simulation of p+p events at $\sqrt{s_{NN}} = 200\,\mathrm{GeV}$. The data has been corrected for tracking efficiency and the near-side track veto cut.

- The **correction for the track veto cut** is done by division of the associated near-side yield with the efficiency of this cut.

The associated yields extracted with this procedure are shown in figure 5.20. The away-side shows the well-known suppression of back-to-back correlations, but in contrast to analyses of correlations at lower transverse momenta, the back-to-back correlations do not disappear, but are still visible, even in the most central collisions. The reason for this could be either a reappearance of dijet correlations, or the first observation of $\gamma+$jet correlations in heavy ion collisions.

The near-side shows also a suppression of the associated yield in central collisions, which has not been seen in analyses at lower momenta, where a small increase was observed. The decrease can be explained by an increased fraction of $\gamma+$jet events, that do not have associated particles on the near side, and reduce the average yield per trigger particle on the near side.

An interpretation of the data in a more quantitative way will be given in the next chapter.

Chapter 6

Discussion of Results

The last chapter described the technical aspects of the analysis of azimuthal correlations with neutral trigger particles, leading to the yields of associated particles close to and opposite of the trigger particle. This chapter will use these results and attempt a physical interpretation. The first section will describe the contributions from neutral pions and photons from different sources to trigger particles and azimuthal correlations in a PYTHIA simulation of p+p collisions as a baseline for the comparisons in later sections. The second section then uses these simulations and data from the RHIC collider to extrapolate these finding to the environment of central Au+Au collisions. The last two sections will then compare the situation developed in this picture to the results from the analysis presented in this thesis.

6.1 Azimuthal Correlations in PYTHIA p+p Collisions

The description of azimuthal correlations in p+p collisions given in this chapter is based on the PYTHIA simulation described in section 5.2.1. The same classification of trigger particles as neutral pions, photons from decays of hadrons other than pions, fragmentation photons, and prompt photons from $\gamma + \text{jet}$ events was used. The analysis steps used for the analysis of the Au+Au data are applied analogously to the PYTHIA simulated events. The results from the GEANT simulation described in 5.3.2 are used to emulate cuts that could not be implemented directly on the simulated events, e.g. the ADC cut applied in the Level-3 trigger algorithm.

The first step in the analysis is the identification of trigger particles. Only the highest neutral particle within the acceptance of the BEMC is used as a trigger particle, and the selection is further constrained, mainly by a cut on the energy of the reconstructed cluster, which is assumed to be equal to the energy of the particle. The second step is then the association with charged particles from the same event. Again, as no full detector simulation was run, but all charged pions, kaons and (anti-)protons were used. With these associated particles, the distribution of azimuthal angles between the trigger particle and the associated charged particles from the same event was determined.

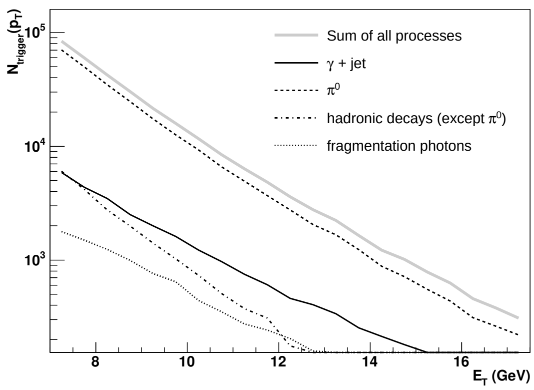

Figure 6.1: Spectrum of trigger particles in PYTHIA. Only the particle with the highest transverse energy of each event has been used.

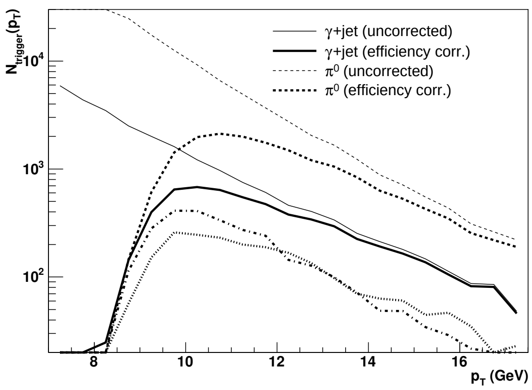

Figure 6.2: Spectrum of trigger particles in PYTHIA after correction for the efficiency of the trigger cut requiring a single tower with $E_T > 9GeV$.

The result of the first step, the selection of trigger particles, is shown in figure 6.1, still without a correction for the trigger efficiency of neutral trigger particles. It can be seen that the dominant source of trigger particles in the relevant transverse energy range between 10 and 15 GeV are neutral pions, that are almost ten times more abundant than the next class of trigger particles, direct photons. Even smaller contributions come from other hadronic decays and fragmentation photons. The ratio between neutral pions and prompt photons decreases between 10 and 15 GeV from about 8 to about 4, a higher energy range for the trigger particle will therefore always select a higher fraction of $\gamma + \text{jet}$ events. For the energy range used here, the ratio is $\pi^0 : \gamma_{pr} = 6.3 : 1$.

The efficiency of the Level-3 algorithm will modify the spectra of trigger particles, and the modification will be different for single photons and neutral pions, that are measured via their decay into two photons. These efficiencies are described in section 5.3.2, and can be accounted for in this simulation by multiplication with the trigger particle spectra. The result is shown in figure 6.2. The efficiency correction affects neutral pions more than single photons, because neutral pions have wider clusters and usually less energy in the highest tower than single electrons. As a result, the spectrum of pion triggers is reduced stronger than the spectra for single photon triggers, and the spectra for neutral pions and prompt photons become nearly parallel in the studied transverse energy range. The ratio of the two trigger species is reduced to $\pi^0 : \gamma_{pr} = 3.5 : 1$.

With these trigger particles, azimuthal correlations can be constructed, according to the algorithm described in section 5.5. For the uncorrected set of trigger particles from the PYTHIA simulation, the azimuthal correlations are shown in figure 6.3. As can already be expected from the mix of trigger particles, correlations with neutral pions dominate both the near- and away-side peaks. In the near-side peak, the only other notable contribution is from decays of hadrons, because prompt photons are not created within a jet, and because the radiation of a photon that is hard enough for a trigger particle leaves only little energy

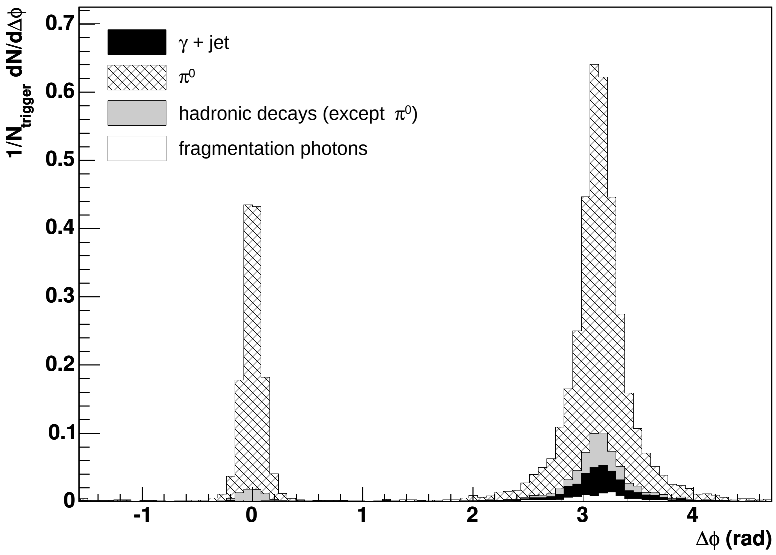

Figure 6.3: Azimuthal correlations in PYTHIA. No correction for experimental inefficiencies was applied.

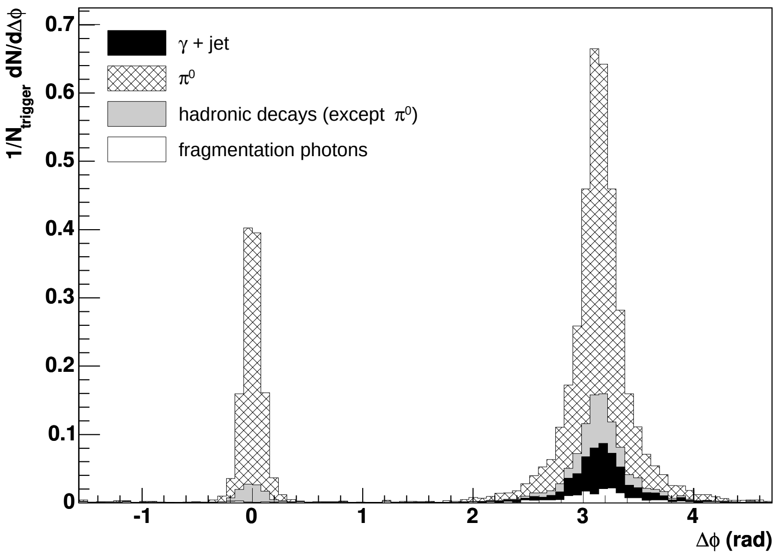

Figure 6.4: Azimuthal correlations in PYTHIA after correction for the efficiency of the trigger cut requiring a single tower with $E_T > 9GeV$.

for the creation of associated high-p_T particles in the jet fragmentation. On the away-side, the decay of hadrons from typical di-jet events is still the source of most correlated pairs. There is a small contribution from γ + jet events with a prompt photon providing the trigger, that is about as strong as the contribution from the decay of all hadrons except for neutral pions. Fragmentation photons do show a small away-side signal as well, that can however be neglected in comparison to the other processes.

The modification of the mix of trigger particles due to the trigger efficiency will also affect azimuthal correlations obtained from the analysis of these events. To include this effect in the simulation, the azimuthal correlation was constructed in a way that the contribution from each pair was weighted with the efficiency to reconstruct its trigger particle. The result is shown in figure 6.4. The overall shape of the correlation does not change by much, but the composition does: the importance of correlations with a neutral pion trigger is reduced, while the contributions from pairs with a single photon trigger are enhanced. Although a small effect in p+p collisions, this enhancement will be more important when the hadron suppression in Au+Au collisions is taken into account.

6.2 Extrapolation of PYTHIA to Central Au+Au

To understand the effects that modify the spectra of trigger particles and the azimuthal correlations, the results shown in the last section can be extrapolated to the situation in central Au+Au collisions using measurements from RHIC.

The nuclear modification factor R_{AA}, that describes the differences in the production of high-p_T particles in p+p and central Au+Au collisions, can also be used to describe the modification of the mix of trigger particles: neutral pions are suppressed by a factor $R_{AA} \approx 0.2$ for a wide transverse momentum range from 5 up to at least $20\,\mathrm{GeV}/c$ [63, 64], and a similar suppression can be assumed for other hadrons as well [21]. When extrapolating the PYTHIA simulation from p+p to Au+Au, neutral pions and single electrons from the decay of hadrons should therefore be scaled down by this factor.

The interest for prompt photons arises exactly from the fact that their lack of interaction with the medium results in unmodified prompt photon production in central Au+Au collisions. This has been confirmed by measurements at the RHIC collider [65]. Prompt photons will therefore not be scaled down in this extrapolation. The last group of trigger particles, fragmentation photons, is also the one with the largest uncertainties in the nuclear modification factor. The distinction from γ + jet events is difficult and the production cross section is even lower. No measurements are therefore available, and for this analysis, no modification in the presence of a hot medium is assumed. Due to the small cross section, moderate deviations from this assumption will not alter the conclusions in a significant way.

Figure 6.5 shows the consequences of scaling hadronic photon production down, while leaving the production of prompt and fragmentation photons untouched. For the hadron suppression $R_{AA} = 0.2$ was assumed. The production of photons from hadronic decays other than neutral pions, and the production of fragmentation photons are still small when

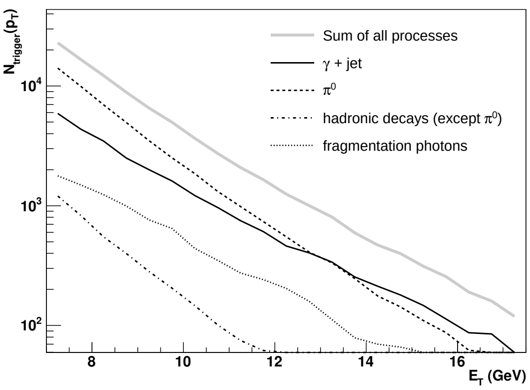

Figure 6.5: Trigger particles in PYTHIA, extrapolated to central Au+Au collision as described in the text. No efficiency correction was applied.

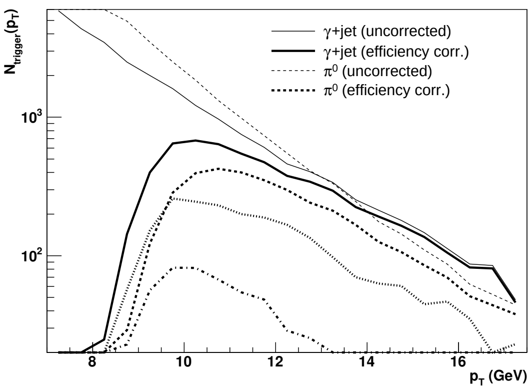

Figure 6.6: Efficiency Correction Trigger Particles in PYTHIA, extrapolated to central Au+Au collisions. The efficiency of the trigger cut has been accounted for.

compared to the production of neutral pions. In contrast to that, the spectrum of prompt photon triggers is comparable to the scaled pion spectrum, and prompt photon triggers even exceed the number of neutral pion triggers at transverse energies above 13 GeV. Averaged over the energy region between 10 and 15 GeV, neutral pion production still prevails with a ratio $\pi^0 : \gamma_{pr} = 1.3 : 1$. The trigger mix contains almost as many $\gamma + \text{jet}$ events as di-jet events with a neutral pion trigger.

Prompt photons are favored even more, when the trigger efficiency of the Level-3 trigger algorithm is taken into account. Due to the lower efficiency for pions, the number of accepted prompt photons exceeds the number of neutral pions over the full accessible range. In the relevant region, the ratio becomes $\pi^0 : \gamma_{pr} = 0.7 : 1$. In the central dataset, we therefore expect 40% more prompt photons than neutral pions. The effect is illustrated in figure 6.6.

For the modification of correlations, not only the suppression of the trigger particle has to be taken into account, but also the effect on associated particles. In the case of neutral pion triggers, a comparison to correlations between two charged hadrons gives a good reference, as the energy loss of the opposite-side jet should not depend on the details of the fragmentation of the jet providing the trigger particle. The quantity describing the suppression of correlations is I_{AA}, which has been defined in [29]. To avoid confusion with the back-to-back suppression in $\gamma + \text{jet}$ events, this quantity will be called $I_{AA}(hadr)$ in this text. For the extrapolation, we will assume $I_{AA}(hadr) = 0.1$, in agreement with the first measurement of this quantity [29], which is however a measurement at lower energies. Later results indicate slightly higher values of $I_{AA}(hadr)$ [30], but agree with the old measurements within errors.

The difference between R_{AA} and $I_{AA}(hadr)$ reflects the bias in the production location of the hard particles. High-p_T spectra of single particles, described by R_{AA}, are mainly sensitive to particles produced near the surface of the medium, that travel only a short

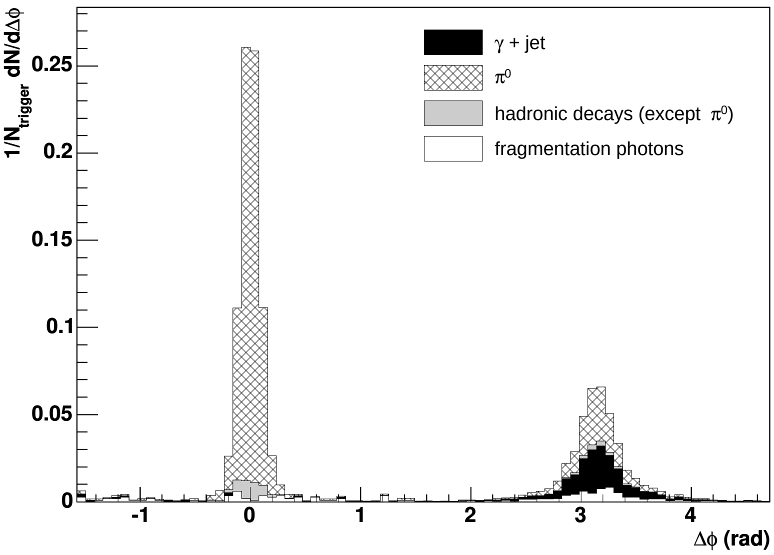

Figure 6.7: Azimuthal correlations in PYTHIA, extrapolated to central Au+Au collisions. No efficiency correction has been applied.

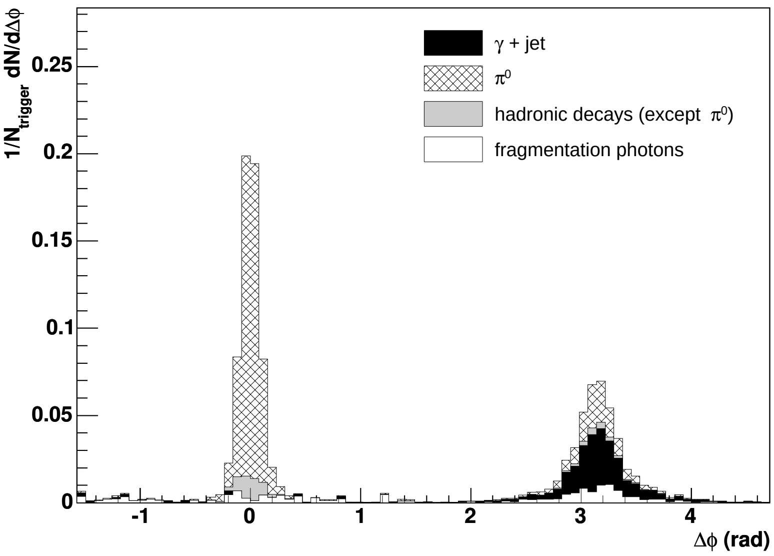

Figure 6.8: Azimuthal correlations in PYTHIA, extrapolated to central Au+Au collision and corrected for trigger efficiency.

distance before they leave the medium. In the case of back-to-back correlations, it is very unlikely that both jets have a short distance to the vacuum, because the surface bias of one parton would generally increase the path length for the opposite parton. For a discussion of this rather complex bias, see for example [66].

But also the jet opposite of a prompt photon will lose energy as it traverses the medium, with the result of a modification of away-side correlations in $\gamma + \text{jet}$ events. The situation is different from the back-to-back suppression in di-jet events, because there is no bias on the production location due to the trigger particle. As the situation is similar to the suppression of single particles, it will be assumed, that the parameter $I_{AA}(\gamma + \text{jet})$ that describes the suppression of the away-side correlation associated with a prompt photon trigger, is equal to the single particle suppression R_{AA}: $I_{AA}(\gamma + \text{jet}) = R_{AA}$.

Fragmentation photons are again assumed to behave like prompt photons, the away-side is therefore scaled down by R_{AA}.

Near-side correlations are assumed not to be modified by the presence of the medium. For the highest transverse momenta that were analyzed so far, only small deviations from correlations in p+p collisions were found [29, 67]. But, although the near-side correlations themselves have not been scaled, the lower fraction of triggers from di-jet events will reduce the overall associated near-side yield. This effect will be discussed in detail in the next section.

For the case of a trigger mix that has not been corrected for the trigger efficiency of the Level-3 algorithm, the resulting azimuthal correlations are shown in figure 6.7. When comparing to figures 6.3 and 6.4 from the last section, note the difference in scale. Compared to p+p collisions, the near-side yield is reduced by almost a factor of two, consistent with the higher fraction of prompt photon trigger particles without associated particles on the near-side. The suppression of the away-side is even more dramatic, reaching almost a factor 10. Also the high fraction of correlations from $\gamma + \text{jet}$ events is remarkable. Other hadronic decays and fragmentation photons still play a negligible role.

In figure 6.8, the azimuthal correlations are plotted for a trigger mix as expected in the most central collisions when taking the trigger efficiencies into account. The overall features are similar, but the signs of a high fraction of $\gamma + \text{jet}$ events are even more prominent: the near-side yield is even lower than in the case of no trigger efficiency correction, and contribution from $\gamma + \text{jet}$ correlations to the away side peak is almost 50%.

After this schematic description of the expected differences between p+p and Au+Au events, the next two sections contain a more quantitative interpretation of the data from this analysis.

6.3 Near-side Yield

As has been seen, one consequence of the increased fraction of prompt photon triggers is a decrease of the associated near-side yield. For the following reasoning, the contributions from hadronic decays other than neutral pion decays and from fragmentation photons will be neglected, so that only prompt photon and neutral pion triggers contribute.

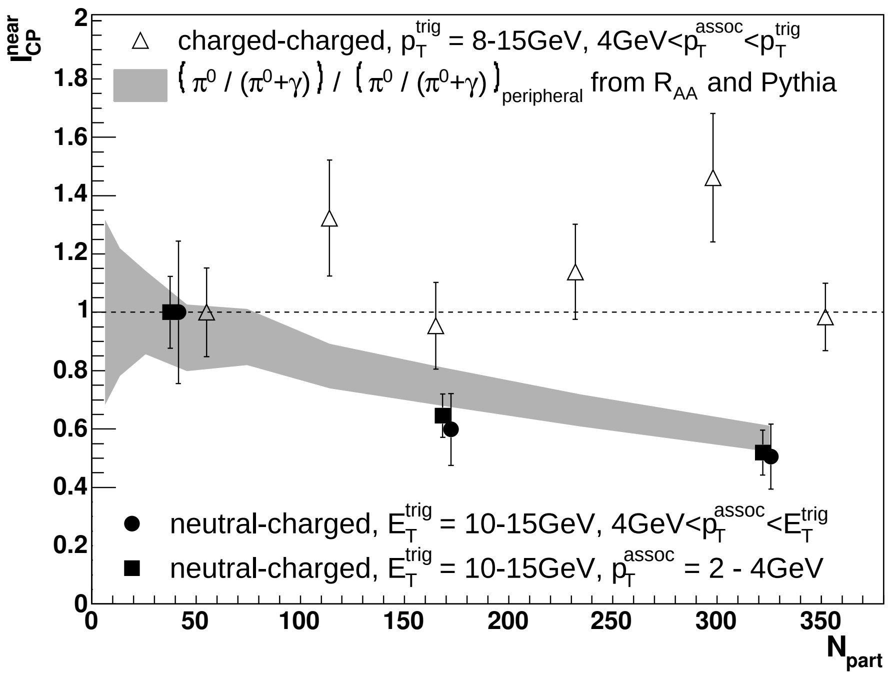

Figure 6.9: Near-side I_{CP} for correlations from this analysis (solid symbols), compared to expected decrease of near-side yield due to increasing fraction of $\gamma +$ jet events (grey band). Correlations of charged particles show no modification of the associated near-side yield (open symbols).

The near-side yield per neutral pion trigger n_π is assumed to be constant for all centralities. In that case, the associated near-side normalized to all trigger particles n is:

$$n = n_\pi \cdot \frac{N_\pi}{N_\pi + N\gamma} = n_\pi \cdot \frac{r}{1+r} \tag{6.1}$$

where r is the ratio of neutral pion to prompt photon triggers: $r = N_\pi / N\gamma$. An explanation of this and the following formulae can be found in appendix C. The associated near-side yield per neutral pion trigger n_π can be eliminated by comparing data at two different centralities. In analogy to I_{AA} and R_{CP}, one can define the ratio of associated yield in central and peripheral collisions:

$$I_{CP} := \frac{n(C)}{n(P)} = \frac{R_{AA}(C) \cdot (1 + r(pp) R_{AA}(P))}{R_{AA}(P) \cdot (1 + r(pp) R_{AA}(C))} \tag{6.2}$$

With the ratio of trigger species $r(pp)$ from the PYTHIA simulation and R_{AA} for different centralities from [63], I_{CP} can be calculated and compared to the associated near-side yields from this analysis.

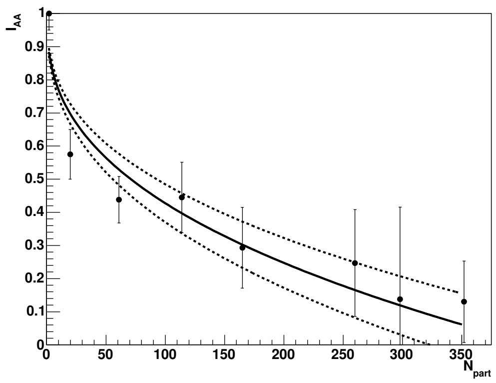

(a) I_{AA}

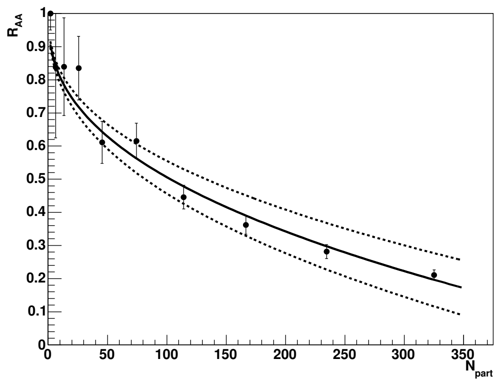

(b) R_{AA}

Figure 6.10: Parameterizations of R_{AA} and I_{AA}. Left panel: I_{AA} from [29] is fitted with a function $f(x) = 1 - Ax^{\alpha}$ (solid line). Uncertainties are marked by a $\pm 10\%$ variation of A (dotted lines). Right panel: Fit and variation of R_{AA} from [63].

Figure 6.9 shows the near-side I_{CP} as determined by this analysis (solid symbols). The near-side yield per neutral trigger particle has been normalized to the yield in the most peripheral event class. The yields agree well for two different transverse momentum ranges of associated particles. The grey band gives I_{CP} as expected when the ratio $\pi^0 : \gamma_{pr}$ is assumed to be $r(pp) = 3.5 : 1$ in p+p events, as was found in the PYTHIA simulation described in section 6.1. The expectation agrees well with the measured data. For comparison, the near-side I_{CP} of azimuthal correlations with charged trigger particles is also shown (open symbols), and confirms that the near-side yield in pure di-jet correlations does not depend on centrality. The observed decrease in correlations with neutral trigger particles can thus not be described by a modification of the near-side peak in hadron-hadron correlations.

We can therefore conclude that the mix of trigger particles behaves as described in the first two sections of this chapter: due to single particle suppression, the production of neutral pions is reduced, resulting in a decrease of the ratio of neutral pion to prompt photon triggers from $\pi^0 : \gamma_{pr} = 3.5 : 1$ in simulated p+p to $0.7 : 1$ in the most central Au+Au collisions. This means that in central Au+Au collisions almost 60% of the trigger particles are prompt photons from $\gamma +$ jet events.

6.4 Away-side Yield

The situation for away-side correlations is more complex. The associated yield for prompt photon triggers does not vanish as on the near-side, and di-jet correlations with neutral pion triggers also contribute. The away-side has therefore to be treated as a mixture of $\gamma +$ jet and dijet correlations. Furthermore, the modification of the correlations will be

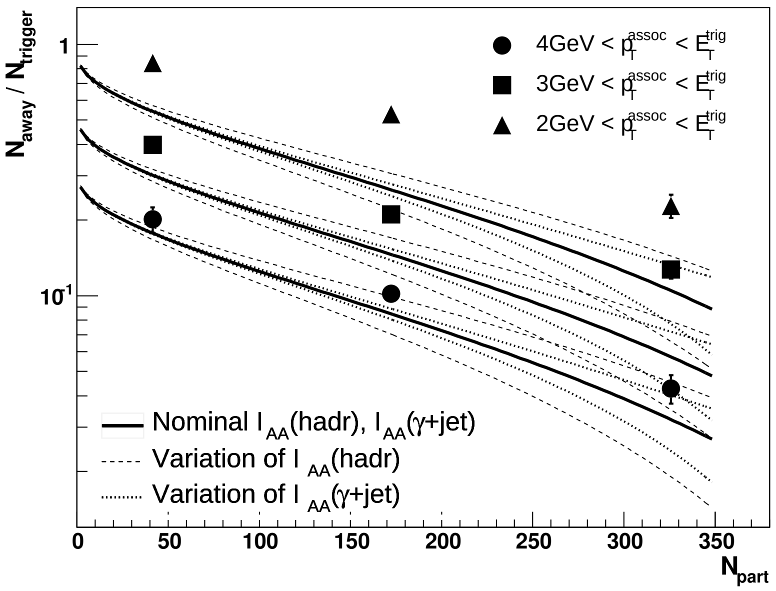

Figure 6.11: Comparison of away-side yield with first scenario: $I_{AA}(hadr)$ is taken from [29].

different for the two categories, because the trigger particles introduce different surface biases. A neutral pion trigger is subject to energy loss in the medium. Its observation therefore prefers short path lengths in the medium, i.e. a hard interaction point that is located on that side of the medium, where the neutral pion trigger is measured. A photon is not subject to energy loss, and therefore does not introduce any bias on the interaction point.

As a result, there is no simple expectation that can be compared to the data as in the case of near-side correlations. For a complete description of the data, it is not only necessary to know the mix of trigger particles and R_{AA} to describe its centrality dependence, but also the unbiased away-side yields per neutral pion and prompt photon trigger in p+p events a_π and a_γ, and their system and centrality dependences $I_{AA}(hadr)$ and $I_{AA}(\gamma + \text{jet})$. All these quantities are connected via the equation 6.3:

$$a(AA) = \frac{a_\gamma(pp) I_{AA}(\gamma + \text{jet})}{1 + r(pp) R_{AA}} + \frac{a_\pi(pp) I_{AA}(hadr) r(pp) R_{AA}}{1 + r(pp) R_{AA}} \tag{6.3}$$

The associated yields can no longer be eliminated by comparing data at two different centralities, and have to be determined in a different way. Direct measurements are difficult due to the mixture of different trigger species, and then only PYTHIA simulations can be used. So far, no reference data of azimuthal correlations in p+p collisions is available, and therefore no cross-check of the simulations is possible. When the associated yields from the simulation are used, there are still two independent quantities describing the modification of the away-side yield, $I_{AA}(hadr)$ and $I_{AA}(\gamma + \text{jet})$. As the knowledge of

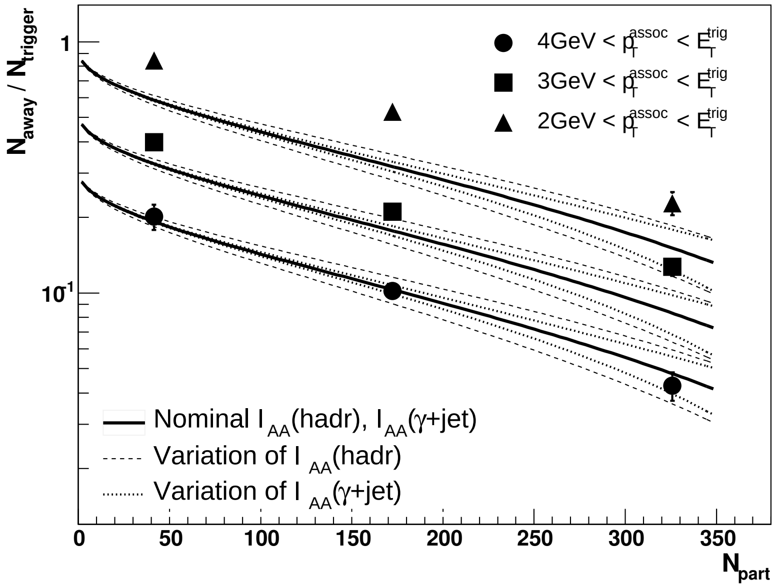

Figure 6.12: Comparison of away-side yield and second scenario $I_{AA}(hadr)$ is assumed to equal R_{AA} from [63].

one quantity is necessary to determine the other, and as both are still unknown for the studied momentum range, it will not be attempted to extract the values directly, but only to sketch out a possible scenario.

The quantity $r(pp)R_{AA}$ in equation 6.3 can be assumed to be known relatively well, because this is also the quantity that determines the near-side yield, and section 6.3 has shown that the expected and measured near-side yields are in good agreement. The unbiased associated yields a_π and a_γ from the PYTHIA simulation are probably also under better control than the modification factors $I_{AA}(hadr)$ and $I_{AA}(\gamma + \mathrm{jet})$.

The away-side suppression in di-jet events can be measured by azimuthal correlations with a charged trigger particle: the fragmentation of the jet providing the trigger particle has no influence on the propagation of the opposite jet through the medium. An analysis of azimuthal correlations of charged particles at lower transverse momenta only provided $I_{AA}(hadr)$ with very large error bars [29], as is shown in the left panel of figure 6.10. The large error bars for the most central collisions are consistent with values between 0 and 0.25. However, as this is to date the best published data, it will be used as one possible scenario for $I_{AA}(hadr)$. The data has been fitted with a function of the form $f(x) = 1 - Ax^\alpha$ to obtain a smooth parameterization for $I_{AA}(hadr)$ (solid line). To illustrate the uncertainties, the fit parameter A has been varied by $\pm 10\%$ (dashed lines).

A second scenario, which can be considered as an upper limit for $I_{AA}(hadr)$, has been inspired by the fact that the numerical values of the nuclear modification factor and $I_{AA}(hadr)$ are consistent within errors: it is assumed that $I_{AA}(hadr) = R_{AA}$. R_{AA} has been taken from [63], and is shown in the right panel of figure 6.10. Again, a smooth function of the form $f(x) = 1 - Ax^{\alpha}$ has been fit to the data, and a 10% variation of A gives an estimate of the uncertainty when setting $I_{AA}(hadr)$ equal to R_{AA}.

As explained before, the away-side suppression in γ + jet correlations should be more similar to the suppression of single charged particles than to the back-to-back suppression in di-jet correlations. The away-side suppression for prompt photon triggers will therefore be assumed to be equal to the single particle suppression: $I_{AA}(\gamma + \text{jet}) = R_{AA}$.

With these assumptions, it is now possible to compare the data to parameterizations of possible values for $I_{AA}(\gamma + \text{jet})$ and $I_{AA}(hadr)$. The first scenario is shown in figure 6.11, assuming that $I_{AA}(hadr)$ takes the nominal values from the STAR paper on the disappearance of back-to-back correlations [29], and assuming $I_{AA}(\gamma + \text{jet}) = R_{AA}$. The dashed and dotted lines indicate the changes when the nominal values of $I_{AA}(hadr)$ and $I_{AA}(\gamma + \text{jet})$, respectively, are varied as described above. This scenario fails to describe the data for associated particles with a transverse momentum of less than 4 GeV/c. The differences get smaller at higher transverse momenta, and for associated particles with transverse momenta above 4 GeV/c, the data is compatible with the upper limit of the assumed range for $I_{AA}(hadr)$.

In the second scenario it was assumed, that the di-jet and the γ + jet components of the away-side correlations can be described by the same parameterization, which is numerically equal to R_{AA}: $I_{AA}(hadr) = I_{AA}(\gamma + \text{jet}) = R_{AA}$. This case is illustrated in figure 6.12, and it can be seen that the agreement is better than in the first scenario. The general trend that harder correlations are described better is still visible, and for the associated particles with the highest transverse momenta, the description fits the data very well.

These parameterizations are not a model for the description of the data, but they can provide a first estimate for the suppression of the associated away-side yield in hadron- and prompt-photon-triggered correlations.The hardest azimuthal correlations with associated particles with momenta above 4 GeV/c, are described quite well by assuming that $I_{AA}(hadr)$ and $I_{AA}(\gamma+\text{jet})$ are numerically similar to the nuclear modification factor R_{AA}, which is about 0.23 in central collisions.

When decreasing the lower transverse momentum cut for the associated particles, the parameterizations can no longer describe the data and underestimates the actual measurements. It seems that the overall I_{AA} is not constant, but decreases for increasing transverse momentum of the associated particles. This might be an indication, that the low-p_T region, where an increased associated away-side yield has been observed [30], extends to more than 2 GeV/c for the trigger particles with very high transverse momentum that were selected for this analysis.

6.5 Conclusions

This chapter has shown that the analysis method presented in this thesis can be used to study azimuthal correlations with prompt photons as trigger particles. The near-side yield is a good measure for the fraction of trigger particles from γ + jet events, and the data agrees well with the expectation, that is based on PYTHIA simulations and the known nuclear modification factor for neutral pions. We can conclude, that the trigger particle mix selected for this analysis contains almost 60% prompt photons from $\gamma + \text{jet}$ events.

Due to the mixture of species in the set of trigger particles, it is not possible to determine exact values for $I_{AA}(hadr)$ and $I_{AA}(\gamma + \text{jet})$. The data for associated particles with high transverse momenta is consistent with the assumption, that both components of the away-side correlation signal are suppressed by a factor of 5. Correlations including associated particles with lower transverse momenta are less suppressed, and indicate a transition towards the low-p_T region with an enhancement of associated particle production.

Chapter 7

Summary

This thesis presented an analysis of azimuthal correlations at high transverse momentum using photons and neutral pions as trigger particles and charged associated particles. The measurements were carried out using the Barrel Electromagnetic Calorimeter and the Time Projection Chamber of the STAR experiment at RHIC. The selection of events with high energy deposition in one BEMC-tower with the Level-0 trigger, and the refinement of this condition on the Level-3 online reconstruction farm allowed the flagging of selected events for an express stream: the storage in a separate set of files and prioritized offline reconstruction. With this setup, the dataset was reduced from almost 200 million Au+Au collisions seen by the Level-0 trigger to only about 30 000 events containing the highest towers seen during one month of run-time.

Based on this dataset, neutral trigger particles were reconstructed with the BEMC, and an azimuthal correlation analysis with charged associated particles was performed. Due to the large sampled luminosity, it was possible to raise the transverse momentum ranges for trigger particles to more than $10\,\mathrm{GeV}/c$ and for associated particles to more than $4\,\mathrm{GeV}/c$, an increase of more than a factor of two when compared to older analyses. The results are extremely clear azimuthal correlation signals with a very low background level. Even in the most central Au+Au collisions, a clear away-side correlation is visible, that — for the first time in central heavy ion collisions — shows the narrowly peaked structure typical for jet-like correlations.

Due to the definition of the trigger particle, this analysis is not only sensitive to hadron-hadron correlation reflecting di-jet events, but also to $\gamma+\mathrm{jet}$ events, where a back-to-back pair of a photon and a parton are created in a hard scattering. The prompt photon from such a scattering will not be affected by the presence of a strongly interacting medium, and therefore provides the best measure for the properties of the opposite jet.

PYTHIA simulations along with known differences in high-p_T particle production between p+p and Au+Au collisions provide a good understanding of prompt photon and neutral pion production in Au+Au collisions. Based on this understanding, a reduction of the near-side yield with increasing centrality has been predicted. The simulation as well as the observed reduction of the near-side yield per trigger particle consistently give a fraction prompt photon triggers from $\gamma + \text{jet}$ events of almost 60% for the selected trigger particle mix.

Away-side azimuthal correlations are a combination of di-jet and γ+jet components, which are expected to be modified differently in the presence of hot nuclear matter. A quantitative disentanglement of these contributions requires more data, that was unfortunately not available on a timescale suitable for this thesis. The available data suggests a suppression of both contributions by a similar factor of about 0.2.

For the future, it is expected that a long Au+Au run of RHIC will provide dramatically increased statistics for this type of azimuthal correlations. The analysis is exceptionally well suited for triggering, allowing to take advantage of the full luminosity that RHIC can deliver. The completion of the BEMC will double the available acceptance, and the use of the Shower Maximum Detector of the BEMC could provide a better distinction between single photons and neutral pions, leading to a very pure sample of $\gamma + \text{jet}$ events.

Appendix A

STAR Coordinate System

The coordinate system used throughout this thesis is defined by the colliding beams in such a way that both particle beams run on the z-axis. The origin of the coordinate system is defined as the center of the experimental apparatus, which is also the mean position of collisions between beam particles. The x- and y-axes are then defined to be perpendicular to the z-axis and each other; the x-axis is parallel to the ground, and the y-axis vertical. The coordinate system does not move relative to the detector, and is therefore a laboratory system. Spatial coordinates are given as three-vectors (x,y,z). Instead of cartesian coordinates, it is often useful to use a cylindrical or spherical coordinate system.

In the cylindrical coordinate system, x and y are expressed in form of a cylinder radius r and an azimuthal angle, or azimuth, ϕ:

$$\begin{aligned} x &= r \sin\phi \\ y &= r \cos\phi \end{aligned} \tag{A.1}$$

Spherical coordinates transform x, y and z to an azimuth ϕ and a polar angle Θ, that give the position on a sphere with radius R:

$$\begin{aligned} x &= R \cdot \sin\Theta \cdot \sin\phi \\ y &= R \cdot \sin\Theta \cdot \cos\phi \\ z &= R \cdot \cos\Theta \end{aligned} \tag{A.2}$$

Momenta of particles involved in collisions can be given as their cartesian coordinates as well: (p_x,p_y,p_z). A frequently used term is *transverse momentum*, which is defined as:

$$p_T = \sqrt{p_x^2 + p_y^2} \tag{A.3}$$

The momentum can then be written in cylindrical coordinates p_T, p_z and the azimuthal angle ϕ. The beam particles by definition move along the z-axis and therefore do not carry any transverse momentum.

A particles longitudinal movement is often described by its *rapidity*, which is defined in terms of a particles longitudinal momentum p_z and energy E:

$$y = \frac{1}{2} \log \frac{E + p_z}{E - p_z} \tag{A.4}$$

The rapidity can be considered as a dimensionless, relativistic replacement for the velocity. The quantity has been constructed in such a way, that a Lorentz boost β along the z-axis will add a constant $\log(\gamma + \beta\gamma)$, making it a useful variable for easy changes between reference frames.

In the above formula for the rapidity y of a particle enters its energy E, so that the knowledge of the full four-vector describing its movement is necessary. Experimentally, the momentum is usually known, but energy and mass are often unknown, especially in a typical heavy-ion experiment that has to deal with extremely high particle multiplicities. In these cases, the rapidity cannot be calculated.

In that case, the rapidity of a relativistic particle can be approximated by another variable, that is defined purely by the momentum of the particle and can therefore be applied even in cases where the particle energy, and thus the rapidity, are unknown. Pseudo-rapidity is defined as a function of the polar angle Θ between the particle and the z-axis:

$$\eta = -\log \tan(\Theta/2) \tag{A.5}$$

In the STAR experiment, particle momentum is usually given as transverse momentum p_T, pseudo-rapidity η and azimuthal angle ϕ.

Appendix B

Combinatorial Background of Azimuthal Correlations

Anisotropies of the azimuthal distribution of particles produced in a heavy-ion collision will also lead to inhomogeneities of azimuthal correlations between random particles from the same event. Based on the azimuthal anisotropy of particle production, the background shape can be calculated.

The azimuthal distribution of particles $dN/d\phi$ relative to the reaction plane, determined by its azimuthal angle Ψ_{RP}, can be expanded in a Fourier series [68]:

$$\frac{dN}{d\phi} = \frac{N}{2\pi}\left(1 + \sum_{n=1}^{\infty} 2v_n \cos(n(\phi - \Psi_{RP}))\right) \tag{B.1}$$

In a collision of two identical nuclei, particle production must be symmetric at mid-rapidity, and all odd-numbered terms vanish. Dropping the first harmonic term due to this symmetry, neglecting all terms with $n > 2$, and measuring the azimuth ϕ relative to the reaction plane ($\Psi_{RP} = 0$), the azimuthal anisotropy can be written as:

$$\frac{dN}{d\phi} = \frac{N}{2\pi}\left(1 + 2v_2 \cos 2\phi\right) \tag{B.2}$$

The probability to find a pair of trigger (denoted with an index T) and associated particle (index A) with a difference of their azimuthal angles $\Delta\phi = \phi_T - \phi_A$ is then given by the product of the single particle anisotropies:

$$\frac{dN_{pairs}(\phi_T, \Delta\phi)}{d\phi_T d\Delta\phi} = \frac{dN_{pairs}(\phi_T, \phi_A)}{d\phi_T d\phi_A} = \frac{dN_T}{d\phi_T} \cdot \frac{dN_A}{d\phi_A} \tag{B.3}$$

Substituting the azimuthal distributions with equation B.2 and application of the identity $\cos x + \cos y = 2\cos\left(\frac{x+y}{2}\right)\cos\left(\frac{x-y}{2}\right)$ then yields:

$$\begin{aligned}
\frac{dN_{pairs}}{d\phi_T d\Delta\phi} &= \frac{N_T}{2\pi}\big(1+2v_{2,T}\cos(2\phi_T)\big)\frac{N_A}{2\pi}\big(1+2v_{2,A}\cos\left(2(\phi_T-\Delta\phi)\right)\big) \\
&= \frac{N_T N_A}{4\pi^2}\big(1+2v_{2,T}\cos\left(2\phi_T\right)+2v_{2,A}\cos\left(2(\phi_T-\Delta\phi)\right) \\
&\qquad + 4v_{2,T}v_{2,A}\cos\left(2\phi_T\right)\cos\left(2\left(\phi_T-\Delta\phi\right)\right)\big) \\
&= \frac{N_T N_A}{4\pi^2}\big(1+2v_{2,T}\cos\left(2\phi_T\right)+2v_{2,A}\cos\left(2(\phi_T-\Delta\phi)\right) \\
&\qquad + 2v_{2,T}v_{2,A}\left(\cos\left(4\phi_T-2\Delta\phi\right)+\cos\left(2\Delta\phi\right)\right)\big)
\end{aligned} \tag{B.4}$$

To eliminate the dependence on the azimuthal angle of the trigger particle, this formula must be averaged over all possible values of ϕ_T.

$$\begin{aligned}
\frac{dN_{pairs}(\Delta\phi)}{d\Delta\phi} &= \frac{1}{2\pi}\int_0^{2\pi}\frac{dN_{pairs}(\phi_T,\Delta\phi)}{d\phi_T d\Delta\phi}d\phi_T \\
\frac{dN_{pairs}(\Delta\phi)}{d\Delta\phi} &= \frac{N_T N_A}{8\pi^3}\Big(\int_0^{2\pi}1d\phi_T+\int_0^{2\pi}2v_{2,T}\cos 2\phi_T d\phi_T+\int_0^{2\pi}2v_{2,A}\cos 2(\phi_T-\Delta\phi)d\phi_T \\
&\qquad +\int_0^{2\pi}2v_{2,T}v_{2,A}\cos\left(4\phi_T-2\Delta\phi\right)d\phi_T+\int_0^{2\pi}2v_{2,T}v_{2,A}\cos\left(2\Delta\phi\right)d\phi_T\Big) \\
&= \frac{N_T N_A}{4\pi^3}\big(2\pi+0+0+0+4\pi v_{2,T}v_{2,A}\cos\left(2\Delta\phi\right)\big)
\end{aligned} \tag{B.5}$$

When performing the integration, note that all integrals $\int_0^{2\pi}\cos(n\cdot\phi_T)d\phi_T$ with $n = 1, 2, 3...$ will evaluate to 0. As the constant factor is usually determined from a fit to data, it can be replaced wit a simple constant $C = (N_T N_A)/4\pi^2$. Equation B.5 can then be written as:

$$\frac{dN_{pairs}(\Delta\phi)}{d\Delta\phi} = C\big(1+2v_{2,T}v_{2,A}\cos(2\Delta\phi)\big) \tag{B.6}$$

The background for $\Delta\phi$ correlations from random combinations of particles from the same event therefore takes a shape, that is very similar to the anisotropy of a single particle, i.e. a constant plus a cosine term. The relative strength of the cosine term is determined by the product of the v_2 values describing the azimuthal anisotropies of trigger particles.

Appendix C

Modification of Associated Yields

For a quantitative comparison between the extrapolation of PYTHIA p+p simulations to Au+Au events and the Au+Au data anlyzed in this thesis, the dependence of the associated yield on quantities like R_{AA}, $I_{AA}(hadr)$ and $I_{AA}(\gamma+\text{jet})$ must be known. Here, a few helpful relations are deduced.

C.1 Definitions

The definitions follow the terminology used in this thesis, especially in chapter 6, and are summarized here for reference:

N_γ and N_π are the number of prompt photon and neutral pion triggers, the sum $N_{trigger} = N_\pi + N_\gamma$ is the total number of trigger particles. The associated near- and away-side yields per trigger particle are denoted as n and a, respectively, with the system and centrality given in parentheses as necessary (e.g. $n(pp)$, $a(AA)$). An index γ indicates the associated yield per prompt photon trigger, a π analogous for neutral pion triggers (e.g. n_π is the associated near-side yield per neutral pion trigger). R_{AA} is the nuclear modification factor for single particle production, and $I_{AA}(hadr)$ and $I_{AA}(\gamma+\text{jet})$ describe the suppression of back-to-back correlations in di-jet and $\gamma+\text{jet}$ events. r is the ratio of neutral pion and prompt photon triggers $r := N_\pi/N\gamma$.

It is useful to note the system dependence of the ratio r terms of the ratio in p+p events and the nuclear modification factor:

$$r(AA) = \frac{N_\pi(AA)}{N\gamma(AA)} = \frac{R_{AA} \cdot N_\pi(pp)}{N\gamma(pp)} = r(pp)R_{AA} \tag{C.1}$$

C.2 Near-side Yield

Assuming that the near-side yield per trigger pion does not depend on the system, and that prompt photons do not have associated near-side particles, the near side yield can be written as:

$$n = \frac{N_{near}}{N_{trigger}} = \cdot \frac{n_\pi \cdot N_\pi}{N_\pi + N\gamma} = n_\pi \cdot \frac{r}{1+r} \tag{C.2}$$

It can be usefule to express this equation in terms of $r(pp)$ and R_{AA}:

$$n^{AA} = \frac{r(pp)R_{AA}}{1 + r(pp)R_{AA}} \cdot n_\pi^{pp} \tag{C.3}$$

When comparing different systems, the near-side yield n_π can be eliminated, and all variations can be expressed as a function of R_{AA} in these systems and $r(pp)$:

$$\begin{aligned} I_{CP} := \frac{n(C)}{n(P)} &= \frac{r(C)}{1+r(C)} \cdot \frac{1+r(P)}{r(P)} \\ &= \frac{r(pp)R_{AA}(C)}{1+r(pp)R_{AA}(C)} \frac{1+r(pp)R_{AA}(P)}{r(pp)R_{AA}(P)} \\ I_{CP} &= \frac{R_{AA}(C)\cdot(1+r(pp)R_{AA}(P))}{R_{AA}(P)\cdot(1+r(pp)R_{AA}(C))} \end{aligned} \tag{C.4}$$

C.3 Away-side Yield

Away-side correlations are a superposition of di-jet and $\gamma + \text{jet}$ contributions:

$$a = \frac{a_\gamma N_\gamma + a_\pi N_\pi}{N_\gamma + N_\pi} = \frac{a_\gamma + r a_\pi}{1+r} \tag{C.5}$$

The associated away-side yields for pion and $\gamma + \text{jet}$ triggers will be suppressed in AA collisions with different suppression factors for both trigger species:

$$\begin{aligned} a(AA) &= \frac{a_\gamma(AA) + r(AA)a_\pi(AA)}{1+r(AA)} \\ &= \frac{a_\gamma(pp)I_{AA}(\gamma + \text{jet}) + a_\pi(pp)I_{AA}(hadr)r(pp)R_{AA}}{1+r(pp)R_{AA}} \end{aligned} \tag{C.6}$$

Bibliography

[1] Siegfried Bethke. alpha(s) 2002. *Nucl. Phys. Proc. Suppl.*, 121:74–81, 2003, hep-ex/0211012.

[2] D. J. Gross and Frank Wilczek. ULTRAVIOLET BEHAVIOR OF NON-ABELIAN GAUGE THEORIES. *Phys. Rev. Lett.*, 30:1343–1346, 1973.

[3] H. David Politzer. RELIABLE PERTURBATIVE RESULTS FOR STRONG INTERACTIONS? *Phys. Rev. Lett.*, 30:1346–1349, 1973.

[4] Frithjof Karsch. Lattice QCD at High Temperature and Density. *Lect.Notes Phys.*, 583:209–249, 2002, hep-lat/0106019.

[5] Peter Braun-Munzinger. Chemical Equilibration and the Hadron-QGP Phase Transition. *Nucl.Phys. A*, 681:119–123, 2001, nucl-ex/0007021.

[6] T.D. Lee. Abnormal Nuclear States and Vacuum Excitations. *Rev.Mod.Phys.*, 47:267, 1975.

[7] New State of Matter created at CERN. CERN Press Release, February 2000.

[8] John C. Collins, Davison E. Soper, and George Sterman. Factorization of Hard Processes in QCD. *Adv. Ser. Direct. High Energy Phys.*, 5:1–91, 1988, hep-ph/0409313.

[9] J. Pumplin et al. New generation of parton distributions with uncertainties from global QCD analysis. *JHEP*, 07:012, 2002, hep-ph/0201195.

[10] J. Ashman et al. MEASUREMENT OF THE RATIOS OF DEEP INELASTIC MUON - NUCLEUS CROSS-SECTIONS ON VARIOUS NUCLEI COMPARED TO DEUTERIUM. *Phys. Lett.*, B202:603, 1988.

[11] Frank E. Close, Jian-wei Qiu, and R. G. Roberts. QCD PARTON RECOMBINATION AND APPLICATIONS TO NUCLEAR STRUCTURE FUNCTIONS. *Phys. Rev.*, D40:2820, 1989.

[12] D. Buskulic et al. Measurement of alpha-s from scaling violations in fragmentation functions in e+ e- annihilation. *Phys. Lett.*, B357:487–499, 1995.

[13] Stefano Moretti, Leif Lonnblad, and Torbjorn Sjostrand. New and old jet clustering algorithms for electron positron events. *JHEP*, 08:001, 1998, hep-ph/9804296.

[14] Gerald C. Blazey et al. Run II jet physics. 2000, hep-ex/0005012.

[15] S. Bethke et al. EXPERIMENTAL INVESTIGATION OF THE ENERGY DEPENDENCE OF THE STRONG COUPLING STRENGTH. *Phys. Lett.*, B213:235, 1988.

[16] R. Baier. Jet quenching. *Nucl. Phys.*, A715:209–218, 2003, hep-ph/0209038.

[17] J. D. Bjorken. Energy Loss of Energetic Partons in Quark-Gluon Plasma: Possible Extinction of High pT Jets in Hadron-Hadron Collisions. FERMILAB-Pub-82/59-THY, 1982.

[18] *Quark-Gluon Plasma 2*, chapter Applications of High Temperature Field Theory to Heavy Ion Collisions, page 51. World Scientific, 1995.

[19] Miklos Gyulassy and Xin-nian Wang. Multiple collisions and induced gluon Bremsstrahlung in QCD. *Nucl. Phys.*, B420:583–614, 1994, nucl-th/9306003.

[20] R. Baier, Yuri L. Dokshitzer, Alfred H. Mueller, S. Peigne, and D. Schiff. Radiative energy loss of high energy quarks and gluons in a finite-volume quark-gluon plasma. *Nucl. Phys.*, B483:291–320, 1997, hep-ph/9607355.

[21] J. Adams et al. Transverse momentum and collision energy dependence of high p(T) hadron suppression in Au + Au collisions at ultrarelativistic energies. *Phys. Rev. Lett.*, 91:172302, 2003, nucl-ex/0305015.

[22] C. Adler et al. Centrality dependence of high p(T) hadron suppression in Au + Au collisions at s(NN)**(1/2) = 130-GeV. *Phys. Rev. Lett.*, 89:202301, 2002, nucl-ex/0206011.

[23] C. Adler et al. Azimuthal anisotropy and correlations in the hard scattering regime at RHIC. *Phys. Rev. Lett.*, 90:032301, 2003, nucl-ex/0206006.

[24] Xin-Nian Wang. High p(T) hadron spectra, azimuthal anisotropy and back-to- back correlations in high-energy heavy-ion collisions. *Phys. Lett.*, B595:165–170, 2004, nucl-th/0305010.

[25] Ivan Vitev and Miklos Gyulassy. High-p(T) tomography of d + Au and Au + Au at SPS, RHIC, and LHC. *Phys. Rev. Lett.*, 89:252301, 2002, hep-ph/0209161.

[26] J. Adams et al. Evidence from d + Au measurements for final-state suppression of high p(T) hadrons in Au + Au collisions at RHIC. *Phys. Rev. Lett.*, 91:072304, 2003, nucl-ex/0306024.

[27] K. H. Ackermann et al. Elliptic flow in Au + Au collisions at s(N N)**(1/2) = 130-GeV. *Phys. Rev. Lett.*, 86:402–407, 2001, nucl-ex/0009011.

[28] M. Gyulassy, I. Vitev, and X. N. Wang. High p(T) azimuthal asymmetry in noncentral A + A at RHIC. *Phys. Rev. Lett.*, 86:2537–2540, 2001, nucl-th/0012092.

[29] C. Adler et al. Disappearance of back-to-back high p(T) hadron correlations in central Au + Au collisions at s(NN)**(1/2) = 200-GeV. *Phys. Rev. Lett.*, 90:082302, 2003, nucl-ex/0210033.

[30] J. Adams et al. Distributions of charged hadrons associated with high transverse momentum particles in p p and Au + Au collisions at s(NN)**(1/2) = 200-GeV. 2005, nucl-ex/0501016.

[31] M. Anderson et al. The STAR Time Projection Chamber: A Unique Tool for Studying High Multiplicity Events at RHIC. *Nucl. Instrum. Meth. A*, 499:659, 2003.

[32] R. Bellwied et al. The STAR Silicon Vertex Tracker: A Large Area Silicon Drift Detector. *Nucl. Instrum. Meth. A*, 499:640, 2003.

[33] L. Arnold et al. The STAR Silicon Strip Detector. *Nucl. Instrum. Meth. A*, 499:640, 2003.

[34] F. Bergsma et al. The STAR Detector Magnet Subsystem. *Nucl. Instrum. Meth. A*, 499:633, 2003.

[35] K.H. Ackermann et al. The Forward Time Projection Chamber (FTPC) in STAR. *Nucl. Instrum. Meth. A*, 499:713, 2003.

[36] F. Sauli. Principles of operation of multiwire proportional and drift chambers. Technical Report CERN 77-09, CERN, 1977.

[37] M. Beddo et al. The STAR Barrel Elecromagnetic Calorimeter. *Nucl. Instrum. Meth. A*, 499:725, 2003.

[38] F.S. Bieser et al. The STAR Trigger. *Nucl. Instrum. Meth. A*, 499:766, 2003.

[39] J.M. Landgraf et al. An Overview of the STAR DAQ System. *Nucl. Instrum. Meth. A*, 499:762, 2003.

[40] N. J. Boden, D. Cohen, R. E. Felderman, A. E. Kulawik, C. L. Seitz, J. N. Seizovic, and Wen-Ken Su. Myrinet — a gigabit-per-second local-area network. *IEEE Micro*, 15(3):29–36, 1995.

[41] J. M. Landgraf, C. Adler, M. J. LeVine, A. Ljubicic, Jr., J. M. Nelson, M. W. Schulz and J. S. Lange. The implementation of the STAR data acquisition system using a Myrinet network. *IEEE Trans. Nuc. Sci.*, 48(3), 2001.

[42] M.J. Levine, T.J. Ljubicic, J.M. Nelson. DAQ Backbone Communication Protocol. `http://www.star.bnl.gov/STAR/html/daq_l/Milestone1/documents/daq_protoc%ols_9_01.pdf`.

[43] C. Adler et al. The STAR Level-3 Trigger System. *Nucl. Instrum. Meth. A*, 499:778, 2003.

[44] D.A. Huffman. A method for the construction of minimum-redundancy codes. In *Proceedings of the I.R.E.*, pages 1098–1102, September 1952.

[45] J. Ziv and A. Lempel. A Universal Algorithm for Sequential Data Compression. *IEEE Transactions on Information Theory*, May 1977.

[46] M. Burrows and D. Wheeler. A block sorting lossless data compression algorithm. Technical Report 124, Digital Equipment Corporation, 1994.

[47] Christof Struck. *Antinuclei Production in Central Au-Au Collisions at RHIC*. PhD thesis, Johann-Wolfgang-Goethe Universität Frankfurt am Main, 2003.

[48] Jens Berger. *Anti-Proton to Proton Ratio in Au+Au Collisions at STAR*. PhD thesis, Johann-Wolfgang-Goethe Universität Frankfurt am Main, 2003.

[49] C. Adler, et al., The STAR Collaboration. Coherent rho0 Production in Ultra-Peripheral Heavy Ion Collisions. *Phys.Rev.Lett.*, 89(272302), 2002.

[50] Clemens Adler. *Der STAR Level-3 Trigger*. PhD thesis, Johann-Wolfgang-Goethe Universität Frankfurt am Main, 2003.

[51] Pablo Yepes. A Fast Track Pattern Recognition. *Nucl. Instrum. Meth. A*, 380:582, 1996.

[52] Ante Ljubicic, Jeff Landgraf. The DAQ100 Project. `http://www.star.bnl.gov/STAR/html/daq_l/daq_100.pdf`.

[53] Thorsten Kollegger. *Search for Upsilons in Heavy-Ion Collisions with the STAR Detector*. PhD thesis, Johann-Wolfgang-Goethe Universität Frankfurt am Main, 2005.

[54] W. Busza, R.L. Laffe, J. Sandweiss and F. Wilczek. Review of Speculative 'Disaster Scenarios' at RHIC. *Rev. Mod. Phys.*, 72:1152, 2000.

[55] A. H. Tang. Strangelet search at RHIC. *J. Phys.*, G31:S1187–S1190, 2005, nucl-ex/0412011.

[56] C. Adler et al. Antideuteron and anti-helium-3 production in s(NN)**(1/2) = 130-GeV Au + Au collisions. *Phys. Rev. Lett.*, 87:262301, 2001, nucl-ex/0108022.

[57] A. Braem et al. Identification of High $p_{\perp}$ Particles with the STAR-RICH Detector. *Nucl. Instrum. Meth. A*, 499:720, 2003.

[58] Torbjorn Sjostrand et al. High-energy-physics event generation with PYTHIA 6.1. *Comput. Phys. Commun.*, 135:238–259, 2001, hep-ph/0010017.

[59] P. Jacobs and D. Irmscher. GSTAR: A Geant-based Detector Simulation Chain for STAR. Technical report, STAR, 1996.

[60] R. Brun et al. *GEANT Detector Simulation Software.* CERN, 1987. CERN-DD/EE/84-1.

[61] J. Adams et al. Azimuthal anisotropy and correlations at large transverse momenta in p + p and Au + Au collisions at s(NN)**(1/2) = 200-GeV. *Phys. Rev. Lett.*, 93:252301, 2004, nucl-ex/0407007.

[62] J. Adams et al. Azimuthal anisotropy in Au + Au collisions at s(NN)**(1/2) = 200-GeV. 2004, nucl-ex/0409033.

[63] S. S. Adler et al. Suppressed pi0 production at large transverse momentum in central Au + Au collisions at s(NN)**(1/2) = 200-GeV. *Phys. Rev. Lett.*, 91:072301, 2003, nucl-ex/0304022.

[64] Maya Shimomura. High-p(T) pi0, eta, identified and inclusive charged hadron spectra from PHENIX. 2005, nucl-ex/0510023.

[65] S. S. Adler et al. Centrality dependence of direct photon production in s(NN)**(1/2) = 200-GeV Au + Au collisions. *Phys. Rev. Lett.*, 94:232301, 2005, nucl-ex/0503003.

[66] Andrea Dainese, Constantin Loizides, and Guy Paic. Leading-particle suppression and surface emission in nucleus nucleus collisions. 2005, hep-ph/0511045.

[67] Dan Magestro. Direct observation of dijets in central Au + Au collisions with STAR. 2005, nucl-ex/0510002.

[68] S. Voloshin and Y. Zhang. Flow study in relativistic nuclear collisions by Fourier expansion of Azimuthal particle distributions. *Z. Phys.*, C70:665–672, 1996, hep-ph/9407282.